Ph.D. in Science – curriculum Chemical Science

Tetrapyrrolic Materials for Solar Energy Production

SSD: CHEM-03/A - General and Inorganic Chemistry

Tutor

Prof. Sandra Belviso

Ph.D. Candidate

Giuseppe Larotonda

Co-Tutor

Prof. Stefano Superchi

Ph.D. Program Coordinator

Prof. Patrizia Falabella

XXXVIII CYCLE

Abstract

The increasing global demand for energy, largely satisfied through fossil fuel consumption, represents one of the most critical challenges of the 21st century due to its strong contribution to greenhouse gas emissions and climate change. In this context, the development of sustainable and low-impact energy conversion technologies has become essential. Among renewable energy sources, photovoltaics plays a central role, and particular interest has recently been directed toward organic photovoltaic (OPV) systems due to their potential advantages, including low-cost fabrication, mechanical flexibility, lightweight properties, and suitability for large-area and building-integrated applications.

However, despite significant progress, OPV technologies still suffer from limitations in terms of power conversion efficiency and long-term stability. Therefore, the design and development of novel photoactive materials with improved optoelectronic properties remain a key objective. In this framework, the present PhD work focuses on the synthesis, characterization, and application of tetrapyrrolic macrocycles, specifically thioalkyl-substituted porphyrazines, as promising materials for solar energy conversion.

Tetrapyrroles are particularly appealing as photoactive systems due to their structural similarity to natural light-harvesting molecules such as chlorophyll, as well as their strong absorption in the visible region, high chemical stability, and tunable electronic properties. Among them, porphyrazines have been relatively less explored in comparison to porphyrins and phthalocyanines, despite offering unique opportunities for molecular engineering. Thioalkyl-substituted porphyrazines exhibit distinctive optical and electronic features due to the presence of sulfur atoms, which introduce additional electronic transitions and broaden the absorption spectrum, enabling panchromatic light harvesting across the visible range.

The main objective of this work was the synthesis of novel asymmetrically substituted thioalkyl porphyrazines and their metal complexes, along with the investigation of their structural, spectroscopic, and electrochemical properties, and their implementation in different types of organic photovoltaic devices, including dye-sensitized solar cells (DSSCs) and bulk heterojunction (BHJ) solar cells.

Several synthetic strategies were developed to introduce functional groups at the β-position of the porphyrazine macrocycle. New thiophene-based substituents bearing ester functionalities were successfully introduced through Suzuki–Miyaura and Liebeskind–Srogl cross-coupling reactions. These modifications were designed to promote anchoring to TiO_2 surfaces in DSSCs and to enhance electronic interactions within the macrocycle. However, the inability to efficiently convert ester groups into the corresponding carboxylic acids limited the applicability of these systems as DSSC sensitizers.

In parallel, a series of porphyrazines functionalized with extended aromatic moieties, such as pyrene and helicene units, were synthesized to improve π–π interactions with carbon-based electron acceptors. These systems were investigated for application in BHJ solar cells and in supramolecular nanohybrids with nanocarbon materials. In addition, a novel β-η^1-palladium(II) thioethyl porphyrazine complex was isolated as catalytic intermediate during the Suzuki cross-coupling reactions. This compound represents the first example of a isolable β-ring metalated tetrapyrrole. This organometallic compound was fully characterized by spectroscopic methods and single-crystal X-ray diffraction. Moreover, detailed experimental and computational studies (TDDFT) revealed peculiar electronic features, including charge-transfer transitions involving the metal fragment, suggesting its potential relevance for optoelectronic applications .

The interaction between β-η^1-palladium(II) thioethyl porphyrazine and graphene nanoflakes was also investigated through the preparation of non-covalent nanohybrids. Spectroscopic and microscopy techniques confirmed the formation of these hybrid systems, highlighting changes in optical properties and significant fluorescence quenching. Despite these promising characteristics, preliminary photodetectors based on these materials did not exhibit measurable photocurrent, indicating that further optimization is required.

In the last stage of the thesis work, the first bulk heterojunction solar cells incorporating thioalkyl porphyrazines as donor materials were fabricated and evaluated. Although the achieved power conversion efficiencies were relatively low (up to ~0.1%), these results represent a significant proof of concept, demonstrating, for the first time, the feasibility of employing porphyrazine-based systems in BHJ architectures. Among the investigated compounds, the best performance was obtained with symmetric porphyrazines and helicene-substituted derivatives.

Overall, this work provides new insights into the design, synthesis, and application of porphyrazine-based materials for organic photovoltaics. Although the performance of the fabricated devices is still limited, the results highlight the strong potential of thioalkyl porphyrazines as tunable chromophores for solar energy conversion. Future improvements will require the optimization of molecular structure, device architecture, and processing conditions, as well as the exploration of alternative acceptor materials and hybrid systems.

Abstract in italiano

La crescente domanda energetica globale, ancora in larga misura soddisfatta mediante il ricorso ai combustibili fossili, rappresenta una delle sfide più rilevanti del XXI secolo, alla luce del suo significativo contributo alle emissioni di gas a effetto serra e ai cambiamenti climatici. In questo scenario, lo sviluppo di tecnologie sostenibili e a ridotto impatto ambientale per la ~~conversione~~ produzione di energia assume un ruolo di primaria importanza. Tra le fonti rinnovabili, il fotovoltaico occupa una posizione centrale e, negli ultimi anni, una sempre crescente attenzione è stata rivolta ai sistemi fotovoltaici organici (OPV), in virtù dei loro potenziali vantaggi tra cui la fabbricazione a basso costo, la flessibilità meccanica, la leggerezza e l'idoneità all'impiego in dispositivi di grande area ed integrate negli edifici.

Nonostante i notevoli progressi conseguiti, le tecnologie OPV presentano tuttora limitazioni legate all'efficienza di conversione della potenza e alla stabilità nel lungo periodo. Di conseguenza, la progettazione e lo sviluppo di nuovi materiali fotoattivi rappresentano un obiettivo di fondamentale rilievo. In tale contesto, il presente lavoro di dottorato si concentra sulla sintesi, caratterizzazione e applicazione di macrocicli tetrapirrolici, con particolare riferimento alle porfirazine tioalchil-sostituite, quali materiali promettenti per la conversione dell'energia solare.

I tetrapirroli costituiscono sistemi fotoattivi di particolare interesse, grazie alla loro analogia strutturale con molecole naturali coinvolte nei processi di raccolta della luce, come la clorofilla, nonché all'intenso assorbimento nella regione del visibile, all'elevata stabilità chimica e alla possibilità di modulare finemente le proprietà elettroniche. In questo ambito, le porfirazine risultano ancora relativamente meno studiate rispetto a porfirine e ftalocianine, pur offrendo peculiari opportunità di ingegnerizzazione molecolare. Le porfirazine tioalchil-sostituite presentano caratteristiche ottiche ed elettroniche distintive, riconducibili alla presenza di atomi di zolfo, capaci di introdurre ulteriori transizioni elettroniche e di ampliare lo spettro di assorbimento, generando un sistema pancromatico nell'intervallo del visibile.

L'obiettivo principale del lavoro ha riguardato la sintesi di nuove porfirazine tioalchiliche non-simmetricamente sostituite e dei relativi complessi metallici, unitamente allo studio delle loro proprietà strutturali, spettroscopiche ed elettrochimiche e alla loro integrazione in differenti dispositivi fotovoltaici organici, incluse celle solari sensibilizzate da colorante (DSSCs) e celle solari ad eterogiunzione di bulk (bulk heterojunction, BHJ).

A tal fine, sono state sviluppate diverse strategie sintetiche volte all'introduzione di gruppi funzionali in posizione β del macrociclo porfirazinico. Nuovi sostituenti tiofenici recanti funzionalità esteree sono stati introdotti con successo mediante reazioni di accoppiamento incrociato di Suzuki–Miyaura e Liebeskind–Srogl. Tali modifiche sono state progettate per favorire l'ancoraggio alle superfici di

TiO_2 nelle DSSCs e per intensificare le interazioni elettroniche all'interno del macrociclo. Tuttavia, l'impossibilità di convertire efficacemente i gruppi esterei nei corrispondenti acidi carbossilici ha limitato l'applicabilità di questi sistemi come sensibilizzatori per DSSC.

Parallelamente, è stata sintetizzata una serie di porfirazine funzionalizzate con unità aromatiche estese, quali pirene ed elicene, con l'obiettivo di migliorare le interazioni π–π con accettori elettronici a base carboniosa. Tali sistemi sono stati investigati sia per l'impiego in celle solari BHJ sia per la formazione di nanoibridi supramolecolari con materiali nanocarboniosi. Inoltre, un nuovo complesso di β-η^1-palladio(II) tioetil-porfirazina è stato isolato come intermedio catalitico durante le reazioni di cross-coupling di Suzuki. Questo composto rappresenta il primo esempio di complesso tetrapirrolico metallato in posizione β- sul macrociclo. Questo composto è stato caratterizzato mediante metodi spettroscopici e diffrazione di raggi X su cristallo singolo. Studi sperimentali e computazionali dettagliati (TDDFT) condotti su tale complesso organometallico hanno messo in evidenza peculiari proprietà elettroniche, incluse transizioni a trasferimento di carica che coinvolgono il frammento metallico, suggerendone il suo potenziale interesse per applicazioni optoelettroniche.

A tal fine , è stata approfondita l'interazione tra il complesso β-η^1-palladio(II) e i nanoflakes di grafene attraverso la preparazione di nanoibridi non covalenti. Le analisi spettroscopiche e microscopiche hanno confermato la formazione di tali sistemi ibridi, evidenziando modifiche delle proprietà ottiche e un marcato quenching della fluorescenza. Sebbene tali caratteristiche risultino promettenti, i fotorivelatori preliminari basati su questi materiali non hanno mostrato una fotocorrente misurabile, indicando la necessità di ulteriori ottimizzazioni.

Nell'ultima fase del lavoro di Tesi, sono state fabbricate e valutate le prime celle solari a eterogiunzione di bulk contenenti porfirazine tioalchil-sostituite come materiali donatori. Sebbene le efficienze ottenute siano risultate ancora contenute (fino a circa 0,1%) rispetto a sistemi porfirinici altamente ingegnerizzati, tali risultati costituiscono una significativa prova di concetto, dimostrando per la prima volta la fattibilità dell'impiego di sistemi porfirazinici in architetture BHJ. Tra i composti esaminati, le migliori prestazioni sono state ottenute con porfirazine simmetriche e derivati sostituiti con unità elicene.

Nel complesso, questo lavoro offre nuove prospettive sulla progettazione, sintesi e applicazione di materiali basati su porfirazine per il fotovoltaico organico. Pur a fronte di prestazioni dei dispositivi ancora limitate, i risultati ottenuti evidenziano il notevole potenziale delle porfirazine tioalchil-sostituite come cromofori modulabili per la conversione dell'energia solare. Ulteriori sviluppi richiederanno l'ottimizzazione della struttura molecolare, dell'architettura dei dispositivi e delle condizioni di processamento, nonché l'esplorazione di materiali accettori alternativi e di sistemi ibridi.

Summary

Introduction

Today, energy supply comes from a diverse mix of sources, including oil, coal, natural gas, nuclear power, hydropower, solar, wind, and biofuels. However, this diversified energy mix is a relatively recent development; in the past, only a limited number of energy sources were available.

Until the mid-19th century, traditional biomass was the dominant global energy source, with people relying primarily on solid fuels such as wood, crop residues, and charcoal. The Industrial Revolution marked a major turning point, leading to a dramatic increase in the use of coal. As a result, even in the early 20th century, approximately half of the world's energy supply came from coal, while the other half still derived from biomass.

Throughout the 20th century, the global energy system diversified further. Oil and natural gas were introduced first, followed by hydropower, and, from the 1960s onward, nuclear energy. Only in the 1980s did so-called "modern renewable" energy sources, such as solar and wind, begin to emerge.

A key observation is that global energy transitions have historically been very slow, with significant acceleration occurring only in recent decades (Figure 1). For example, in the United Kingdom, nearly two-thirds of electricity generation came from coal in 1990, whereas today this share has declined to around 1%.

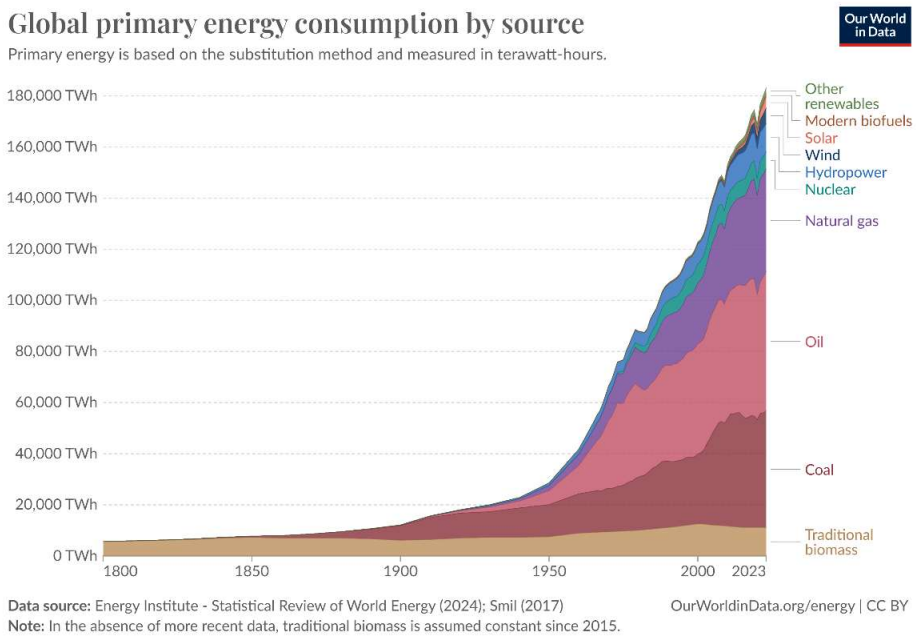

Figure 1 *Global primary energy consumption by source.*[1]

[1] https://ourworldindata.org/global-energy-200-years

The enormous global demand for energy, largely met through fossil fuel production, represents one of the most critical challenges of this century. Energy production accounts for approximately three-quarters of global greenhouse gas emissions, making it the primary driver of climate change.
Moreover, the combustion of fossil fuels and biomass is a major contributor to air pollution, which is one of the leading risk factors for mortality worldwide, particularly in low-income countries.
Additional environmental impacts associated with energy production include land use for oil extraction, as well as the material requirements for renewable energy technologies such as wind turbines and solar panels. These technologies also require significant land areas for installation, further contributing to land use pressures.

Figure 2 *Examples of land consumption: a bucket wheel excavator for coal extraction (upper left), a wind farm (upper right), a solar farm (down).*

It is well established that different energy sources have markedly different impacts on climate change. For this reason, it is essential to promote a transition from high carbon footprint energy sources, such as coal, oil, and natural gas, to low carbon alternatives, including renewable energy and nuclear power.
Among the various renewable energy sources, photovoltaics represents the technology with the greatest potential for improvement. For this reason, it is also the energy production technology that attracts the highest level of scientific interest and research investment worldwide.
Most commercially available photovoltaic panels are currently based on inorganic materials,

primarily silicon (either amorphous or crystalline), which provide good energy conversion efficiency and long-term stability. However, this technology also presents several drawbacks, including high production costs and challenges related to end-of-life disposal. Furthermore, silicon-based panels are rigid, bulky, and non-transparent, which limits their application in architectural contexts.

In recent years, alternative photovoltaic technologies to crystalline silicon have emerged, such as organic photovoltaics (OPV).[2] These systems are based on organic semiconducting materials that enable low-cost fabrication processes (e.g., printing and roll-to-roll techniques) on flexible, lightweight, large-area, transparent, and even colored substrates. The most recent research, focused on the synthesis and development of increasingly efficient and stable materials, demonstrates that OPV is a scientifically mature technology, achieving efficiencies of up to 20% in laboratory conditions and already finding practical applications in building integration, as well as in portable and indoor devices.[3]

Although OPV technologies are not expected to replace silicon-based panels in the short term, their unique features make them a strategic complementary solution for advanced energy design, smart building applications, and the development of hybrid floating photovoltaic (FPV) systems. The integration of OPV into FPV systems may offer several advantages, including reduced load on floating structures, energy harvesting from non-load-bearing and curved surfaces, improved performance under diffuse light conditions, and the possibility of powering sensors and control systems autonomously. Despite these advantages, OPV technology still suffers from limitations related to relatively low power conversion efficiency and poor chemical stability under prolonged illumination and environmental exposure, particularly in large-scale installations.

A key feature of these systems is that the photoactive materials can be finely tuned at the molecular level through chemical synthesis, offering significant room for improvement. Structurally, OPV devices are typically composed of two main components: an electron donor and an electron acceptor. The donor efficiently absorbs solar radiation, while the acceptor facilitates effective electron transfer, enabling photocurrent generation. Possible acceptor materials include single-walled carbon nanotubes (SWNTs), fullerenes, graphene, other polymers, and titanium dioxide (TiO_2), which is commonly used as an acceptor in dye-sensitized solar cells (DSSCs).[4] As for donor materials, some

[2] Organic Photovoltaics: Mechanisms, Materials, and Devices; Sun, S. -S., Sariciftci, N. S., Eds.; Taylor & Francis: Boca Raton, FL, 2005.

[3] Perkhun, P., Khodr, A., Quiroz, Y. A. A., Karahan, A., Alkhatib, H., Bharwal, A. K., Duché, D., Simon, J.-J., Herrero, C. M. R., Watanabe, T., Sekimoto, H., Yoshimoto, N., Margeat, O., Videlot-Ackermann, C., & Ackermann, J. *Energies*, 2026, *19*(7), 1773.

[4] (a) Muchuweni E.; Mombeshora E. T.; Martincigh B. S.; Nyamori V. O. *Front. Chem.,* **2022,** *9*, 733552.
(b) Das S.; Pandey, D.; Thomas, J.; Roy, T.; *Adv. Mater.* **2019**, *31*, 1802722; (c) Bonaccorso, F.; Balis, N.; Stylianakis, M. M.; Savarese, M.; Adamo, C.; Gemmi, M.; Pellegrini, V.; Stratakis, E.; Kymakis, E. *Adv. Funct. Mater.* **2015**, *25*, 3870–3880 (d) Lee, M.; Hwang, E.; Kim, T.; Kwon, T. H.; *Bull. Korean Chem. Soc*., **2024**, *45,* 664–674.

of the most successful systems include polymeric structures or small molecules with extended chromophores, such as tetrapyrroles, which are also found in nature as the "solar antenna" of chlorophyll. These macrocyclic structures, characterized by highly delocalized π-electron systems, exhibit interesting nonlinear optical properties that can be tuned by functionalizing their peripheral structure. Among tetrapyrroles, porphyrazines represent a class of molecules suitable for OPV applications that has been relatively underexplored. These macrocycles consist of tetrapyrrolic units linked by nitrogen bridges. In particular, β-substituted thioalkyl porphyrazines exhibit pronounced nonlinear optical properties, making them particularly attractive for OPV applications.[5,6] The unique properties of thioalkyl porphyrazines are related to the presence of sulfur atoms, which introduce an additional $n_{sulfur} \rightarrow \pi^*$ electronic transition. This results in a broadening of the absorption spectrum in the visible region, overlapping with the maximum of the solar emission spectrum. Consequently, these molecules are capable of covering a large portion of the solar spectrum, representing a significant advantage for OPV applications. If at least one of the beta positions is substituted differently, the porphyrazine becomes asymmetrically substituted. This modification can significantly affect spectroscopic and electrochemical properties of the molecule, as well as its ability to undergo columnar self-aggregation (which is beneficial for charge transport). Furthermore, it can enhance interactions with acceptor materials such as TiO_2 (in DSSCs) or carbon nanostructures in bulk heterojunction (BHJ) organic solar cells.

The aim of this PhD project was therefore the synthesis and investigation of the electronic properties of thioalkyl-porphyrazines with various peripheral substitutions, as well as their metal complexes, and their application in OPV devices. In particular, peripheral functionalization was designed to introduce both polar groups capable of anchoring to TiO_2 and extended aromatic groups to maximize interactions with carbon-based nanostructures. The ultimate goal was the fabrication of OPV cells, both DSSC and BHJ types, and the evaluation of their photovoltaic performance.

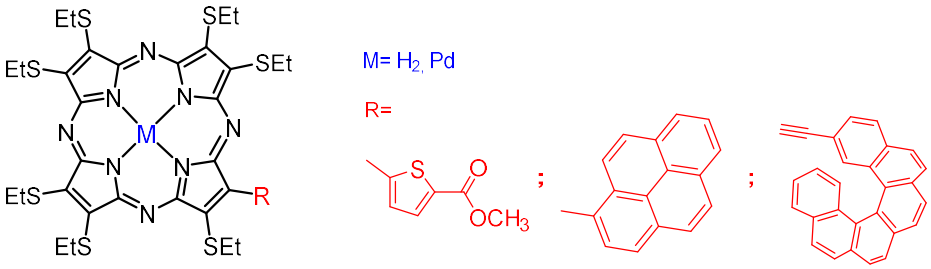

Figure 3 *Structure of thioalkyl-porphyrazine*

[5] Belviso, S.; Capasso, A.; Santoro, E.; Najafi, L.; Lelj, F.; Superchi, S.; Casarini, D.; Villani, C.; Spirito, D.; Bellani, S.; Del Rio-Castillo, A. E.; Bonaccorso, F. *Adv. Funct. Mater*, **2018**, *28,*1705418.

[6] Belviso, S.; Santoro, E.; Penconi, M.; Righetto, S.; Tessore, F.; *J. Phys. Chem. C,* **2019**, *123*, 13074.

Chapter 1

Solar source energy: Organic Photovoltaic

1.1 Historical notes

Among different energy source, the solar is one of the most interesting. The conversion of light into electricity was first discovered in 1839 by Alexandre Edmund Becquerel who noted an increase of the current intensity under illumination during an electrochemical experiment in aqueous solution with a platinum electrode covered with either silver bromide or silver chloride. This discovery was followed by the works of Willoughby Smith in 1873 and William G. Adams in 1876 that described the first reports on Selenium photoconductivity.[1] Then Pochettino in 1906 and Volmer in 1913,[2] observed for the first time photoconductivity in an organic compound: the anthracene, while the first inorganic solar cell was developed in1954 at Bell's Laboratories. This cell was based on silicon and displayed 6% of solar energy conversion efficiency. Another key discovery was achieved in early 60's when it was discovered that many common dyes, such as methylene blue, had semi conducting properties, thus being the firsts materials to exhibit photovoltaic effect. Such effect was also observed in many important biologically active molecules such as carotenes, chlorophylls, and other porphyrins, as well as in the structural related phthalocyanines (Pc).[3,4] In 1986 the first organic solar cell was built by Tang.[5] It was constituted by a glass covered with Indium-Tin Oxide (ITO) on which a thin layer of copper phthalocyanine was deposited by evaporation together with an additional layer of perylene tetracarboxylic acid derivative. Finally, the system was connected to an Ag electrode.

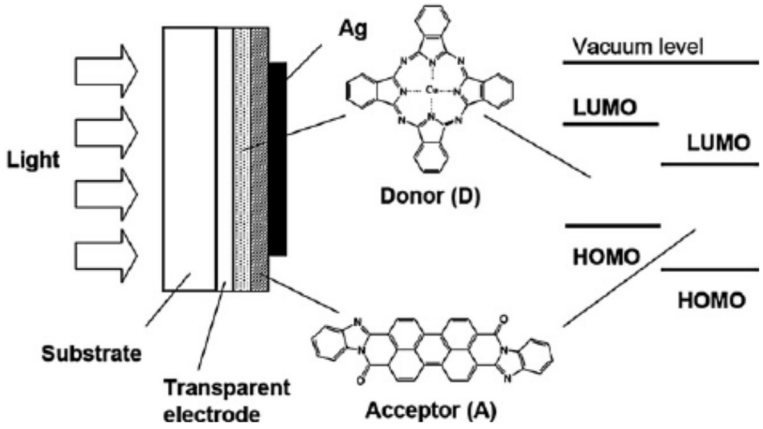

Figure 1.1.1 *First organic solar cell designed by Tang with HOMO-LUMO energy level for the molecules.*

This cell (Figure 1.1.1) was a bilayer cell consisting of a transparent electrode, typically a conducting oxide (like ITO), two organic light-absorbing layers and a second electrode. The bilayer is made by two different organic compounds that have different semiconducting properties. One with an electron-

donor character and the other with electron-acceptor character. The donor (D) exhibits a low ionization potential (and thus a high lying HOMO energy), while the acceptor (A) possesses a high electron affinity (and thus a low lying LUMO energy). Another key discovery happened in early 90s when Heeger *et al.* observed the ultrafast photo-induced electron transfer occurring from a conjugated polymer to C_{60} [6,7] and the consequent enhancement in charge photogeneration yield opened the way to the use of solution processed polymers in OPV (Organic PhotoVoltaic).[8]

One of the limits of the bilayer cells is linked to the short exciton diffusion length that requires a very thin active layer, thus limiting the light absorption. To overcome this limit, in 1992 the Bulk Hetero Junction Cells (BHJ) were developed. This type of cell is made by a continuous interpenetrating network of donor and acceptor materials. This structure provides a large area for excitons dissociation and, thus, reduces the pathway of separated excitons to the corresponding electrode. The development of BHJ was a milestone in OPV because it provided a great improvement of the Power Conversion Efficiency (PCE) of the OPVs. Over the past two decades, BHJ-OPVs have dominated the field of OPVs with extensive material and device engineering, leading the PCE beyond a 19%,[9] a value that is close to the efficiency of silicon based solar cells. This success was mainly due to the development of low bandgap conjugated organic semiconductors with deep HOMO levels enabling higher light harvesting and optimized selective layers for effective charge collection.[10] Since 2010, benzodithiophene based D-A conjugated polymers, including PTB7,[11] PM6,[12] and D18[13] have provided a rapid development in OPVs as donor. With the large improvement of the donor materials, also an improvement for the acceptors was achieved, leading to the development of several types of acceptor materials such as fullerene, non-fullerene, and polymers.[14]

Another milestone in the field was the development of dye-sensitized solar cells (DSSCs), first reported by Michael Grätzel and Brian O'Regan in 1991.[15] These solar cells convert light into electricity through a mechanism analogous to natural photosynthesis, initially achieving an efficiency of about 7%. DSSCs are low-cost photovoltaic devices based on the interaction between a molecular donor (the dye) and a semiconductor acting as an electron acceptor. Since the first DSSC was developed, significant improvements in power conversion efficiency (PCE) have been achieved, reaching a maximum of approximately 13% according to NREL data.[16] This record efficiency was first reported at EPFL in 2014 by Grätzel and co-workers[17] and was further slightly improved by Zhang et al. in 2019.[18]

Despite the progress achieved and the development of various types of organic solar cells, their efficiency and stability remain lower than those of silicon-based devices. This represents a major limitation for OPV technologies. In response, the scientific community has focused on the development of a new generation of solar cells with higher power conversion efficiencies (PCEs)

than bulk heterojunction (BHJ) and dye-sensitized solar cells (DSSCs). This new class of devices is based on organometal halide perovskite crystals as the active material, which have rapidly emerged as highly promising photovoltaic materials due to their exceptional optoelectronic properties.[19] In general, organo-metal halide perovskites crystals can be described by the chemical formula ABX_3 where A is an organic cation such as methylammonium (MA); B is a metal cation such as lead (Pb) and X is a halogen atom disposed in the lattice as described in

Figure 1.1.2.

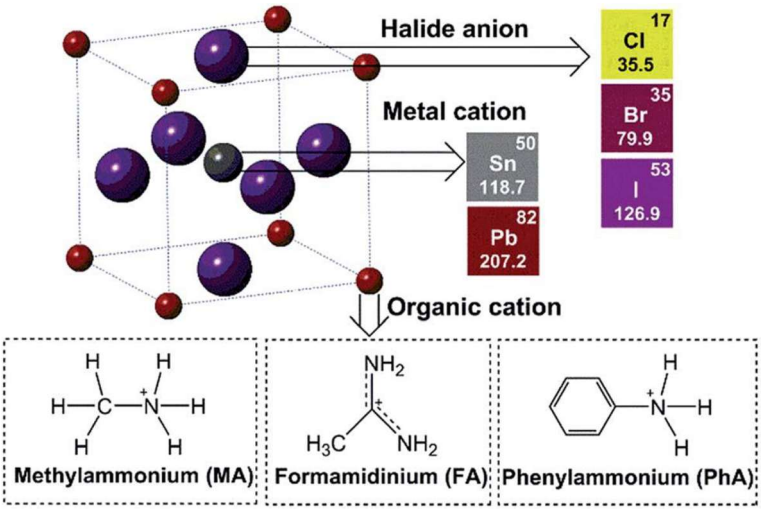

Figure 1.1.2 *Schematic crystal structure of organo-metal halide perovskite.*

The first perovskite solar cell (PSC) reported in 2009 by Miyasaka *et al.* [20] displayed a 3.8% PCE, but only five years later, in early 2016, a 22.1% PCE was reported [21] by researchers from KRICT and UNIST representing the largest increase in PCE. Nowadays the power conversion efficiency of these cells is around the 27%.[22] The main features of organo-metal halide perovskite are the long-range ambipolar charge transport,[23] high dielectric constant,[24] low exciton binding energy,[25] intrinsic ferroelectric polarization[26] and spin-dependent response.[27]

Despite their high power conversion efficiencies, perovskite solar cells still suffer from significant stability issues. One of the main challenges arises from the presence of organic components, which are often water-soluble and therefore require effective encapsulation. Moreover, these organic materials are prone to degradation when exposed to humidity and elevated temperatures. As a result, the large-scale commercialization of PSCs has progressed more slowly than initially expected. Another critical issue is related to the most commonly used metal cation, lead, which is toxic to human health and harmful to the environment, thereby limiting the widespread applicability of this technology.

At the same time, research on silicon-based solar cells continues to advance. Ongoing developments have led to more cost-effective fabrication processes, reinforcing silicon-based technologies as the most commercially attractive option in photovoltaics. However, silicon is not the only high-performance technology: the highest efficiencies ever achieved for solar cells have been obtained with multijunction devices. These cells consist of multiple p–n junctions stacked on top of each other, with progressively decreasing bandgaps from top to bottom, and typically employ III–V semiconductor alloys in combination with silicon as active materials. Multijunction solar cells have reached a record power conversion efficiency of approximately 47%.[28] Another promising research direction is represented by perovskite–silicon tandem solar cells, in which a PCS is stacked onto a silicon-based device. These tandem architectures have achieved power conversion efficiencies of around 34%.[29]

In

Figure 1.1.3 the evolution of power conversion efficiency through the years since 1976 till March 2026 reported by National Renewable Energy Laboratory (now National Laboratory of the Rockies) sponsored by the U.S. Department of Energy is showed.[16]

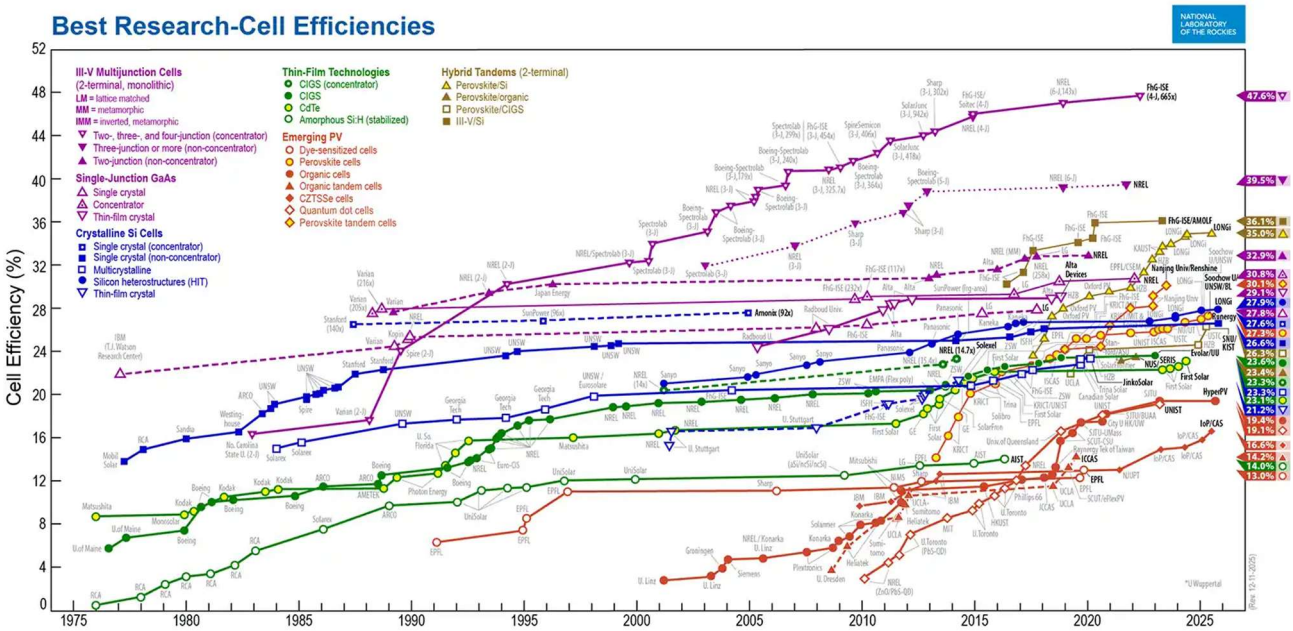

Figure 1.1.3 *Best research cell efficiencies divided by type.*

1.2 The photovoltaic process

Solar cell is a device capable of turning light energy into electricity and its working is mainly based on two processes: the light absorption and the electric current generation. To develop this processes a solar cell is made of two or more materials assembled in a precise way to maximize the efficiency. For every solar cell, from the simplest to the most complicated, the basic and essential constituents are:

- A semiconductor material with a proper *band gap* that ensure the light absorption in the visible region of the light spectrum.
- A pair of electrodes, one of which transparent, where to carry the generated charge.

Looking at the classic inorganic solar cell, it is based on p-n junction formed by two different doped semiconductors. One of *p-type* that works also as hole transporting material and is positively charged and the other of *n-type* that works as electron transport material and is negatively charged.

When the two semiconductors are joined together in a device named *diode* at the junction some holes from the p-type migrate into the n-type where they combine with electrons. *Vice versa* some electrons from the n-type migrate into the p-type semiconductor where they rearrange with holes. This zone near the junction where the charge carriers rearrange generating a charge-less zone is named *depletion region* and leads to a built-in potential and to an electric field that is confined near the junction as shown in Figure 1.2.1.[30]

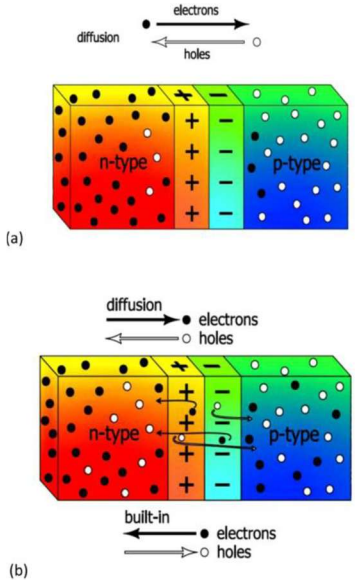

Figure 1.2.1 *schematic representation of (a) diffusion establishing a "built-in" electric field and (b) the motion of mobile electrons and holes due to diffusion and the electric field (formation of depletion region).*

When the diode is irradiated by light, the materials absorb only the photons that have equal or greater energy than its band-gap. The absorption promotes the excitation of electrons from the valence band to the conducting band and consequently the formation of holes in the valence band. Normally when this happen, the relaxation of electrons is fast but in the diode the presence of the built-in electric field at the junction separates the hole-electron couples that generate current while the depletion region prevents the recombination and keep the separation.

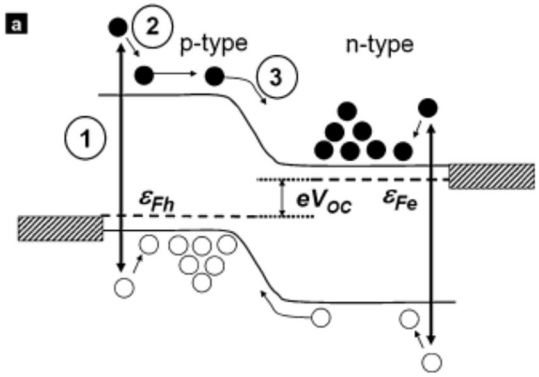

Figure 1.2.2 *Energy levels in an inorganic p-n junction under illumination. ε_{Fe} and ε_{Fh} denote the quasi-Fermi levels in the n-type and p-type semiconductors. The difference between the quasi-Fermi level energies determines the maximum open-circuit voltage (VOC) under illumination.*

Following the scheme in Figure 1.2.2, when light hits the diode the absorption of photons with an average photon energy greater than the band-gap occurs. After this, in both side of the junction in the n-type and p-type semiconductors, the thermalization of the holes and electrons near the top of valence and conduction bands happen, respectively (step 2). At this point, the *minority carriers* (electrons in the p-type semiconductor and holes in n-type semiconductor) diffuse to the junction where they are swept away and accumulate on the other side of the junction where they become majority carriers (step 3). At this point, if the device is connected to an external electric circuit, the electrons will move in the conduction band of the n-type material towards the cathode while the holes will migrate in the p-type material towards the anode. In this way an electric current will flow in the circuit. Such device represents a solar cell in short-circuit conditions.

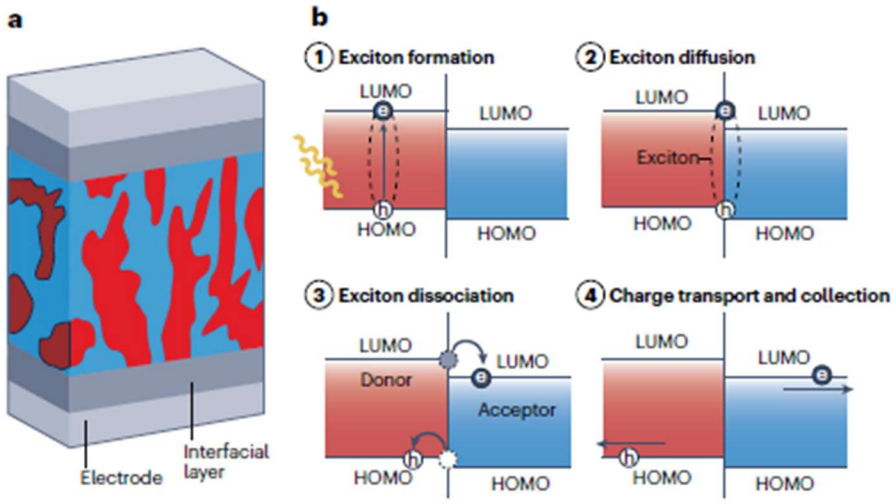

Figure 1.2.3 *(a) Schematic representation of BHJ cell. (b) Energy level diagram and working scheme of BHJ cell under illumination.*

The operational principles in OPV differ significantly from the traditional crystalline silicon based photovoltaics. Following the scheme in Figure 1.2.3[31] the absorption of photons with average photon energy greater than the optical band-gap and the subsequent thermalization, generates the excitons (step 1). The excitons so generated diffuse through the donor material to the heterojunction (step 2) where the excitons dissociate and transfer an electron into the acceptor material (step 3) while the holes remain in the donor material. At this point, the charges are transported and collected at the electrodes (step 4) and, if the device is connected to an external circuit, the current will flow through it. The maximum open circuit voltage (V_{OC}) is determined by the difference between the donor Ionization Potential and acceptor Electron Affinity.

The process of light conversion in electricity in an organic solar cell can be schematically described in three key points:

- Absorption of a photon that led to the formation of an excited state with the creation of the exciton (a bounded electron-hole pair).
- Exciton diffusion to a region where exciton dissociation occurs (in other words the charge separation).
- Charge transport within the organic semiconductor to the respective electrodes.

The critical step in all the process is the charge separation by exciton dissociation, and to achieve a good charge separation, an electrical field is needed. In an OPV cell this electrical field is provided by the asymmetrical *ionization energy/workfunction* of the electrodes. This asymmetry is the reason why electron flow is more favoured from the low workfunction electrode, that is the cathode, to the high workfunction electrode, that is the anode, this is a phenomenon referred as rectification.

1.3 Photovoltaic device features

To evaluate the performances of photovoltaic devices the following parameters are generally considered:[32,33,34]

- Short-circuit current (I_{SC}) or most of the times the short-circuit current density (J_{SC}), that is the current that flows through the cell when the voltage across is zero. Depends on overall the photovoltaic process, like the absorption, the exciton diffusion and dissociation, the charge transport and collection process. In an ideal situation, the short-circuit current and the light generated current are identical. Therefore, the short-circuit current is the largest current which may be drawn from the solar cell.
- Open-circuit voltage (V_{OC}) is the maximum voltage across the cell when no current is flowing through it. In the inorganic device depend by the Fermi level of the p-n junction while in the OPV depends on the gap between the HOMO of donor and the LUMO of the acceptor.
- Fill Factor (FF) is defined as the ratio between the maximum power delivered to an external circuit and the potential power defined as the product between the V_{OC} and the I_{SC}. It indicates how easy is to carry out the charges from the cell.

$$FF = \frac{P_{MAX}}{V_{OC} I_{SC}}$$

- Power Conversion Efficiency (PCE, η_e) is defined as the ratio between the maximum electrical power generated and the incidental optical power (the incoming solar power). To evaluate this parameter is possible to use the ones described above:

$$PCE = \frac{P_{MAX}}{P_{IN}} = \frac{V_{OC} I_{SC} FF}{P_{IN}}$$

The spectral response is another important parameter to evaluate solar cells. To do this, the device is illuminated by a monochromatic light source, generally consisting of a broadband illuminator dispersed by a monochromator. The photocurrent is measured as the function of wavelength and compared to the light intensity of the photon flux. In this way it is possible to measure the external quantum efficiency (EQE), also known as the incident photon conversion efficiency. It is a measure of how much current is generated under illumination by a specific light wavelength or in other words, represents the probability of the electron-current generation by a photon absorption capable to pass through an external circuit.[35] It is given by the number of electrons generated per incident photon:[32]

$$EQE = \frac{n_e}{n_{ph}} = \frac{I_{SC} hc}{P_0 \lambda e}$$

Where P_0 is the incident optical power, h is the Plank's constant, c is the light speed, λ is the incident light wavelength and e is the electron electrical charge.

To evaluate all these parameters in laboratory it is common to measure the current/voltage curve (I/V curve) in different operative conditions.

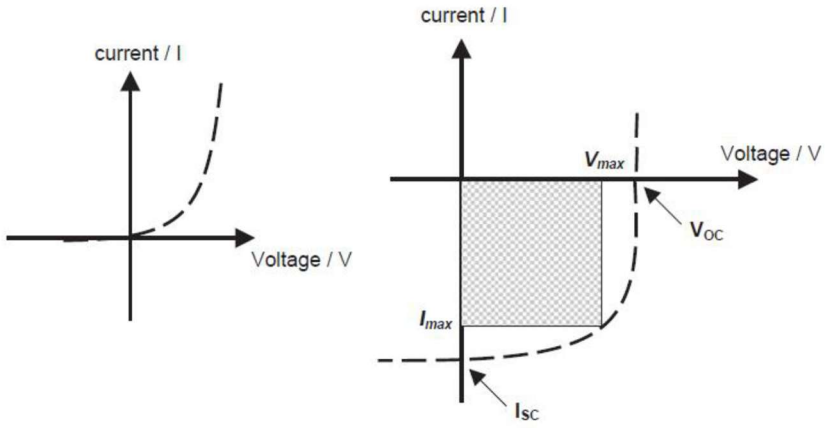

Figure 1.3.1 *(a) I/V curve in dark condition (b) I/V curve measured under illumination.*

In Figure 1.3.1 two I/V curve are shown. In the second one, it is immediately visible that the point where the curve intersects the X and Y axis are respectively the V_{OC} and the I_{SC} while the "squareness" of the curve represents the Fill Factor.

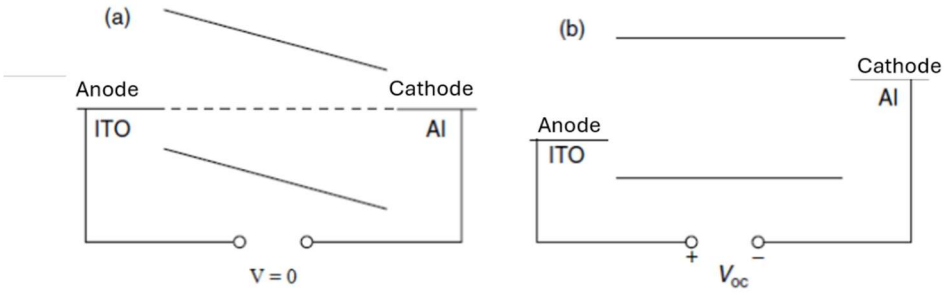

Figure 1.3.2 *(a) short-circuit condition and (b) open-circuit condition.*

When the device is in short-circuit condition (Figure 1.3.2), some electrons migrate from the higher Fermi level electrode (the cathode) to the lowest Fermi level electrode (the anode). This migration modifies the workfunction of the two electrodes rising the one of the anode and lowering the one of the cathode until reaching the equilibrium between the two Fermi level and the electric field. Because of this, also a variation in HOMO and LUMO energy levels is observed. The one closer to the cathode, positively charged, lowers while the one closer to the anode, negatively charged, rises. When the equilibrium is reached, current and potential are both zero. Under irradiation, the excited electrons will move towards the cathode and the holes towards the anode, generating the short-circuit current.

When the device is irradiated in open-circuit condition, an external potential is applied to counterbalance the migration from cathode to anode. In this condition the current flow is zero while the V_{OC} is the difference between the two electrode workfunction. There is no built-in electric field.

1.4 Organic solar cells

As described in Paragraph **1.1**, after the first bilayer, two different type of solar cells were developed to improve the efficiency of organic solar cells: the Bulk HeteroJunction (BHJ) solar cell and Dye Sensitized Solar Cell (DSSC) or Grätzel cell.

Another possible classification according to the nature of the active layer is made. There are three cell types:

- *Molecular devices,* where the active layer is made by small molecules.
- *Polymeric devices,* where the active layer is made by polymers.
- *Hybrid and quantum dots devices*, where the donor material is made by organic or metal-organic compound and the acceptor is inorganic.

1.4.1 Organic heterojunction solar cells

The organic heterojunction is the key to the photovoltaic process and properties of organic solar cells. As described before, the critical step in photovoltaic process is the exciton dissociation speed and to have an increase of the speed, it is common to maximize the difference between the ionization potential and electron affinity of the two materials involved in the device. One is the donor (D), that is the light absorbing and hole transporting material, the other one is the acceptor (A) that works as electron transfer unit. To build an efficient device, the donor must have lower ionization potential than the acceptor that has higher electron affinity. This means that donor has higher HOMO energy and the acceptor has lower LUMO energy.

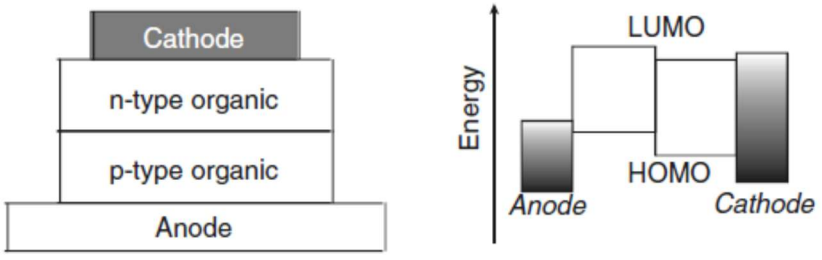

Figure 1.4.1 *Scheme of generic organic bilayer heterojunction cell (left) and scheme of energy levels in generic organic heterojunction cell (right).*

As shown in Figure 1.4.1, donor material acts as the p-type semiconductor while the acceptor acts as n-type semiconductor in p-n junction. These two materials are inserted between a semi-transparent

anode, that permit the light passing through and hit the donor material, while the cathode can be metallic. The electrodes are chosen with a proper workfunction to maximize the efficiency, avoiding the side effects of the excitation process, such as hole-electron recombination, relaxation process etc. Usually, the electrode used are the semi-transparent Indium Tin Oxide (ITO) or the Fluorine doped Tin Oxide (FTO) while the other electrodes can be metallic made of silver, gold etc.
If the donor and the acceptor materials are disposed like in Figure 1.4.1, a bilayer organic photovoltaic cell is obtained. In this type of cell, the exciton separation is better than the single layer cell but there is a limit linked to the diffusion of the exciton. In fact, the exciton diffusion length is about 10 nm, while the thickness of the layer is about 100 nm. This led to waste a lot of excitons that will never reach the interface. To avoid this problem the *Bulk Heterojunction*, where the donor and the acceptor materials are mixed and placed between the electrodes, was developed (Figure 1.4.2).

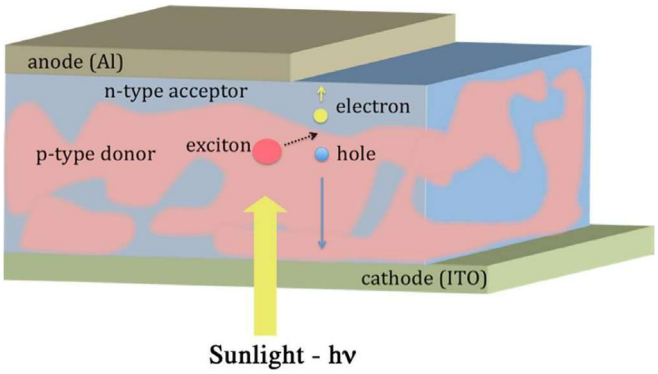

Figure 1.4.2 *Schematic representation of generic Bulk Heterojunction solar cell. The exciton separation and charge separation is also shown.*

In this type of cell, the heterojunction is spread in the bulk of the film and this lowers the distance between the exciton formation site and the junction, making it in the order of exciton diffusion length, eventually enhancing the performance of the cell. The production of the charges in any places of the bulk, increases the importance to have electrodes with the right *workfunction,* capable of collecting them. There are two possible ways to stack a BHJ solar cell, the conventional one and the inverted one. In both structures,[36] shown in Figure 1.4.3, the active layer is placed between the two electrodes. For the conventional one, the holes are transported to the anode and the electrons to the cathode. The anode is typically made by a substrate (usually glass or transparent polymer) coated with a high workfunction transparent semiconductor usually made of ITO. On the top of the electrode a layer of hole selecting/electron blocking material is deposited to help the holes transport. Usually, in the conventional structure, this is a matrix of poly (3,4-ethylenedioxythiophene (PEDOT) and

poly(styrenesulfonate) (PSS). These materials display high optical transparency and good charge mobility properties.

The cathode is made by a low workfunction electrode usually made by Al, chosen also for its high reflectivity. To help the electron transport a layer of electron selecting/hole blocking material is deposited between the active layer and the electrode. Usually in the conventional structure this layer is made by LiF or Ca. This structure is also affected by some problems due to the acidity of the PEDOT: PSS, that can be destructive towards the active layer, or to the reactivity of the aluminium electrode with oxygen and humidity.

To overcome these problems, the inverted design was developed; it consists in an inversion of the electrode functions using a high workfunction metal as reflective electrode. This inversion changes all the working principle of the solar cell. In fact, the ITO now works as cathode and it is coated with an electron transport material such as ZnO or a transition metal oxide. The counter electrode in this structure, can be made by a stable metal like Ag or Au coated with a hole transporter material such as MoO_3 or a high workfunction oxide.

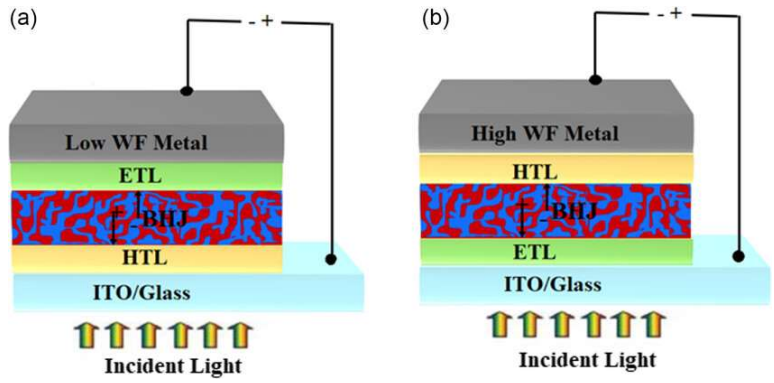

Figure 1.4.3 *(a) Scheme of conventional BHJ solar cell; (b) scheme of inverted BHJ solar cell.*

As described before in this chapter, the active layer is made by two organic compounds: the donor material and the acceptor material. Aromatic or hetero-aromatic molecules are widely used as donor material. These can be aryl or hetero-aryl polymers,[11–13] or small molecules such as tetrapyrroles (mostly porphyrins and phthalocyanines) derivatives.[37] As acceptor materials fullerene derivatives are the most used, especially the phenyl-C61-butyric acid methyl ester ($PC_{61}BM$) or his C71 version. The problem with PCBM is that the absorption spectrum is limited in the visible region and has a relatively deep LUMO, which limits its contribution to J_{SC} of the device and constrains the energy level requirement for donor materials in order to obtain high V_{OC}.[35] To try to overcome these issues, in the last 10 years, different types of acceptors were developed. The first competitors were nanocarbon structures such as carbon nanotubes[38] or graphene[39]. In recent years, another type of acceptor is rising: the *non-fullerene acceptor*. This class of compounds consists of small molecules

or polymers[40] and can be classified in three groups: NFAs (Non-Fullerene Acceptors) with fused-ring core that include molecules with a central core of fused aromatic rings with a side chain attached to one of the carbon atoms in the core and two compact, strong electron-withdrawing end groups; a prominent example of such structure is ITIC in Figure 1.4.4.

NFAs with non-fused ring core, are similar in structure with the fused ring core NFAs, but display a simpler structure that means less synthetic complexity and lower production costs. Because of the lower conjugation, due to the single bonds C-C in the backbone, non-fused ring core NFAs result less effective than fused ring core ones. For this reason, π-bridges between end groups and central core are inserted in the structure.

The third group of NFAs are the polymeric NFAs. They show high thermal and mechanical stability, intrinsic ductility and ensure effective entanglement with other polymer chains. This class are typically designed with a D-A configurations to achieve efficient push-pull electronic structures. The first one introduced is a perylene diimide (PDI) based polymer acceptor, composed of alternating PDI and dithienothiophen units (P1), as shown in Figure 1.4.4.

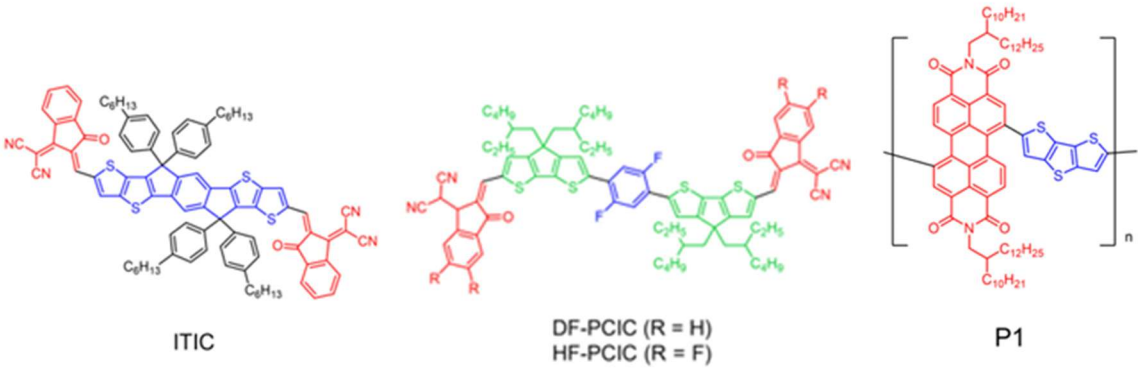

Figure 1.4.4 *Representative chemical structure of three different classes of NFAs.*

1.4.2 Dye sensitized solar cells

Dye-sensitized solar cells (DSSCs) belong to the class of hybrid solar cells, as their active layer consists of an organic molecule, known as the light-harvesting dye sensitizer (antenna), anchored to an inorganic anode, typically made of titanium dioxide (TiO_2). Prior to the work of Grätzel and O'Regan[15], this type of solar cell was based on flat electrodes, which significantly limited efficiency, since only the first monolayer of dye could effectively inject electrons into the semiconductor. In the Grätzel cell, nanostructured TiO_2 is instead employed as the anode, allowing for a much larger active surface area for dye adsorption and, consequently, enhanced electron injection.

The essential parts of DSSC solar cells are:

- A photoanode made of nanocrystalline oxide layer such as TiO_2 deposited on a transparent glass functionalized with ITO or FTO.

- A monolayer of dye sensitizer anchored to the oxide used for light harvesting and exciton formation.
- An electrolyte containing a redox couple that collects electrons at the counter electrode and regenerate the dye, usually the couple is I^-/I_3^-.
- A counter electrode made of platinum coated conductive glass substrate.

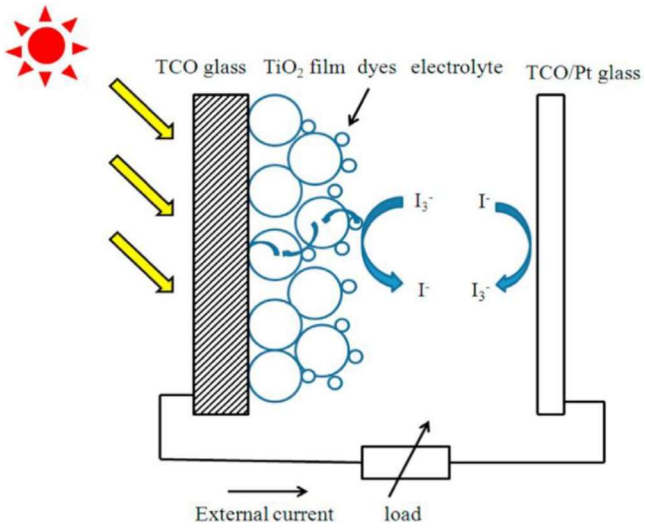

Figure 1.4.5 *Schematic diagram of DSSC solar cell.*

As shown in Figure 1.4.5, when the light is absorbed by the dye, an electron is excited from the HOMO to the LUMO of the dye and injected into the conduction band of the oxide at the photoanode spreading through it. Here an external circuit sends the electron to the counter electrode generating current. To avoid shut down of this current flow, the oxidized dye is regenerated by the redox couple into the electrolyte solution.

DSSCs are well known as a cost-effective photovoltaic technology due to their use of inexpensive materials and simple fabrication processes. Moreover, they are relatively insensitive to environmental contaminants, allowing processing under ambient conditions. Another advantage of DSSCs is that their unique features are well suited to roll-to-roll fabrication, a continuous and low-cost manufacturing method that enables printing on flexible substrates. In addition, DSSCs perform better under low-light or diffuse illumination conditions than conventional solar cells, making them particularly suitable for indoor applications such as windows and sunroofs.[41]

As described in Paragraph 1.1 the efforts in DSSC solar cells, brought the efficiency to a maximum value of 14% in 2019[18]. However, the research is still going on to improve the components of this solar cell type as highlighted below.

The photoanode

The photoanode was the first component that enabled the development of DSSCs. Titanium dioxide (TiO_2) was the first material employed, owing to its stability, non-toxicity, and high refractive index (n = 2.4–2.5). It is widely used as a white pigment in paints, toothpaste, sunscreens, self-cleaning materials, and even in food (under the designation E171). TiO_2 exists in several crystalline forms; however, only one—anatase—is sufficiently efficient as a photoanode. This is due to its wider band gap and higher conduction band edge, which result in a higher Fermi level and open-circuit voltage (V_{OC}) for a given electron concentration in the conduction band.[42] This layer of TiO_2 is coated, for example, on conductive glass substrate (glass-ITO or FTO substrate).

Dye

The photosensitizer or dye, is the heart of the DSSC, it must fulfil some important features:

- The absorption spectrum should cover the visible region or even better the NIR.
- It needs specific anchoring polar groups to link the oxide such as -COOH; SO_3H, *etc.*
- Its LUMO should be higher in energy than the conduction band of the semiconductor oxide to ensure a good electron injection.
- Is important to avoid the dye aggregation because could affect the efficiency of the solar cell.
- The dye must be photostable, electrochemically stable and thermally stable to extend the cell's life.

Many classes of both metal complexes and organic compounds fit this description, therefore, different compounds were employed in DSSC.[41]

Metal complexes have been widely employed due to their broad absorption spectra and favorable photovoltaic properties. Among them, ruthenium complexes have demonstrated the best performance, owing to their wide absorption range, suitable ground- and excited-state energy levels, relatively long excited-state lifetimes, and good stability. [42] However, one limitation of ruthenium complexes is their relatively weak absorption in the near-infrared region of the solar spectrum, which reduces the number of generated excitons. An example of these compounds is shown in Figure 1.4.6.

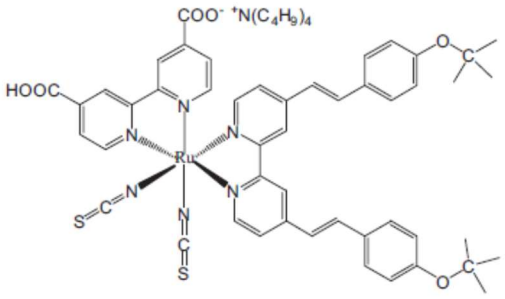

Figure 1.4.6 *Example of Ruthenium complex.*

As an alternative to metal complexes, organic dyes were developed. The possibility of easily design and synthetize the molecular structure of organic dyes is one of the major advantages. They are also cheaper and less toxic for the environment then Ru. Exhibiting higher molar extinction coefficients usually lead to higher efficiency. Among them, tetrapyrroles such as porphyrins[43] and phthalocyanines[44] are widely used because they exhibit intense spectral response bands in the near-IR region and possess good stability making them good candidates for photovoltaic applications. All the dyes to be used in DSSC needs an anchoring group to allow the interaction with the TiO_2 or the other semiconductor oxide. The most used anchoring group is the carboxylate that can interact with the TiO_2 either by covalent bond, electrostatic interaction, and H-bond as shown in Figure 1.4.7.

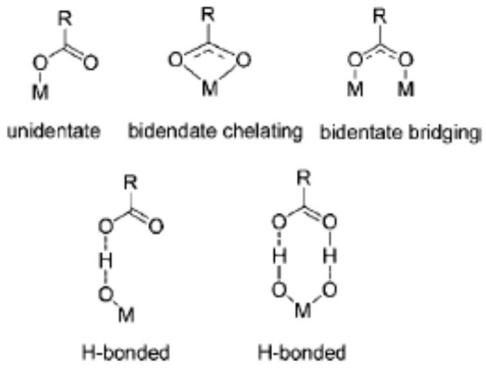

Figure 1.4.7 *Different type of anchoring between TiO_2 (M) and carboxylate group.*

Electrolyte

The electrolyte in a DSSC must exhibit chemical stability, low viscosity to minimize mass transport limitations, and good solubility for the redox couple. It should also be compatible with the sealing material to prevent leakage and evaporation. To address these issues, some solid-state redox couples have been investigated; however, they often cannot completely fill the voids at the semiconductor/dye interface, which can reduce device efficiency. Among the various redox systems, the iodide/triiodide (I^-/I_3^-) couple in liquid form remains the most widely used.

Counter electrode

For DSSCs using the I^-/I_3^- redox couple, the counter electrode is typically prepared by depositing a thin platinum film on a transparent conductive glass substrate or by employing nanoscale platinum clusters. Only a small amount of platinum is required, which preserves the transparency of the glass and allows back illumination of the active layer. This property is particularly important for applications such as windows, rooftops, or decorative installations. Alternative counter electrodes, including platinum-coated nanotubes and graphene-based electrodes, have also been explored to reduce costs while maintaining high catalytic activity.[41,42]

1.5 Organic and inorganic semiconductors: differences and applications

The key difference between organic and inorganic semiconductors lies in the nature of their excited states. Inorganic semiconductors used in photovoltaics are typically crystalline or semi-crystalline solids, in which electronic states form a band structure. In contrast, organic molecules possess localized orbitals and generally form amorphous structures. Consequently, in inorganic semiconductors, electrons excited into the conduction band are readily separated from the holes generated in the valence band, enabling direct charge transport. In organic semiconductors, however, the larger HOMO–LUMO gap leads to the formation of excitons (electron–hole pairs) upon light absorption, which must be dissociated to produce current. Charge transport in organic materials occurs via hopping between molecules, which significantly limits the efficiency of organic solar cells.
The other major difference between the organic and inorganic solar cells is related to the physical properties of the active material. In fact, the inorganic active layer is crystalline, this means that material is rigid and cannot be deformed. Instead, the organic material can be solved for deposition and this led to the possibility of treat the active layer like ink, reducing the production costs.
Furthermore, the active layer in organic photovoltaics is thinner than in inorganic devices. This, combined with solution processing, allows the fabrication of flexible solar cells on polymeric substrates such as PET.
Organic solar cells also exhibit advantages under non-ideal lighting conditions. Silicon solar panels achieve maximum power conversion only when light strikes at specific angles, whereas organic solar cells maintain relatively high efficiency under diffuse or angled illumination, making them suitable for a wider range of environments. These and other advantages and limitations are summarized in Table 1.5.1.

Figure 1.5.1 *Two application of OPV on large scale during the EXPO 2015 in Milan.*

Table 1.5.1 *Main features of most used inorganic and organic cells*

Monocrystalline Si Solar panel	**Thin film solar panel**
Pros: - Longevity. - Efficiency is high in the rang 15-24%. - Lower installation costs. - Space-efficient Cons: - High initial cost (purity of Si must be 99.999%). - High fragility	Pros: - Low manufacturing costs. - Versatile. - Can be printed at industrial scale, making them cheaper than crystalline solar cells. - Have uniform appearance. - Can be made flexible. - Shading and high temperatures do not have any major effect on performance. - Can be used in situation were the space is not a constraint Cons: - Lower efficiency respect the Si solar panels. - Faster degradation compared to the Si solar panels
Polycrystalline Si Solar panel	**Dye Sensitized Solar panels**
Pros: - Simpler production process, cost effective, and less silicon waste. Cons: - Lower conversion efficiency compared to the monocrystalline - Lower space-efficiency. - Less aesthetically pleasing compared to the monocrystalline and thinfilms panels.	Pros: - Low cost. - Good price/performance ratio. - Operate in low light condition and at wider angles. - Operate at lower internal temperatures. - Long life. - Mechanical robustness. Cons: - Less effectiveness in large scale, where higher cost and higher efficiency cells are more practical. - Liquid electrolyte can be a problem because can contain volatile organic solvents. - Liquid electrolyte is not stable in a big range of temperatures, cutting power generation and potential causing physical damage due to freezing.

1.6 Tetrapyrroles as active layer for OPV

The conjugated organic systems are the most suitable for OPV applications. In fact, they are the main alternative to the silicon electronic devices. This applicability is due to their main characteristics such as the high charge mobility, efficient luminescence, high thermal stability and the capability to make thin films. Among all the suitable small organic molecules, tetrapyrroles such as porphyrins, phthalocyanines and porphyrazines, emerged as extremely attractive structures, mainly because of their similarity with natural photoactive molecules like chlorophyll.[45] In Figure 1.6.1 are depicted the structure of the tetrapyrroles.

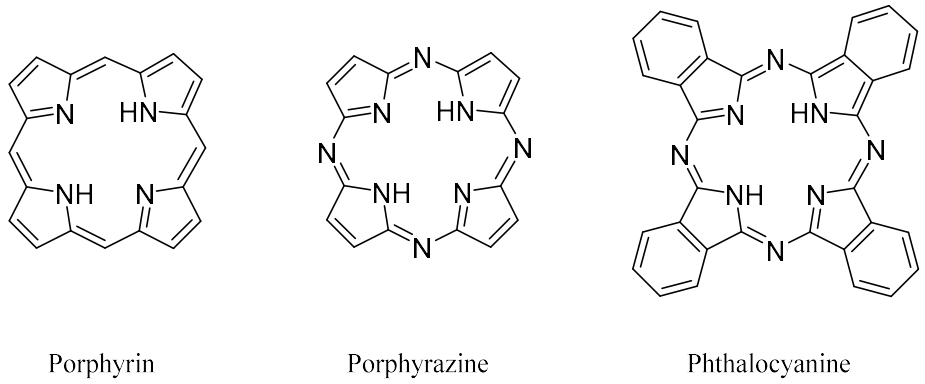

Figure 1.6.1 *Structure of tetrapyrroles.*

These molecules represent highly promising chromophores for artificial photoactive systems due to their strong optical absorption and favorable redox properties. Their remarkable electrochemical and photophysical behavior arises from extended π-conjugation, they also display good chemical and thermal stability, diverse coordination chemistry, and high synthetic versatility.

For efficient light conversion, a molecule must absorb in the visible region of the solar spectrum, and tetrapyrroles exhibit high molar extinction coefficients in the 350–750 nm range. Moreover, their absorption properties can be finely tuned through chemical modification, thereby enhancing device performance. The properties of the macrocycle can be further adjusted by functionalization at the *meso*-positions, β-positions, or within the inner cavity. By selecting appropriate substituents, these systems can be engineered to interact with a wide range of electron acceptors, from oxide semiconductors (such as TiO_2) to nanocarbon materials (e.g., graphene nanosheets or carbon nanotubes).[38,39]

Tetrapyrroles are widely employed in organic photovoltaics, primarily as donor materials,[46] but they have also been investigated as acceptors.[37, 47] In addition, they can play multiple roles in perovskite solar cells, for example as hole-transporting materials[48] or interfacial layers.[49] In contrast to related macrocycles such as porphyrins and phthalocyanines, porphyrazines have been comparatively less explored in photovoltaic applications.

One particularly attractive feature of tetrapyrroles—gaining increasing attention in bulk heterojunction (BHJ) solar cells—is their ability to form liquid-crystalline mesophases. The partial structural order in these phases reduces exciton trapping and promotes efficient charge separation.[50] Consequently, the charge carrier mobility in liquid-crystalline systems is intermediate between that of amorphous solids and single crystals, as illustrated in Figure 1.6.2.

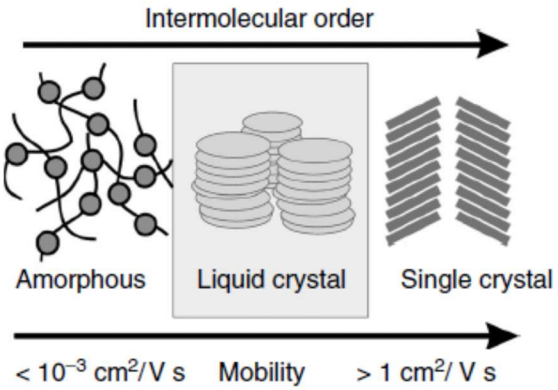

Figure 1.6.2 *Scheme of correlation between intermolecular order and charge carrier mobility.*

Tetrapyrrolic macrocycles can form liquid-crystalline mesophases with a discotic columnar arrangement (as shown in Figure 1.6.3), which promotes charge carrier mobility along the *z*-axis. This behavior arises from strong π–π interactions between the macrocyclic cores, leading to efficient stacking within the columns. In this arrangement, intracolumnar interactions are significantly stronger than intercolumnar ones. As a result, the columns can be regarded as molecular wires, where the conductive π-stacked cores are surrounded by peripheral alkyl chains that act as insulating barriers.

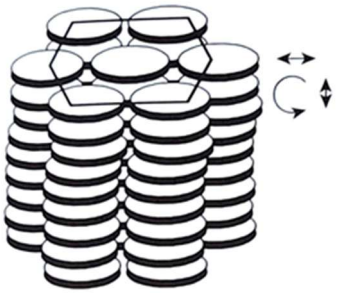

Figure 1.6.3 *Scheme of columnar discotic mesophase.*

Additional features that make tetrapyrroles suitable for BHJ solar cells include their high solubility in common organic solvents and strong absorption in the visible region of the solar spectrum. Tetrapyrroles also possess the appropriate characteristics to act as sensitizers in DSSCs. Indeed, their extended π-conjugation and structural tunability allow optimization of key processes such as light harvesting, charge recombination suppression, and electron injection into the semiconductor, while also minimizing aggregation phenomena.[51]

The focus of this thesis is on porphyrazines, a class of tetrapyrroles that has been only marginally explored in organic photovoltaics. These macrocycles can be considered structural hybrids between porphyrins and phthalocyanines (Figure 1.6.1). Compared to porphyrins, the methine bridges are replaced by nitrogen bridges, as in phthalocyanines, but without the presence of benzo-fused rings. As a result, porphyrazines exhibit an intermediate cavity size between porphyrins and phthalocyanines, as well as comparable molecular rigidity.

Porphyrazine complexes display a wide range of coordination chemistry, excellent photostability, good solubility in common organic solvents, and distinctive spectroscopic properties that differentiate them from the other two macrocyclic families. Moreover, their synthesis allows for precise tuning of their physicochemical properties, as peripheral functionalization with heteroatoms can be readily achieved—an approach that is generally more challenging in porphyrins.

1.6.1 Thioalkyl porphyrazines: General features

In recent years, the research activity of the group in which this thesis was carried out has focused on a subclass of porphyrazines, namely thioalkyl-substituted porphyrazines (Figure 1.6.4), which are peripherally functionalized with thioether moieties and exhibit promising properties for organic photovoltaic (OPV) applications.[52,53,54]

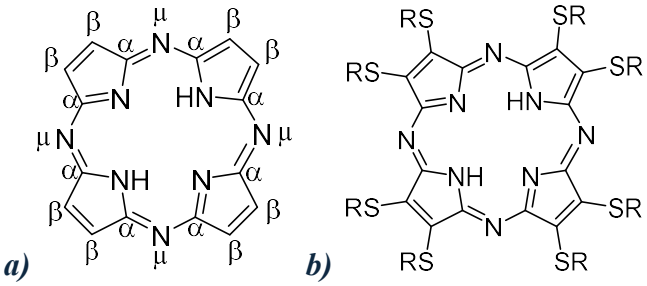

Figure 1.6.4 *(a) general structure of porphyrazine with position name(b)general structure of a thioalkyl-porphyrazine (R = alkyl).*

The presence of sulfur atoms at the β-positions imparts distinctive spectroscopic and electrochemical properties to these molecules. Moreover, it promotes the formation of coordination sites above and below the macrocyclic plane, favoring the self-assembly into discotic liquid-crystalline mesophases, particularly in metal complexes with Cu, Zn, Co, and Ni.[52] This behavior arises from the lone pairs of the sulfur atoms, which enable axial coordination to the metal center of adjacent macrocycles. As a result, one thioalkyl porphyrazine molecule can coordinate to another located above or below the molecular plane, as illustrated in Figure 1.6.5. Comparative studies on different thioalkyl porphyrazines have shown that longer alkyl side chains enhance the stability of the mesophases.

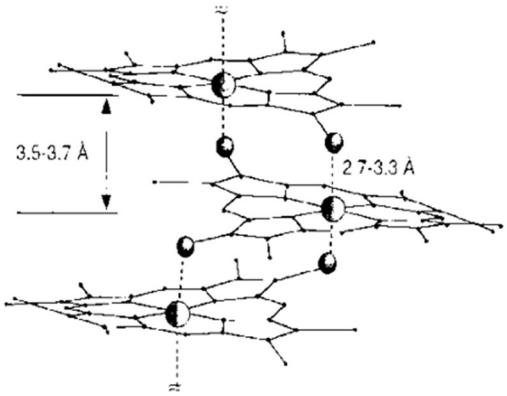

Figure 1.6.5 *Sulphur-metal interaction up and under the molecular plane in thioalkyl porphyrazines metal complexes.*

One of the advantages of using thioalkyl-porphyrazines is that these molecules are a panchromatic light absorber, this means that the thioalkyl porphyrazines absorption spectrum covers the whole visible part of the light spectrum. Considering the UV-Vis absorbance spectrum of porphyrins or phthalocyanines, they display narrow and strong ($\varepsilon \sim 3 \div 6 \times 10^5$ $cm^{-1}M^{-1}$) absorption bands at about 400 and 600 nm, but only 10% of the overall absorption is in the 450-650 nm region, where the solar emission reaches its maximum (Figure 1.6.6 left).[55] The presence of sulphur atoms in thioalkyl porphyrazines gives rise to a new electron transition involving the sulphur non-bonding electrons and falling in the 450-550 nm region of the spectrum with a wide absorption band.[56] In general, as shown in Figure 1.6.6 (right), thioalkyl porphyrazine has weaker but much wider absorption bands ($\varepsilon \sim 1 \div 5 \times 10^4$ $cm^{-1}M^{-1}$).

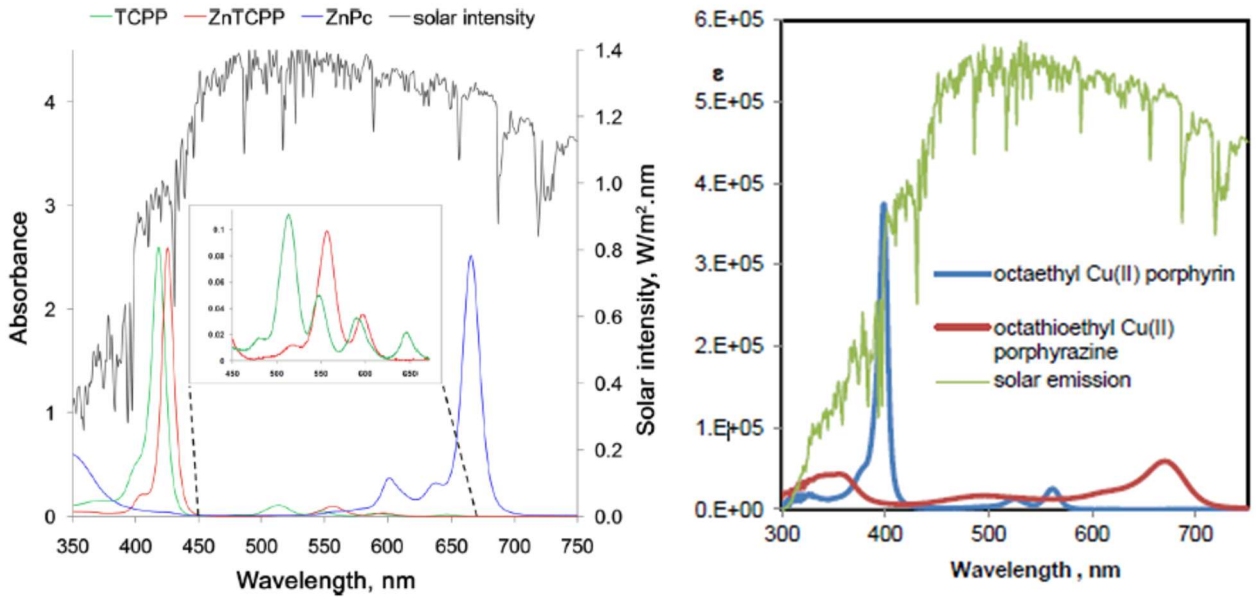

Figure 1.6.6 (left) *Normalized absorption spectra of porphyrin (green and red) and phthalocyanine (blue line) compared to the solar emission spectrum (black line)* ***(right)***[55] *comparison between porphyrin and thioalkyl-porphyrazine and solar emission spectrum.*

1.6.2 Thioalkyl porphyrazine in OPV

Unlike the more extensively studied porphyrins and phthalocyanines, porphyrazines have received comparatively limited attention, and only a few examples of their application in organic photovoltaics have been reported. Recently, Mori *et al.*[57] described thiophene-fused porphyrazines, which can, however, be considered closer to heterocyclic phthalocyanines. Subsequently, in 2018, Torres *et al.* [58] reported the use of alkyl-substituted porphyrazines with benzo-fused rings as sensitizers in DSSCs. More recently, the research group in which this thesis was carried out investigated a pyrene monosubstituted thioalkyl porphyrazine (**PzPy**, Figure 1.6.7), specifically designed for application in bulk heterojunction (BHJ) solar cells. The pyrene moiety acts as an efficient chromophore due to its extended π-conjugated system[54] and, for the same reason, enables strong non-covalent interactions with nanocarbon acceptors such as single-walled carbon nanotubes (SWNTs) and graphene nanoflakes (GNFs).

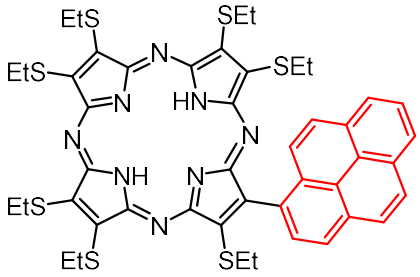

***Figure 1.6.7** Structure of pyrene monosubstituted thioalkyl-porphyrazine (**PzPy**).*

A supramolecular approach, based on non-covalent interactions between the pyrene moiety and nanocarbon structures, was adopted in order to preserve the sp^2 network of the nanocarbons and, consequently, their electronic properties. Nanohybrids composed of **PzPy** and nanocarbon materials were therefore prepared, and their photoresponse was investigated.[59] The **PzPy**/GNF system exhibited a slightly lower photoresponse compared to **PzPy**/SWNT, indicating a more effective interaction between the porphyrazine and the carbon nanotubes, as shown in Figure 1.6.8.

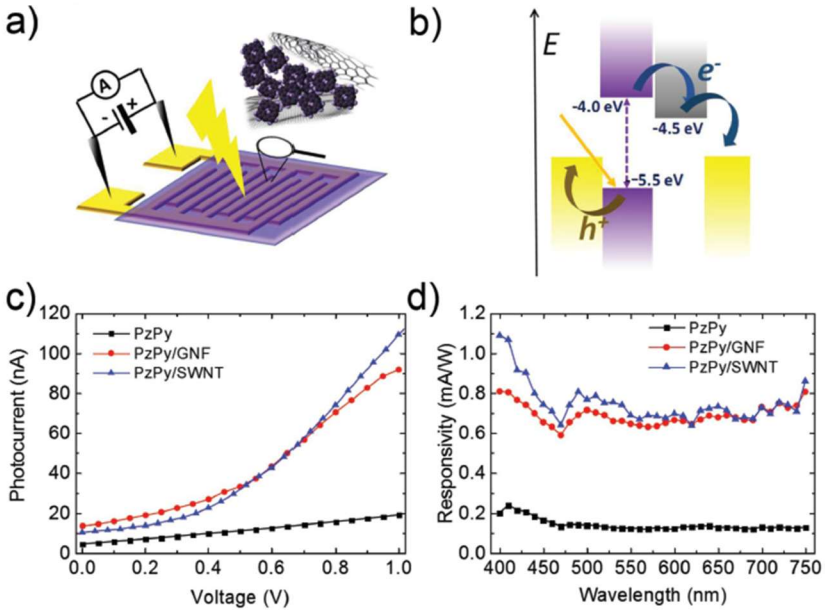

Figure 1.6.8 *(a) Schematic representation of the photodetector. (b) Energy levels diagrams and photodetector working principle. (c) Generated photocurrent in* ***PzPy*** *and in nanohybrids under 500 nm light irradiation. (d) Spectral response in* ***PzPy*** *and nanohybrids at constant voltage of 1V.*

The stronger interaction between **PzPy** and SWNTs can be explained by the molecular conformation of the porphyrazine. Structural studies have shown that rotation around the single C–C bond connecting the pyrrolic unit to the pyrene moiety is hindered. As a result, the pyrene unit is tilted with respect to the macrocycle, disrupting planarity and giving rise to an atropisomeric structure with axial chirality. This induced axial chirality plays a key role in supramolecular interactions, as SWNTs themselves possess intrinsic chirality. The chiral matching between the porphyrazine and the nanotubes likely enhances their interaction, leading to improved photoresponse.

However, the enantiomers of the pyrene-substituted porphyrazine were configurationally unstable at room temperature, having a rotational barrier of about 22.0 kcal mol^{-1}. Therefore, a new porphyrazine scaffolds conjugated with extended aromatic moieties endowed with stable inherent chirality like helicenes was investigated. In fact, these moieties join an aromatic structure suitable to establish attractive π–π interactions with nanocarbons with helical chirality, a structural feature providing interesting properties for optoelectronic applications[60] and organic light-emission diodes (OLEDs), but still they have been rarely explored in organic photovoltaics.[61] Building on these findings, the research group further developed a chiral, non-symmetrically substituted thioalkyl porphyrazines Pd(II) and Ni(II) metal complexes **PdPzHelix** and **NiPzHelix** incorporating 2-ethynyl-[6]helicene as a substituent (Figure 1.6.9).[62]

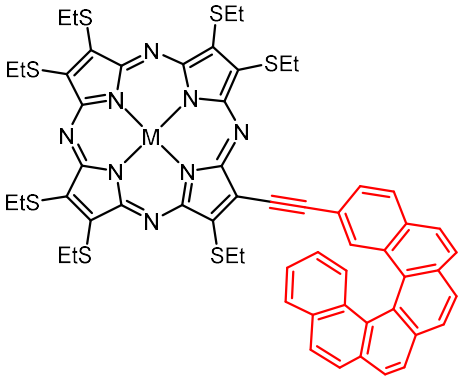

Figure 1.6.9 *Structure of 2-ethynyl-[6]-helicene substituted thioalkyl porphyrazine* ***PdPzHelix*** *and* ***NiPzHelix*** *(M= Ni, Pd).*

From the analysis of the two metal complexes, the UV–Vis absorption spectra revealed a red shift of the absorption maxima, attributed to the interaction between the porphyrazine macrocycle and the aromatic helicene moiety. Fluorescence measurements showed a broader and more intense emission band in the 400–550 nm range upon excitation at 350 nm, compared to the symmetrical thioalkyl porphyrazine complex. Moreover, the Pd complex exhibited an emission intensity approximately 60% higher than that of the Ni analogue.

Electrochemical characterization by cyclic voltammetry (CV) and differential pulse voltammetry (DPV) indicated an energy gap of about 1.6 eV, with HOMO and LUMO energy levels of −5.4 eV and −3.8 eV, respectively. These values confirm the suitability of these molecules for applications in bulk heterojunction (BHJ) solar cells.[63]

The research group in which this thesis was carried out also reported the photovoltaic performance of a β-hydroxyphenyl-substituted porphyrazine **NiPzPhOH** (Figure 1.6.10). This compound was tested as a dye in a TiO_2-based DSSC, representing only the second reported example of a DSSC employing alkylthio porphyrazines. [54] The device exhibited a power conversion efficiency (PCE) of 0.052%. Although hydroxyl groups are less effective than carboxylic groups for electron injection into TiO_2, the observed PCE is 2.6 times higher than that reported for a structurally related carboxy-derived benzofused thioethyl porphyrazine.[58]

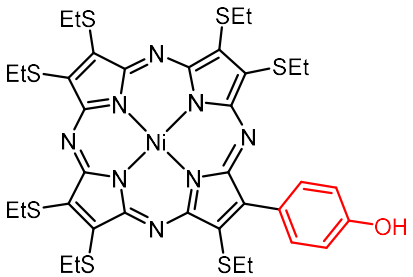

Figure 1.6.10 *Structure of β-hydroxyphenyl substituted thioethyl porphyrazine* ***NiPzPhOH****.*

Further experiments to improve the dye anchoring to the TiO_2 surface of the electrode were carried out. In particular, carboxyphenyl thioethyl porphyrazine **PzPhCOOH** in Figure 1.6.11, bearing a better carboxyl anchoring group was synthesized designed.

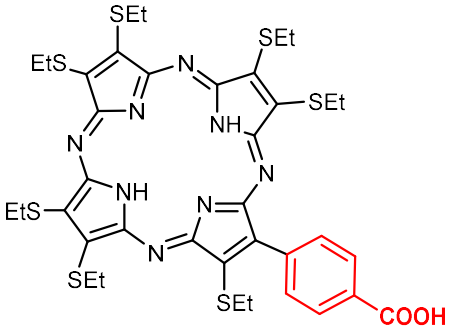

Figure 1.6.11 *Structure of β-carboxyphenyl substituted thioethyl porphyrazine* ***PzPhCOOH****.*

The synthesized carboxyphenyl thioethyl porphyrazine **PzPhCOOH** was employed as a sensitizing dye in DSSC-type solar cells based on TiO_2.[64] Device fabrication and photogeneration measurements were carried out by the research group of Prof. F. Tessore (University of Milan). Upon illumination under a one-sun solar simulator (AM 1.5G), photocurrent generation was observed. The power conversion efficiency (PCE) obtained for this porphyrazine was approximately six times lower than that of the previously studied hydroxyphenyl derivative (0.0094% vs 0.053%). However, several factors must be considered when evaluating this apparently unfavorable result. Although the present "free-base" porphyrazine contains a –COOH group, which is generally more effective than –OH for anchoring to TiO_2, the previously investigated compound was a metal complex (Ni), which may have positively influenced device performance. Indeed, the presence of a metal center in the macrocyclic cavity can enhance both the interaction with the semiconductor surface and the overall π-conjugation, thereby facilitating electron injection and improving cell efficiency.

1.7 References

1. (a) Smith, W. *Nature*, **1873**, *7*, 303; (b) Adams, W. G.; Day, R. E. *Proc. R. Soc. London*, **1876**, *25*, 113-117.
2. (a) Pochettino, A. *Acad. Lincei Rend*. **1906**, *15*, 355-368; (b) Volmer, M. *Ann. Physik*, **1913**, *345*, 775-796.
3. Kearns, D.; Calvin, M. *J. Chem. Phys.,***1958**, *29*, 950-951.
4. Delacote, G. M.; Fillard, J. P.; Marco, F. *Solid State Commun.* **1964**, *2*, 373-376.
5. Tang, C. W. *Appl. Phys. Lett.* **1986**, *48*, 183-185.
6. (a) Sariciftci, N. S.; Smilowitz, L.; Heeger, A. J.; Wudl, F. *Science* **1992**, *258*, 1474–1476; (b) Sariciftci, N. S.; Smilowitz, L.; Heeger, A. J.; Wudl, F. *Synth. Met*. **1993**, *59*, 333–352
7. Morita, S.; Zakhidov, A. A.; Yoshino, K. *Solid State Comm*. **1992**, *82*, 249–252.
8. Yu, J.; Zheng, Y.; Huang, J. *Polymers* **2014**, *6*, 2473-2509
9. Zhang, J. Du, X. Li, X. Bai, G. Deng, J. Wang, K. Qiao, J. Wang, H. Liu, Y. Huang, H. Tao, X.Gao, F. Sun, Y. *Energy Environ. Sci.* **2025**, *18*, 5378–5388.
10. Meng, D. Zheng, R. Zhao, E. Zhang, E. Leitan, D. Yang, Y. *Adv. Mater.* **2022**, *34*,2107330
11. Liang, Y.; Xu, Z.; Xia, J.; Tsai, S.-T.; Wu, Y.; Li, G.; Ray, C.; Yu, L. *Adv. Energy Mater.* **2010**, 22, E135–E138.
12. Jun Yuan, Y.; Zhang, Y.; Zhou, L.; Zhang, G.; Yip, H.-L.; Lau, T.-K.; Lu, X.; Zhu, C.; Peng, H.;Johnson, P. A.; Leclerc, M.; Cao, Y.; Ulanski, J.; Li, Y.; Zou, Y. *Joule* **2019**, *3*, 1140–1151
13. Liu, Q.; Jiang, Y.; Jin, K.; Qin, J.; Xu, J.; Li, W.; Xiong, J.; Liu, J.; Xiao, Z.; Sun, K.; Yang, S.; Zhang, X.; Ding, L. *Sci. Bull.* **2020**, *65*, 272–275.
14. (a) Yuan, S.; Luo, W.; Xie, M.; Peng, H. *RSC Advances* **2025**, *15*, 2470–2489; (b) Langa, F.; de la Cruz, P.; Sharma,G. D. *ChemSusChem* **2025**, *18*, e202400361
15. O'Regan, B.; Grätzel, M. *Nature* **1991**, *353*, 737-740
16. NREL Record Efficiency Chart: https://www.nlr.gov/pv/cell-efficiency
17. S. Mathew, A. Yella, R. Humphry-Baker, B. F. E. Curchod, N.Ashari-Astani, I. Tavernelli, U. Rothlisberger, M. K. Nazeer-uddin, M. Grätzel, *Nat. Chem.* **2014**, *6*, 242– 247.
18. L. Zhang, X. Yang, W. Wang, G. G. Gurzadyan, J. Li, X. Li, J.An, Z. Yu, H. Wang, B. Cai, A. Hagfeldt, L. Sun, *ACS Energy Lett.* **2019**,*4*, 943–951
19. Hsiao, Y-C.; Wu, T.; Li, M.; Liu, Q.; Qin, Q.; Hu, B. *J. Mater. Chem. A* **2015**, *3*, 15372–15385
20. Kojima, A.; Teshima, K.; Shirai, Y.; Miyasaka, T. *J. Am. Chem. Soc.* **2009**, *131, 17,* 6050-6051
21. Jung, M.; Kim, Y. C.; Jeon, N. J.; Yang, W. S.; Seo, J.; Noh, J. H.; Il Seok, S.; *ChemSusChem,* **2016**, *9*, 2592.
22. Li, G., Zhang, Z., Agyei-Tuffour, B.; Wu, L.; Gries, T. W.; Prashnanthan, K.; Frohloff, L.; Musiienko, A.; Li, J.; Zhu, R.; Hart, L. J. F.; Wang, L.; Li, Z.; Hou, B.; Koch, N.; Saba, M.; Barnes, P. R. F.; Nelson, J.; Dyson, P. J.; Nazeeruddin, M. K.; Li, M.; Abate, A. *Nat. Photon.***2026** ,*20*, 55–62
23. Heo, J. H. ; Im, S. H.; Noh, J. H.; Mandal, T. N.; Lim, C.-S.; Chang, J. A.; Lee, Y. H.; Kim, H.-J.; Sarkar, A.; Nazeeruddin, M. K.; Grätzel, M.; Seok, S. I. *Nat. Photonics* **2013**, *7*, 486–491.

24. Hu, M.; Bi, C.; Yuan, Y.; Xiao, Z.; Dong, Q.; Shao, Y.; Huang, J. *Small* **2015**, *11*, 2164–2169.

25. Hirasawa, M.; Ishihara, T.; Goto, T.; Uchida, K.; Miura, N. *Phys. B* **1994**, *201*, 427–430.

26. Frost, J. M.; Butler, K. T.; Brivio, F.; Hendon, C. H.; van Schilfgaarde, M.; Walsh, A. *Nano Lett.* **2014**, *14*, 2584–2590.

27. Zhang, C.; Sun, D.; Sheng, C.-X.; Zhai, Y. X.; Vardeny, Z. V. *Nat. Phys*. **2015**, *11*, 427–4

28. Geisz, J. F.; France, R. M.; Schulte, K. L.; Steiner, M. A.; Norman, A. G.; Guthrey, H. L.; Young, M. R.; Song, T.; Moriarty, T. *Nature Energy* **2020**, 5, 326–335

29. Li, N.; Niu, X.; Dong, Z.; Hu, J.; Luo, R.; Yang, S.; Zhou, Q.; Shi, Z.; Chen, J.; Du, X.; Kai Lee, L.; Wang, Y.; Guo, X.; Wang, X.; Qiu, C.; Lin, M.; He, R.; Zhang, X.; Chen, Y.; Wu, M.; Hou, Y.; *Science,* **2025**, *390*, 6779

30. Al-Ezzi, A.S.; Ansari,M.N.M. *Appl. Syst. Innov*. **2022**, *5*, 67.

31. Wang, J.; Xie, Y.; Chen, K.; Wu, H.; Hodgkiss, J. M.; Zhan, X. *Nat Rev Phys* **2024**, *6*, 365–381

32. Organic Photovoltaics: Mechanisms, Materials, and Devices; Sun, S. -S., Sariciftci, N. S., Eds.; Taylor & Francis: Boca Raton, FL, 2005

33. Solak, E. K.; Irmak, E. *RSC Adv.*, **2023**,*13*, 12244-12269

34. https://www.pveducation.org/

35. Mazzio, K. A.; Luscombe, C. K. *Chem. Soc. Rev.* **2015**, *44*, 78-90.

36. Abubaker, S. A.; Pakhuruddin, M. Z., *Energy Technology*., **2024**, *12*, 2400285

37. Piradi, V.; Yan, F.; Zhu, X.; Wong, W. Y. *Materials Chemistry Frontiers*., **2021**,7119–7133.

38. Muchuweni E.; Mombeshora E. T.; Martincigh B. S.; Nyamori V. O. *Front. Chem.,* **2022,** *9*, 733552.

39. (a) Das S.; Pandey, D.;Thomas, J.; Roy, T.; *Adv. Mater.* **2019**, *31*, 1802722; (b) Bonaccorso, F.; Balis, N.; Stylianakis, M. M.; Savarese, M.; Adamo, C.; Gemmi, M.; Pellegrini, V.; Stratakis, E.; Kymakis, E. *Adv. Funct. Mater.* **2015**, *25*, 3870–3880

40. Lee, M.; Hwang, E.; Kim, T.; Kwon, T. H.; *Bull. Korean Chem. Soc*., **2024**;*45,* 664–674

41. Abdulsalami, I. O.; Omobhude, I. A.; Abdulsalami, B. A.; Younas, M.; Semire, B.; Bello, I. A., *Discov. Chem.*, **2026**, *3*, 87

42. Hagfeldt, A.; Boschloo, G.; Sun, L.; Kloo, L.; Pettersson, H. *Chem. Rev*. **2010**, *110*, 6595–6663

43. Brogdon, P.; Cheema, H.; Delcamp, J. H.; ChemSusChem., **2018**, *11*, 86.

44. Hamad, O.A.; Kareem, R.O.; Omer, P.K.; *J. Chem. Rev.*, **2024**, *6(1)*, 39-75.

45. Koifman, O. I.; Ageeva, T. A. *Polym. Sci. Ser. C*, **2014**, *56*, 89-110

46. Qin, Y.; Luo, D.; Zhang, M.; Wong, W. Y.; *Advanced Materials,* **2026,** e18393.

47. A. Zhang, C. Li, F. Yang, J. Zhang, Z. Wang, Z. Wei, W. Li, *Angew. Chem. Int. Ed.* **2017**, *56*, 2694.

48. Reis, M. J. A.; Pereira,A. M. V. M.; Moura, N. M. M.; Neves, M. G. P. M. S.; *ACS Omega* **2024**, *9*, 31196−31219

49. (a) Liu, Z.; Wang, X.; Ge, H.; Li, A.; Wang, X. F.; *Energy Fuels,* **2024**, *38, 15*, 13685–13703; (b) S. Wu and J. Cao, *J. Coord. Chem.*, **2022**, 1–26

50. Hayashi, H.; Nihashi, W.; Umeyama, T.; Matano, Y.; Seki, S.; Shimizu, Y.; Imahori, H. *J. Am. Chem. Soc.,* **2011**, *133*, *28*, 10736–10739

51. Sekaran, B; Misra, R.; *CoordinationChemistryReviews*, **2022**, *453*, 214312

52. Belviso, S.; Ricciardi, G.; Lelj, F.; *J. Mater. Chem.*, **2000**, *10*, 297-304

53. Belviso, S.; Amati, M.; Rossano, R.; Crispini, A.; Lelj, F*., Dalton Trans.,* **2015***, 44*, 2191,

54. Belviso, S.; Santoro, E.; Penconi, M.; Righetto, S.; Tessore, F.; *J. Phys. Chem. C,* **2019**, *123*, 13074

55. Walter, M. G.; Rudine, A. B. ; Wamser, C. C. *J. Porphyrins Phthalocyanines* **2010**, *14*, 759–792 ;

56. Ghidinelli, S.; Abbate, S.; Santoro, E.; Belviso, S.; Longhi, G. *J. Phys. Chem. B*, **2021**, *125*, 264–280.

57. Mori, H.; Miyazaki, E.; Osaka, I.; Takimiya, K. *Organic Electronics* **2012**, *13*, 1975-1980.

58. Fernàndz-Ariza, J.; Urbani, M.; Rodrìguez-Morgade, M. S.; Torres, T.; *Chem. Eur. J.,* **2018**, *24*, 2618

59. Belviso, S.; Capasso, A.; Santoro, E.; Najafi, L.; Lelj, F.; Superchi, S.; Casarini, D.; Villani, C.; Spirito, D.; Bellani, S.; Del Rio-Castillo, A. E.; Bonaccorso, F. *Adv. Funct. Mater*, **2018**, *28,*1705418.

60. (a) Kim, C.; Marks, T. J.; Facchetti, A.; Schiavo, M.; Bossi, A.; Maiorana, S.; Licandro, E.; Todescato, F.; Toffanin, S.; Muccini, M.; Graiff, C.; Tiripicchio, A. *Org. Electron*., **2009**, *10*, 1511–1520; (b) Irfan, A.; Assiri, M; Al- Sehemi, A. G. *Org. Electron*., **2018**, *57*, 211–220.

61. (a) Josse, P.; Favereau, L.; Shen, C.; Dabos-Seignon, S.; Blanchard, P.; Cabanetos C.; Crassous, J. *Chem. Eur. J*. **2017**, *23*, 6277–6281. (b) Xiao, S.; Kang, S. J.; Wu, Y.; Ahn, S.; Kim, J. B.; Loo, Y.-L.; Siegrist, T.; Steigerwald, M. L.; Li H.; Nuckolls, C. *Chem. Sci.*, **2013**, *4*, 2018; (c) Lewińska, G.; Danel K. S.; Sanetra, J. *Sol. Energy*, **2016**, *135*, 848–853.

62. Belviso, S.; Marsico, G.; Franzini, R.; Villani, C.; Abbate, S.; Longhi, G., *Dalton Trans.*, **2022**, *51*, 16453–16464.

63. Xu, H.; Chen, R.; Sun, Q.; Lai, W.; Su, Q.; Huang W.; Liu, X.; *Chem. Soc. Rev*., **2014**, *43*, 3259–3302.

64. Unpublished results.

Chapter 2

Synthesis of novel thioalkyl porphyrazines for Organic Solar Cells

2.1 New thioalkyl porphyrazine for *Dye Sensitized Solar Cells*

2.1.1 Synthesis

Although only a few examples have been reported in the literature, thioalkyl porphyrazines represent promising substrates for photovoltaic applications (see Section 1.6.2).[1] Following the encouraging results previously obtained by our group with the β-hydroxyphenyl-substituted porphyrazine **NiPzPhOH**,[2] this thesis focuses on the synthesis of a new β-monosubstituted thioalkyl porphyrazine bearing a carboxy-thiophene group, **PzTCOOH**. This combination of functional moieties was considered particularly promising for several reasons. The carboxylic group can act as an anchoring unit to TiO_2, one of the most widely used semiconductors in dye-sensitized solar cells (DSSCs). At the same time, the thiophene moiety, commonly found in highly efficient polymers for organic photovoltaics,[3] introduces an electron-rich aromatic system. This feature facilitates the formation of an effective *push–pull* architecture when coupled with the porphyrazine core, potentially enhancing the photovoltaic performance of the material.

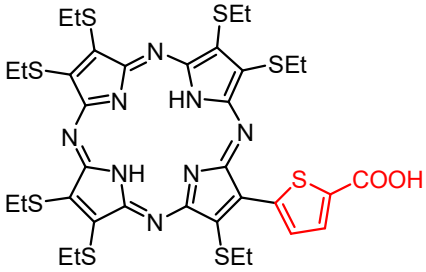

Figure 2.1.1 *Structure of 2-(4-carboxy-thienyl)-3,7,8,12,13,17,18-heptakis-(ethylthio)-5,10,15,20 porphyrazine* ***PzTCOOH****.*

All the compounds described in this chapter were synthesized starting from the symmetrically substituted *free-base* (i.e., without a metal ion in the macrocyclic cavity) thioalkyl porphyrazine **3**, (Scheme 2.1.1) which was subsequently unsymmetrized and then functionalized via cross-coupling reactions. The thioether side chain selected for the compounds investigated in this thesis is the ethyl group.

The synthesis of the symmetrically substituted octakis(thioethyl) porphyrazine (**3**) follows a general procedure reported by Schramm and Hoffman,[4] involving a magnesium-templated cyclization in an alcoholic medium, as illustrated in Scheme 2.1.1.

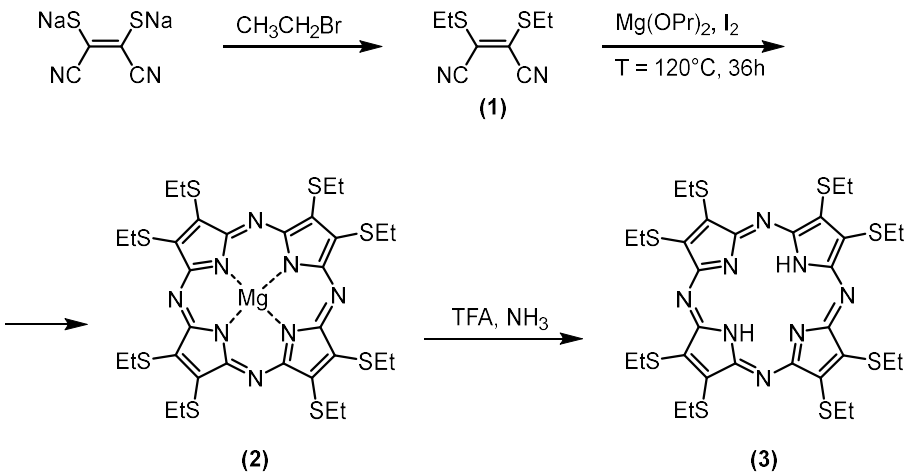

Scheme 2.1.1 *Schramm and Hoffman synthesis for symmetrical porphyrazine **3**.*

The process begins with a nucleophilic substitution reaction between the sodium salt of dicyanomaleonitrile and ethyl bromide, yielding the corresponding monomer **1**. This intermediate then undergoes template cyclization in the presence of magnesium propoxide, leading to the formation of the magnesium porphyrazine complex **2**. Subsequent treatment with trifluoroacetic acid (TFA) removes the magnesium ion from the macrocyclic cavity, affording the *free-base* porphyrazine **3**.

At this stage, compound **3** was subjected to an original asymmetrization process developed within the research group where this thesis was carried out. This reaction involves the reduction of the porphyrazine macrocycle, leading to the elimination of one thioethyl chain at the β-position of a pyrrole unit. The removed substituent is replaced by a hydrogen atom, affording the heptakis-substituted porphyrazine **4**, as shown in Scheme 2.1.2. Subsequently, compound **4** was treated with N-bromosuccinimide (NBS) in distilled chloroform, resulting in the formation of the brominated derivative **5** in nearly quantitative yield.

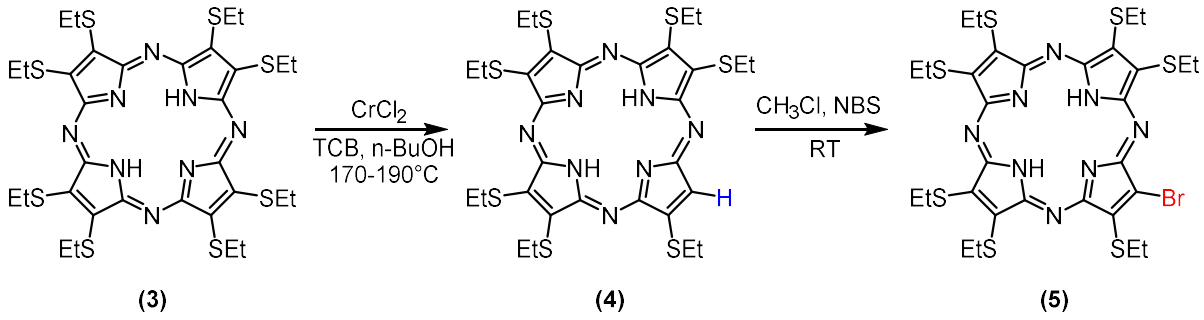

Scheme 2.1.2 *Synthesis of brominated unsymmetrically substituted porphyrazine **5**.*

Once the asymmetric porphyrazine had been obtained, attention shifted to the thienyl derivative. To prevent unwanted side reactions of the acidic function on the thiophene moiety under the basic

conditions of the cross-coupling reaction, 2-carboxy-5-boropinacolate thiophene **6** was first converted into its corresponding methyl ester **7** (Scheme 2.1.3). This transformation proceeded in high yield and required only a simple purification step, consisting of dissolution of the crude product in CH_2Cl_2 followed by filtration.

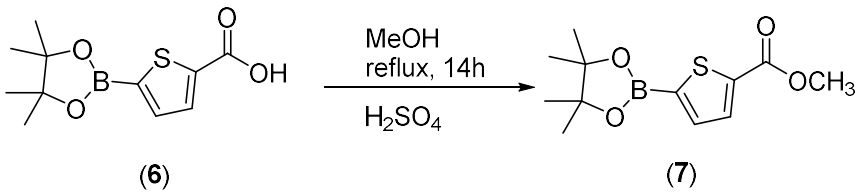

Scheme 2.1.3 *Synthesis of Methyl 5-(4,4,5,5-tetramethyl-1,3,2-dioxaborolan-2-yl)thiophene-2-carboxylate (7).*

At this point, the Suzuki-Miyaura[5] reaction (Scheme 2.1.4) was then performed on the compound **5**, heating at reflux in dry DMF/toluene (2:3, v/v) with excess (4 equivalent) of **7**, in the presence of excess of K_2CO_3 and a catalytic amount of $Pd(PPh_3)_4$ (10% mol).

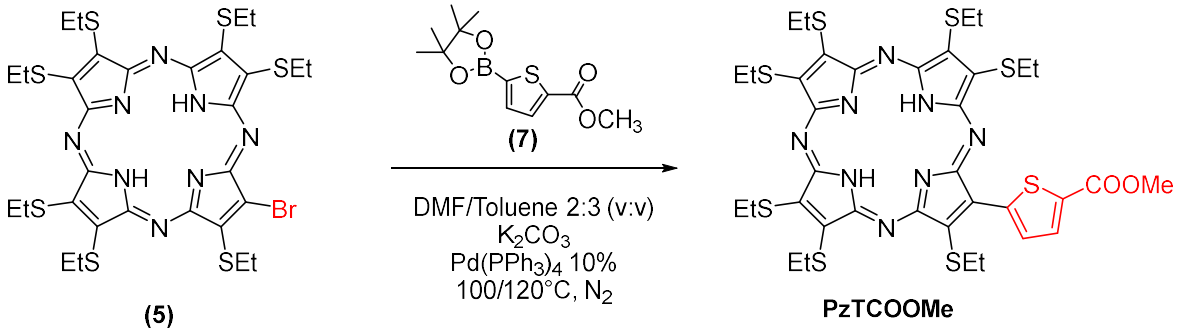

Scheme 2.1.4 *Suzuki-Miyaura Cross Coupling reaction and synthesis of* ***PzTCOOMe****.*

The Suzuki cross-coupling reaction afforded the desired product **PzTCOOMe** in 14% yield. The subsequent step involved the hydrolysis of the ester functionalities. This transformation was initially attempted by dissolving the porphyrazine in THF, with the addition of a small amount of *t*-BuOH to improve solubility, and heating the reaction mixture to 80 °C. Once the target temperature was reached, finely powdered KOH (previously ground using a mortar) was added. After 24 h, no desired product was detected. Moreover, upon acidification of the reaction mixture with 0.1 M HCl, degradation of **PzTCOOMe** was observed, with no recovery of the starting material. To overcome this issue, the base was changed to LiOH, which was added as a 1.0 M aqueous solution to the THF solution of the porphyrazine, and the reaction was initially carried out at room temperature. After 5

h, no conversion was observed; therefore, the mixture was heated to 50 °C. However, no reaction occurred under these conditions either, and only degradation products were recovered after acidification (Scheme 2.1.5). The failure of the hydrolysis can likely be attributed to a combination of poor reactivity and instability of the porphyrazine under the applied conditions. In particular, the strong basic environment (KOH or LiOH) necessary for hydrolysis may have promoted degradation of the macrocyclic thiophene-substituted system before ester cleavage could occur. Additionally, limited solubility and possible aggregation of the porphyrazine in the reaction medium may have reduced the accessibility of the ester groups to hydroxide ions, further hindering the reaction.

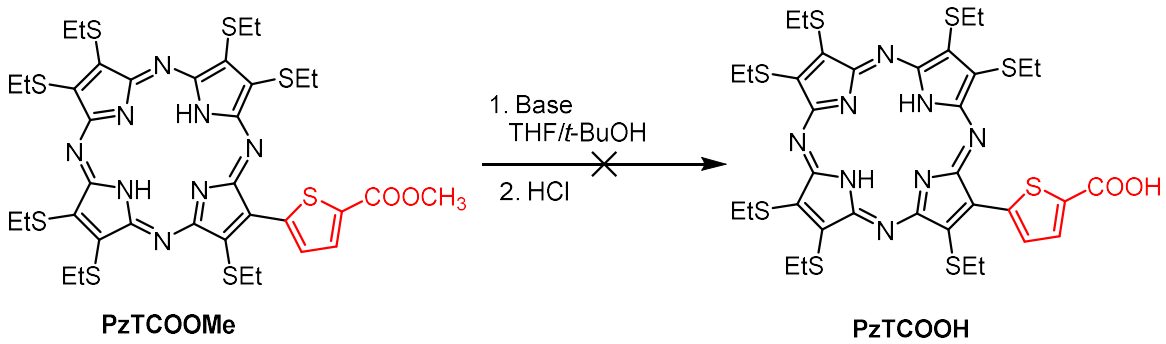

PzTCOOMe **PzTCOOH**

Scheme 2.1.5 *Base-catalyzed hydrolysis of* ***PzTCOOMe****.*

The possibility of directly introducing the aromatic system into the symmetrically substituted thioalkyl porphyrazine via the Liebeskind–Srogl coupling methodology,[6] without passing through the brominated intermediate **5**, was also investigated. This approach has been reported in the literature for the coupling of heteroaromatic thioethers and successfully applied to sulfanyl tetrapyrrolic systems.[7] It requires the use of Cu(I) thiophene-2-carboxylate (CuTC) as a co-catalyst in combination with $Pd(PPh_3)_4$.

Due to the presence of two metal species in the reaction environment, this strategy was applied to a metal complex rather than directly to the corresponding *free-base* precursor **3**, in order to avoid possible side reactions such as undesired metalation of the macrocyclic cavity. Accordingly, the coupling reaction was performed on the Pd(II) porphyrazine complex **8**. In this synthetic pathway, the first step involves the formation of the palladium complex **8** (Scheme 2.1.), obtained by reacting compound **3** with palladium acetate. In this process, palladium acetate acts not only as a metal source but also as a base, promoting the deprotonation of the inner cavity of the macrocycle and enabling the formation of the corresponding metalated species.

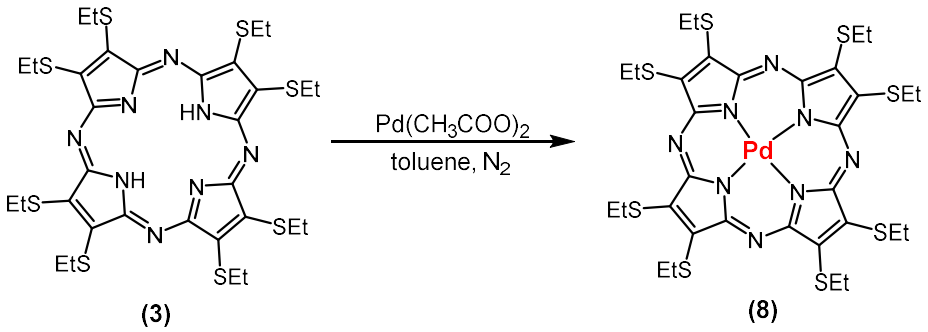

Scheme 2.1.6 *synthesis of palladium complex* ***8****.*

Once the complex had been obtained, the Liebeskind–Srogl cross-coupling reaction was performed using **7** as the boronic coupling partner Scheme 2.1.7. The presence of the ester protecting group reduces the likelihood of undesired side reactions involving the carboxylic functionality.

The reaction was carried out by dissolving the porphyrazine complex **8** in THF at 60 °C, followed by the addition of the boronic unit **7** and the catalytic system consisting of $Pd(PPh_3)_4$ and CuTC (whose structure is also shown in Scheme 2.1.7). After chromatographic purification, the coupled product **PdPzTCOOMe** was isolated in 15% yield. Also in this case, base hydrolysis of the ester moiety with KOH in THF/t-BuOH to restore the carboxylic function failed and only degradation products were recovered after the acidification with HCl 0.1M.

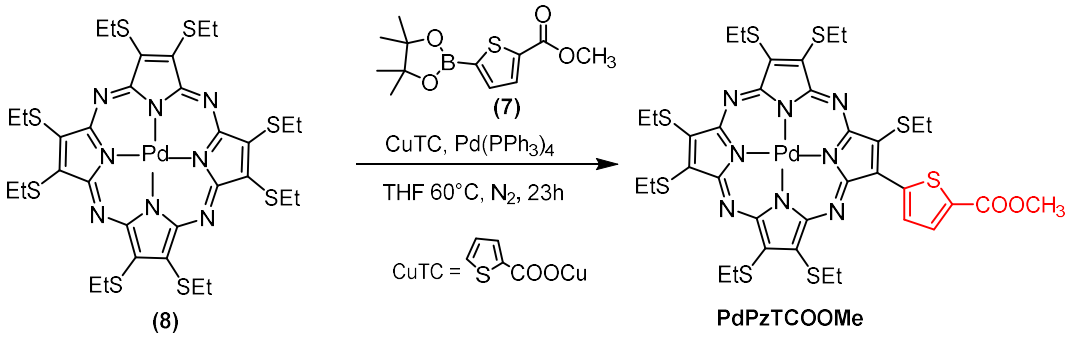

Scheme 2.1.7 *Liebeskind-Srogl cross coupling reaction.*

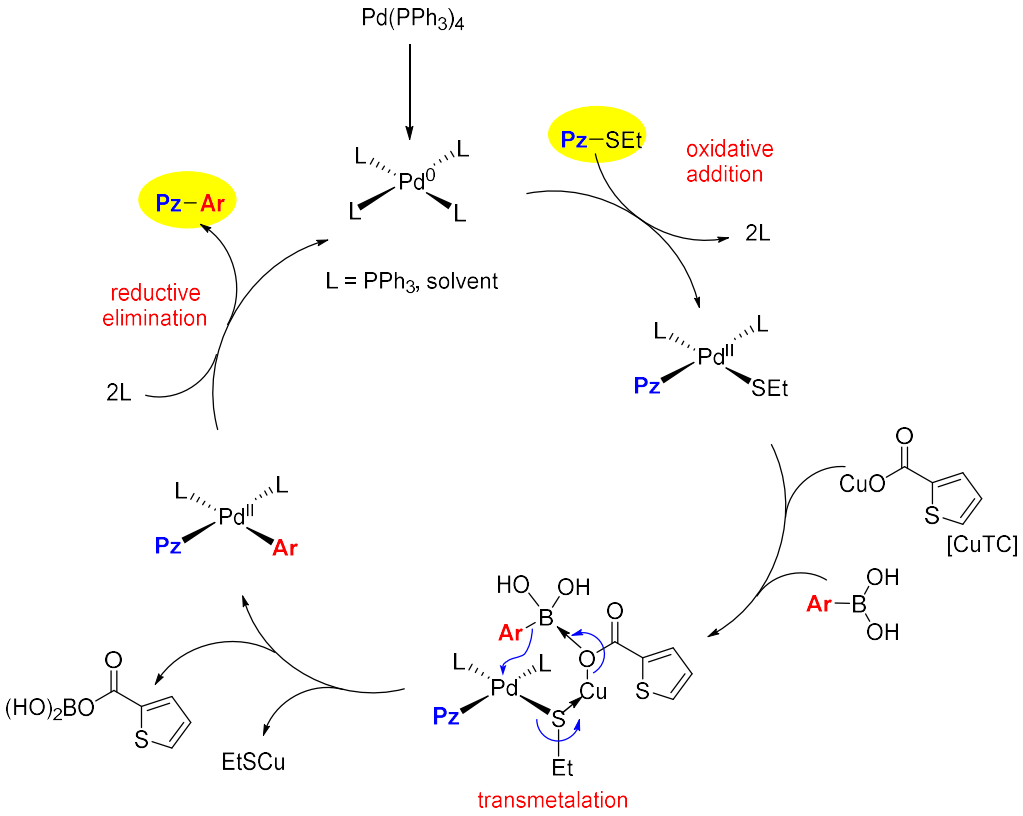

Figure 2.1.2 *Scheme of Liebeskind-Srogl cross coupling reaction mechanism.*

The mechanism proposed by Liebeskind–Srogl for this reaction is reported in Figure 2.1.2. The first and last steps of the catalytic cycle are oxidative addition and reductive elimination, respectively, as commonly observed in transition metal-catalyzed cross-coupling reactions. The key difference compared to the more conventional Suzuki coupling with boronic acids lies in the transmetalation step, which involves the CuTC salt. This neutral copper(I) salt facilitates the transfer of the boronic substituent to the palladium center while simultaneously promoting the removal of the thioether moiety. As a result, the reaction can be carried out under neutral conditions, without the need for a base, thereby avoiding possible hydrolysis of the ester functionality.

2.1.2 Characterization

The new thioalkyl porphyrazines were characterized by NMR, by MALDI-TOF and by UV-Vis.

PzTCOOMe

As shown in Figure 2.1.3, the ^{1}H NMR spectrum ($CDCl_3$) exhibits the typical pattern of a *free-base* unsymmetrically substituted thioalkyl porphyrazine. The signal at $\delta = -1.95$ ppm is diagnostic of the two inner core protons of the macrocycle. The cluster of signals around 1.5 ppm is attributed to the

terminal methyl groups of the side chains, while the multiplet signals between 3.5 and 4.5 ppm correspond to the methylene groups. The presence of the thiophene methyl carboxylate substituent is confirmed by two signals at δ = 8.03 and 8.92 ppm, assigned to the thiophene protons, and by a singlet at δ = 3.9 ppm corresponding to the methoxy group of the ester functionality.

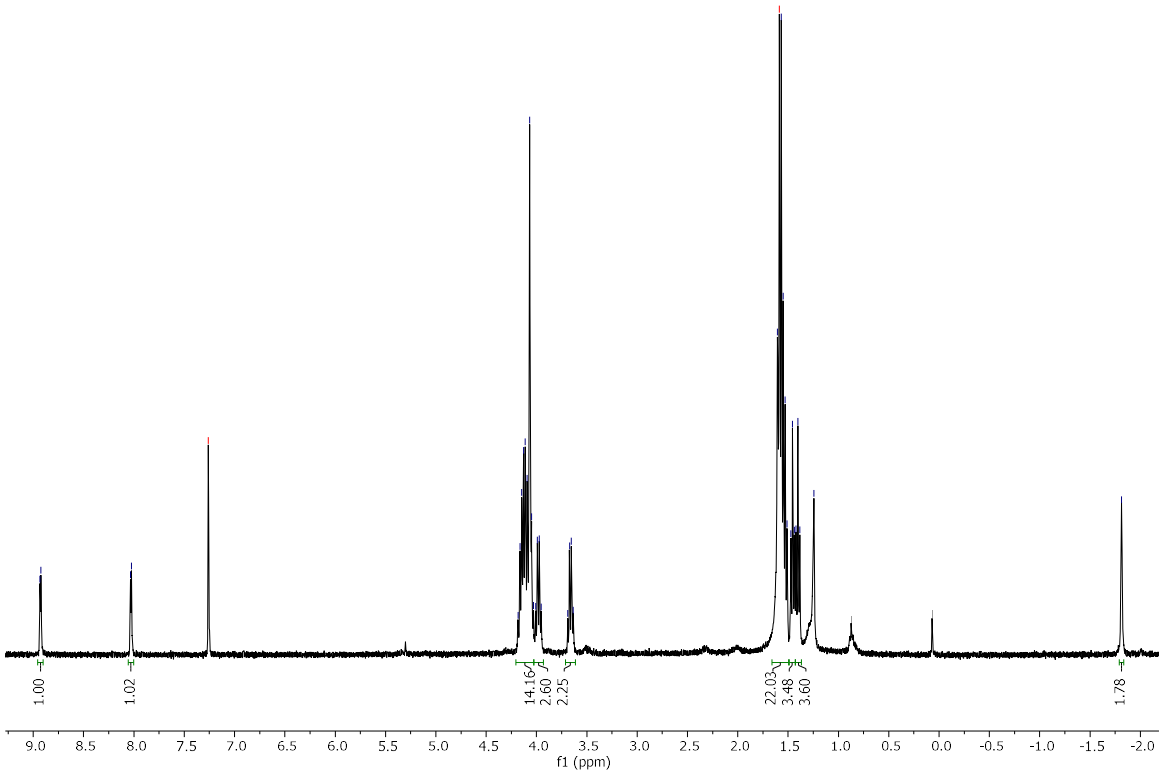

Figure 2.1.3 *^{1}H-NMR of compound* ***PzTCOOMe****.*

One other confirmation that the reaction product was the compound **PzTCOOMe** was given by the MALDI-TOF mass spectrometry where were founded the molecular peak plus two hydrogen atoms at m/z 876.17 and the molecular peak plus one sodium atom at m/z 897.14. According to the calculated exact mass for the molecule of 874.12.

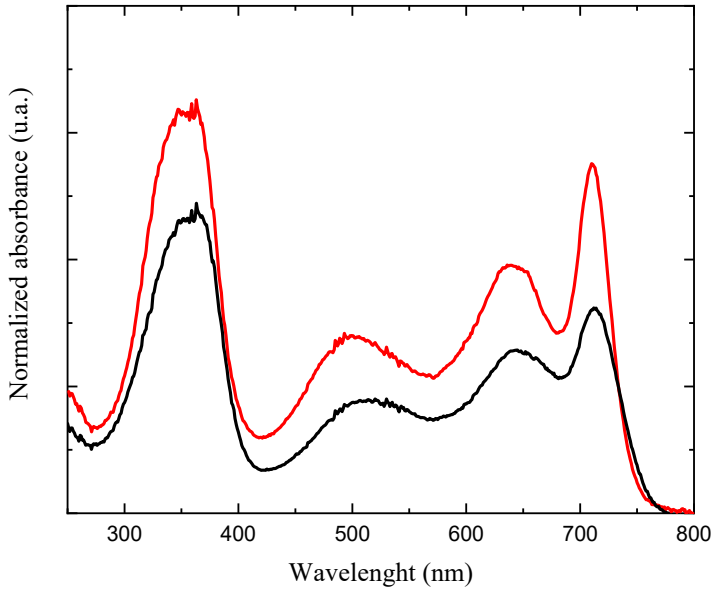

Figure 2.1.4 *UV-Vis absorbance spectrum of* ***3*** *(red line) and compound* ***PzTCOOMe*** *(black line).*

Comparison of the UV–Vis (CH_2Cl_2) spectra of staring compound **3** and **PzTCOOMe** reveals that the **PzTCOOMe** compound exhibits a red shift and an asymmetric broadening of both the Soret and Q bands. These spectral changes indicate that the thiophene moiety significantly influences the electronic structure of the macrocycle, thereby confirming its successful covalent attachment.

Compound 8

As shown in Figure 2.1.5, the ^{1}H-NMR spectrum ($CDCl_3$) is the typical spectrum of a symmetrical thioalkyl porphyrazine complex. In fact, it shows only two signals at 1.55 ppm ad 4.07 ppm respectively the terminal methyl groups of the sidechain and the methylene bridge near the sulphur in the sidechain. The confirm is in the absence of the peak at negative ppm, because the absence of the hydrogen inside the cavity of the macrocycle where the palladium is coordinated.

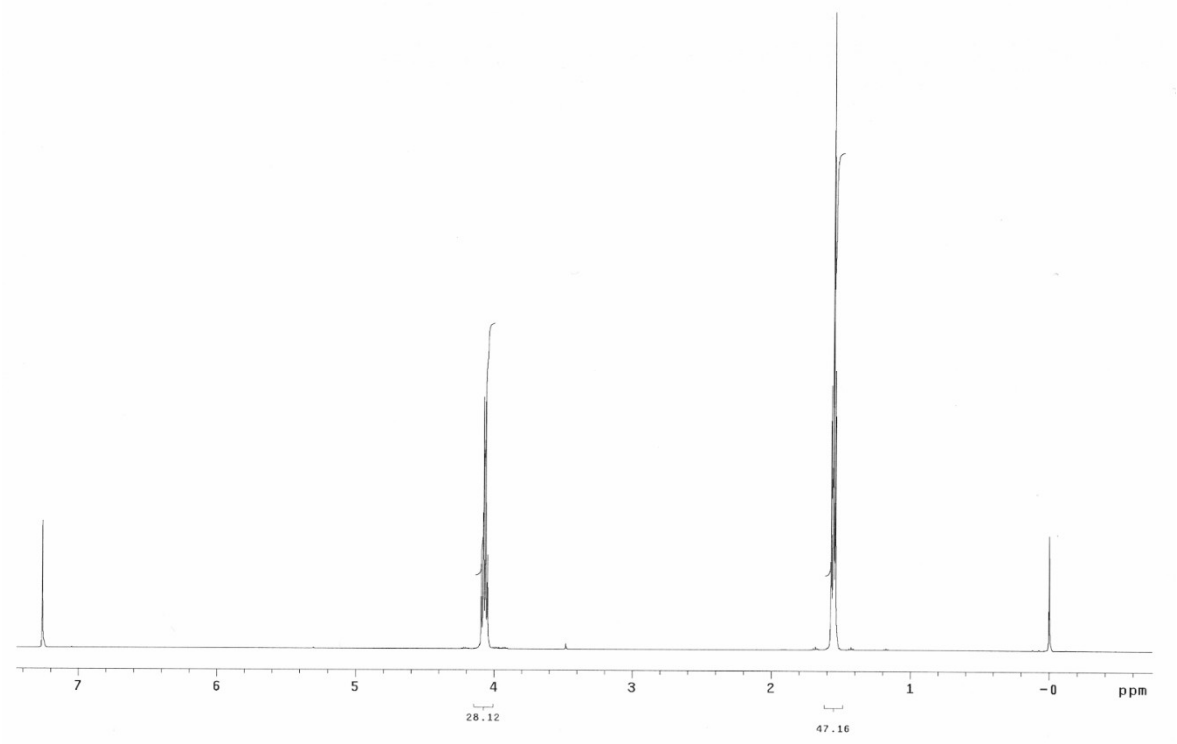

Figure 2.1.5 *^{1}H-NMR of compound **8**.*

Another confirms comes from the UV-Vis spectrum (CH_2Cl_2). In fact, the absorbance spectrum in Figure 2.1.6 (red line) shows only one band at 655 nm instead the two of the **3** spectrum. As also shown, there is a blue shift of the bands due to the modification of the energy levels due to the presence of the metal.

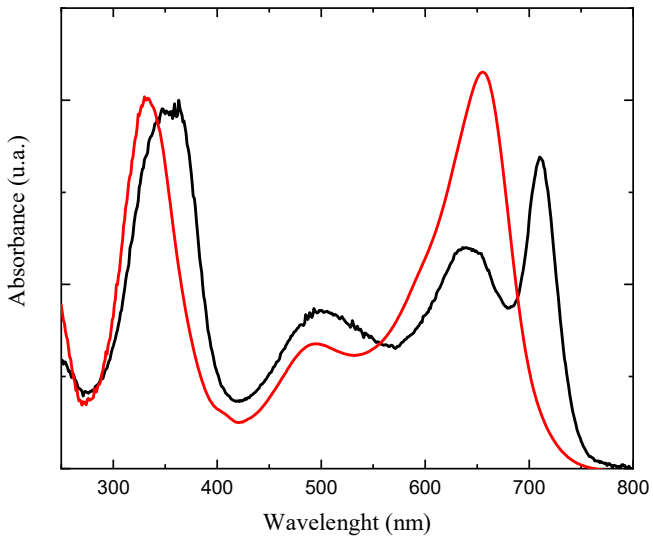

Figure 2.1.6 *UV-Vis absorbance spectrum of **3** (black line) and **8** (red line).*

PdPzTCOOMe

The ^{1}H-NMR ($CDCl_3$) spectrum (Figure 2.1.7) shows, in the 3.4–4.20 ppm region, a series of multiplets attributable to the S–CH_2 groups of the seven thioethyl chains. The differentiation of these signals, compared to symmetrically substituted porphyrazines, indicates the non-symmetrical functionalization of the macrocyclic periphery. In the 1.0–1.8 ppm region, signals corresponding to the methyl groups of the seven ethyl chains are observed. The presence of the aromatic thiophene substituent is evidenced by two broadened singlets at 8.01 and 8.86 ppm (each integrating for one proton). Additionally, a singlet at 4.02 ppm is assigned to the O–CH_3 protons of the ester group on the aromatic substituent. It is worth noting that the corresponding chemical shifts of the aromatic signals in the isolated pinacol boronate precursor **7** appear at higher field (δ = 7.55 and 7.81 ppm) compared to those observed upon β-substitution on the porphyrazine complex, due to the ring current effect exerted by the macrocycle.

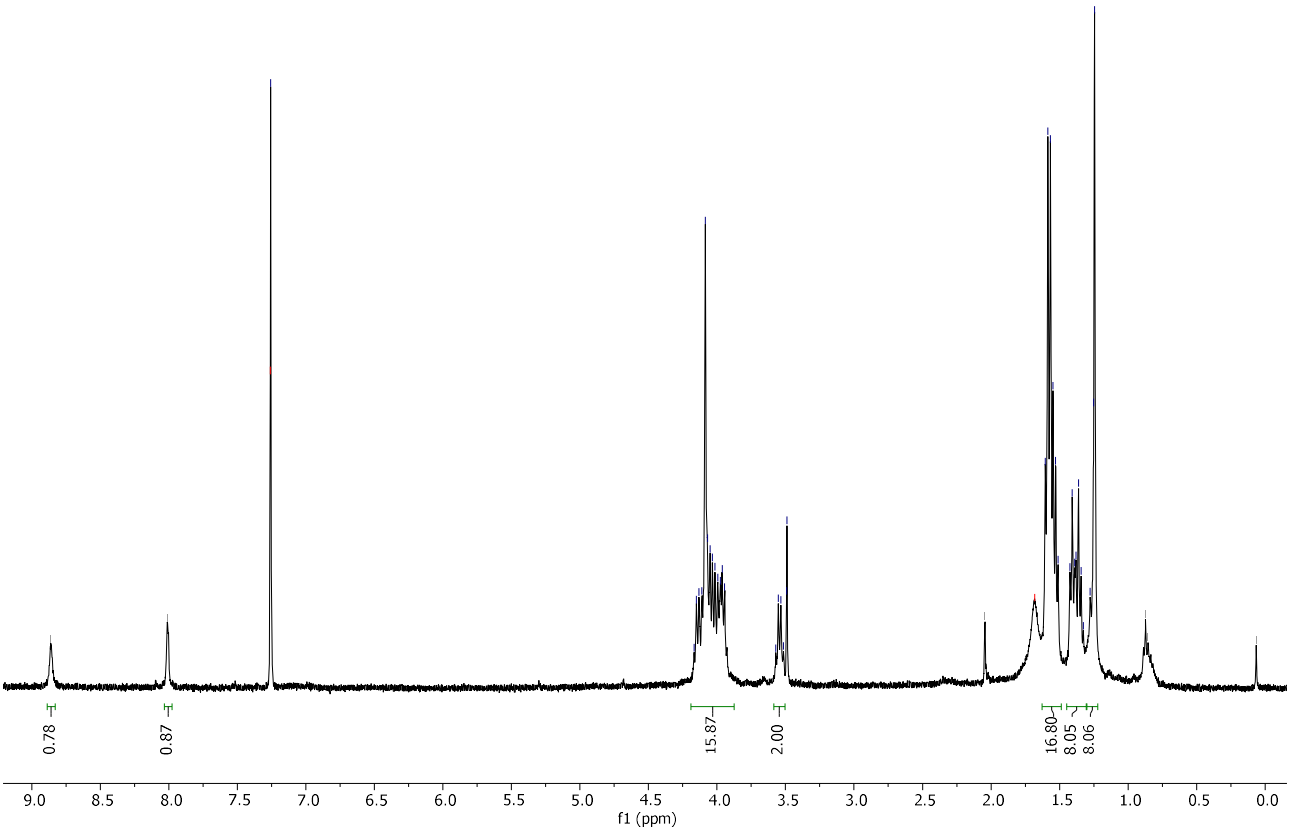

Figure 2.1.7 *^{1}H-NMR of compound* ***PdPzTCOOMe****.*

In the MALDI-TOF analysis was identified the cluster relative to the molecular peak with three more hydrogen atoms at m/z 981.14 and another important peak where the molecule lost the methyl

carboxylate and gained 5 hydrogen atoms at m/z 924.08. According to the calculated exact mass for the molecule 978.01.

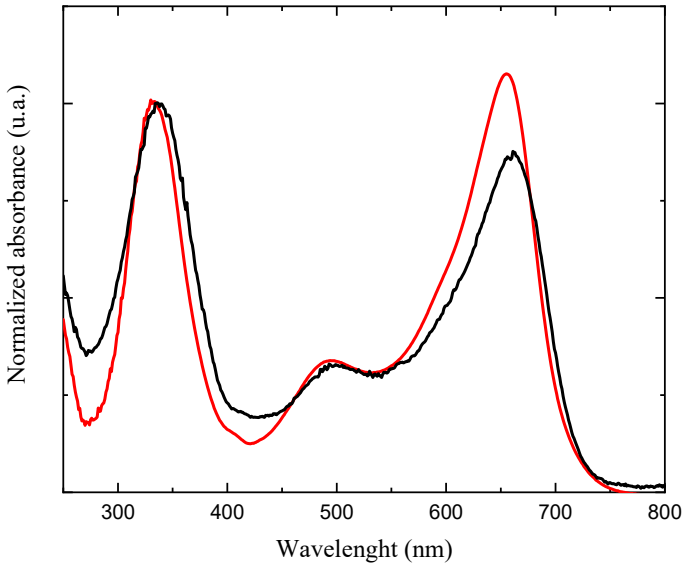

Figure 2.1.8 *UV-Vis absorbance spectrum of* ***8*** *(red line) and compound* ***PdPzTCOOMe*** *(black line).*

The newly obtained thiophene-substituted porphyrazine complex **PdPzTCOOMe** was also investigated in terms of its absorption spectroscopic properties. The UV-Vis (CH_2Cl_2) spectrum of the compound **PdPzTCOOMe** (Figure 2.1.8) is a typical spectrum of metal complex thioalkyl-porphyrazine, in fact, it shows only one Q band at 662 nm other than the extra band at 500 nm (due to the $n_{sulphur} \rightarrow \pi^*$ transitions) and the Soret band at 336 nm. Comparing the spectrum of **PdPzTCOOH** with its symmetric precursor **8** (red line in Figure 2.1.8) is observed a noticeable redshift while a slight redshift is observed for the Soret band, confirming the conjugation between the two aromatic system and that the cross coupling reaction was successful.

2.2 Thioalkyl porphyrazines for *Bulk Heterojunction solar cells*

As the aim of this PhD project is the fabrication of OPV solar cells, the pyrene-monosubstituted thioalkyl porphyrazine **PzPy** and the ethynyl-[6]helicene **PdPzHelix**, later employed in device fabrication as reported in Chapter 4, were resynthesized following procedures previously reported in the literature by the research group in which this thesis was carried out.[8, 9]

2.2.1 Synthesis

The synthetic pathway proceeds through the brominated intermediate **5** (Figure 2.2.1). The pyrene-substituted derivative[8] was obtained via a Suzuki cross-coupling reaction, whereas the ethynyl-[6]helicene[9] was synthesized through a Sonogashira cross-coupling reaction starting from the same brominated precursor.

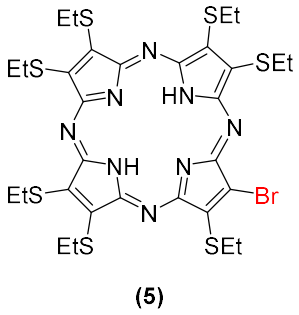

Figure 2.2.1 *Brominated compound* ***5*** *starting material for the following synthetic procedures.*

PzPy

The synthesis of pyrene derivatives goes through the Suzuki-Miyaura cross coupling reaction,[5,8] starting from the brominated non-symmetrically substituted thioethyl porphyrazine **5** heating at reflux in dry DMF/toluene (2:3, v/v) with excess (4 equivalent) of 1- pyrene- boronic acid, in the presence of excess of K_2CO_3 and catalytic amount of $Pd(PPh_3)_4$ (10% mol) obtaining the cross coupling product with a 45% yield.

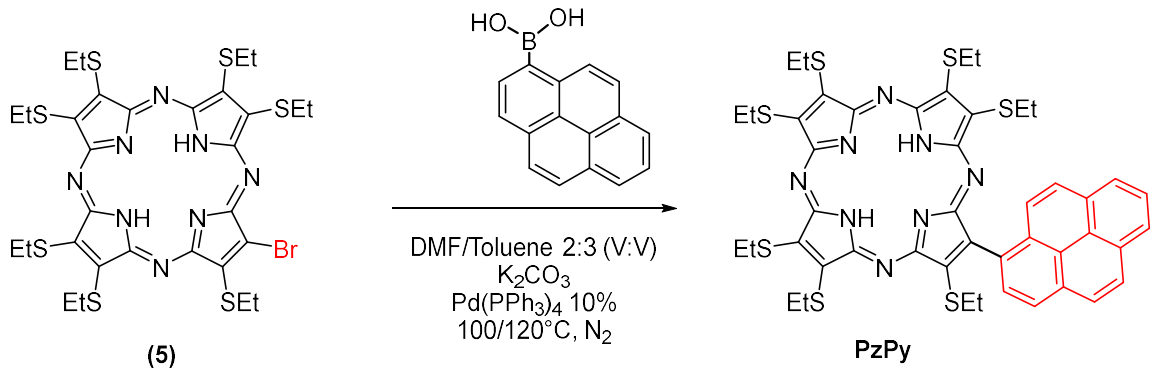

Scheme 2.2.1 *Suzuki-Miyaura cross coupling reaction and synthesis of* ***PzPy****.*

PdPzHelix

Synthesis of **PdPzHelix** goes through a longer synthetic pathway. It starts with the metalation of the brominated compound **5** to obtain the palladium complex **9** (Scheme 2.2.2).

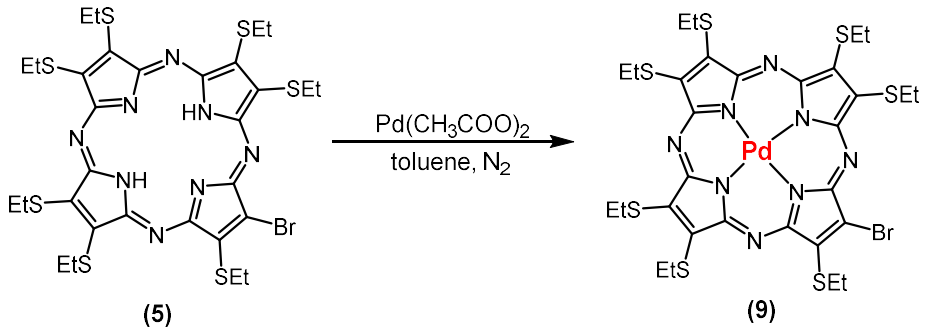

Scheme 2.2.2 *Synthesis of palladium complex* ***9****.*

Then the alkyne was prepared by Sonogashira cross coupling on 2-bromo-[6]-helicene with TMS-acetylene and then the resulting product was desilylated by treatment with TBAF in dry THF as shown in Scheme 2.2.3.

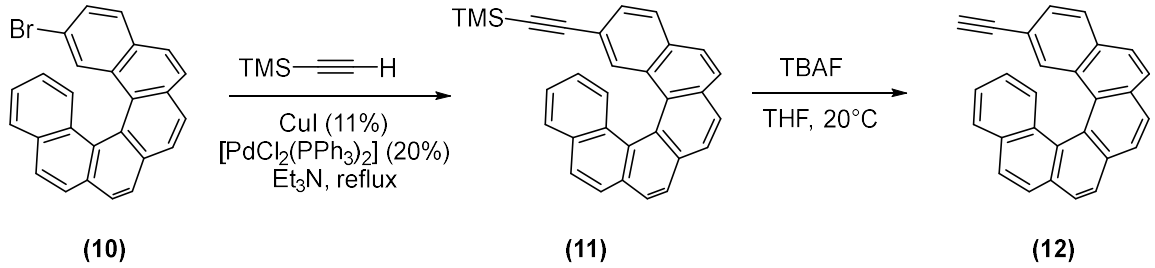

Scheme 2.2.3 *Synthesis of 2-ethinyl-[6]-helicene.*

Then, the synthesis of **PdPzHelix** was performed as follow. Compound **9** was dissolved in dry triethyl amine at reflux at the presence of little excess (1.5 equivalent) compound **12**, and catalytic amount of CuI (11% mol) and $PdCl_2(PPh_3)_2$, obtaining the desired product in a 25% yield.

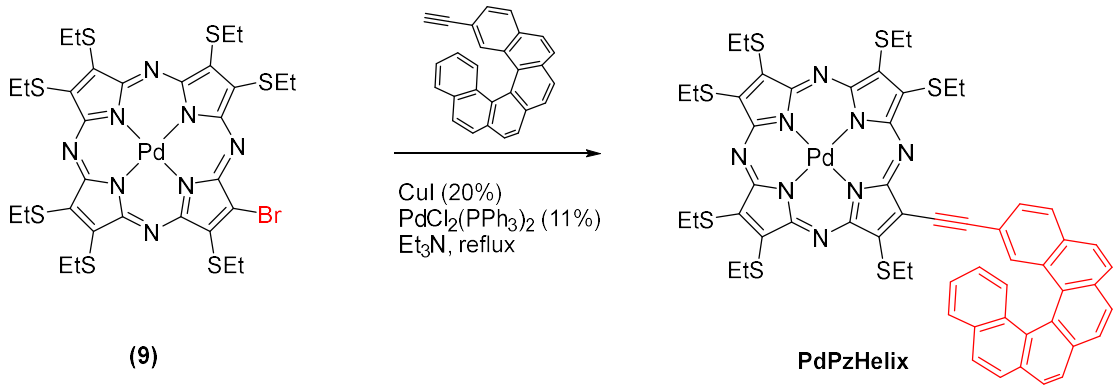

Scheme 2.2.4 *Sonogashira cross-coupling reaction and synthesis of* ***PdPzHelix****.*

2.2.2 Characterization

PzPy and **PdPzHelix** were characterized by NMR and UV-Vis absorption and compared with the one in literature[8,9] showing accordance.

PzPy

The ^{1}H-NMR ($CDCl_3$) of compound **PzPy**, shows the clusters of the non-symmetrically substituted thioethyl porphyrazines and the aromatic signals related to the pyrene unit in the aromatic region, in addition to the singlet at negative chemical shift due to the internal protons as shown in Figure 2.2.2.

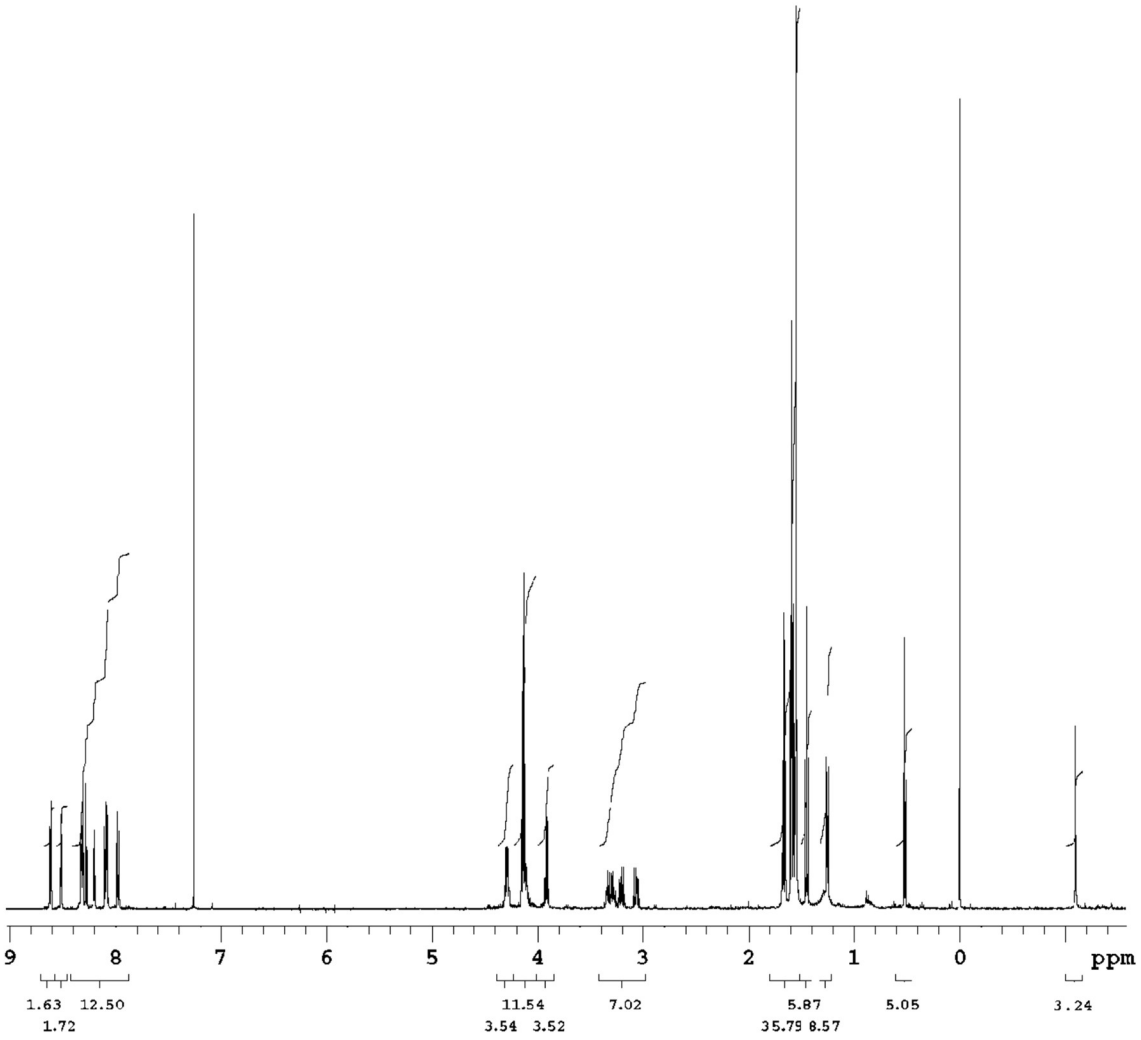

Figure 2.2.2 *^{1}H-NMR of compound* ***PzPy****.*

The UV-Vis (CH_2Cl_2) absorption (Figure 2.2.3) shows the typical spectrum for a *free base* thioethyl porphyrazine with two separated Q bands but also shows a new band in the region between 250 and 300 nm due to the pyrene absorption band.

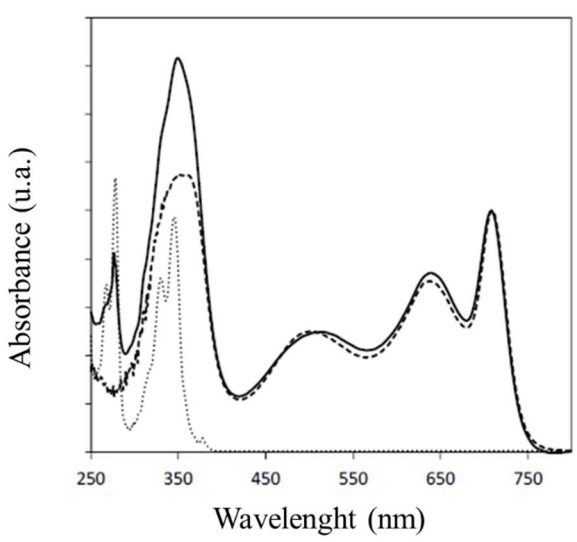

Figure 2.2.3 *UV-Vis absorption spectrum of 1-pyrene boronic acid (dot line); symmetric free-base **3** (dashed line) and **PzPy** (solid line).*

PdPzHelix

The ^{1}H-NMR ($CDCl_3$) of compound **PdPzHelix** shows the clusters of the non-symmetrically substituted thioethyl porphyrazines complexes and the aromatic signals, in the 6.7-8.2 ppm range, related to the helicene unit in the aromatic region. The singlet at negative chemical shift due to the internal protons is absent because of the presence of the metal as shown in Figure 2.2.4.

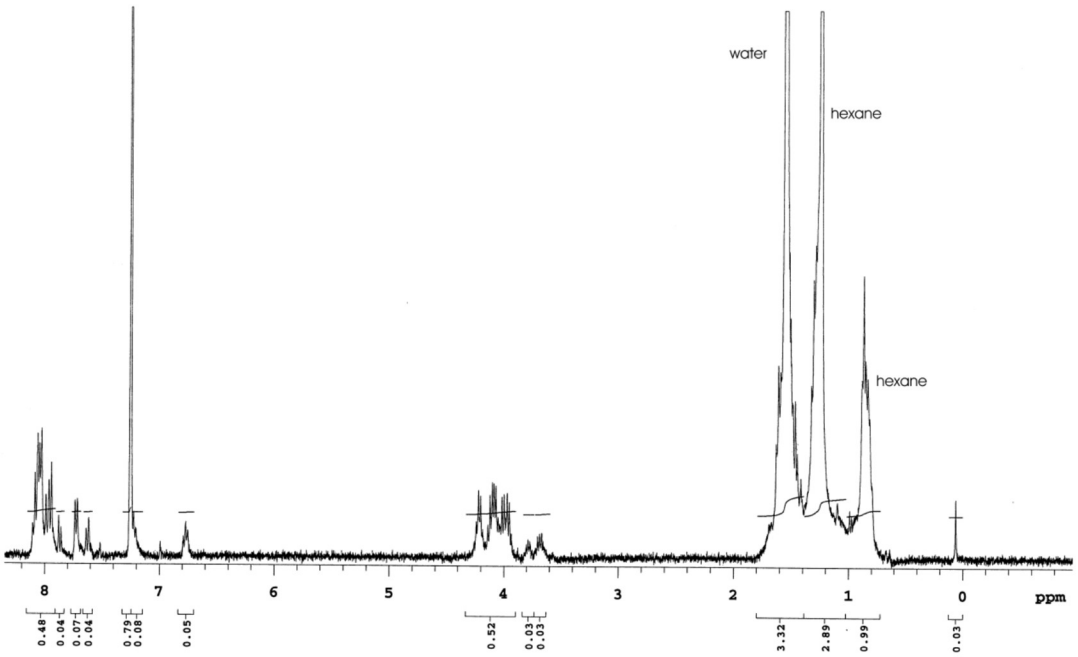

Figure 2.2.4 *^{1}H-NMR of compound **PdPzHelix**.*

The UV-Vis (CH_2Cl_2) absorption (Figure 2.2.3) shows the typical spectrum for a thioethyl porphyrazine complex with only one Q band but also shows a new band in the region between 250 and 300 nm due to the helicene absorption band.

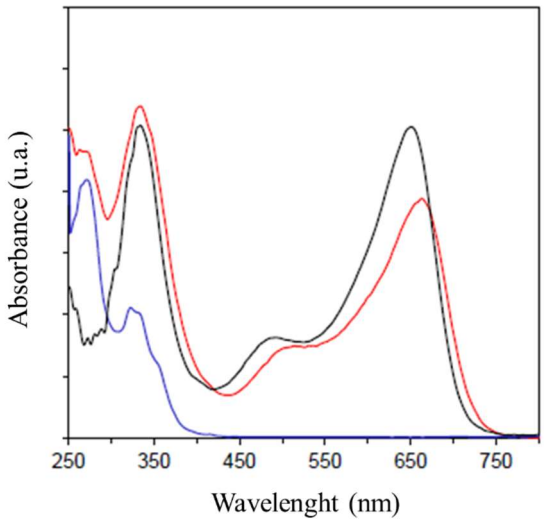

Figure 2.2.5 *UV-Vis absorbance spectrum of* ***Pd complex 9*** *(black line),* ***2-ethinyl-[6]-helicene*** *(blue line) and* ***PdPzHelix*** *(red line).*

2.3 Conclusions

Non-symmetrically substituted porphyrazines represent highly promising systems for OPV applications. This chapter discusses the synthesis and characterization of two new thioalkyl-substituted porphyrazines designed for DSSC applications, building on the favorable results previously obtained with **PzPhCOOH** and **NiPzPhOH** (described in Chapter 1).

A new thiophene methoxy ester functionalization was successfully introduced at the β-position of the porphyrazine macrocycle using two different synthetic approaches. The thiophene moiety was selected due to its widespread presence in photoactive materials, while the carboxylic acid group was chosen for its effectiveness as an anchoring group to TiO_2, the most commonly used semiconductor in DSSCs.

The first synthetic strategy follows a classical route involving asymmetrization, bromination, and Suzuki cross-coupling reactions. The second, more direct approach starts from a symmetric porphyrazine precursor and affords the non-symmetrically substituted thioalkyl porphyrazine via a Liebeskind–Srogl cross-coupling reaction. This alternative method is particularly attractive because, despite providing comparable yields in the cross-coupling step, it reduces the number of synthetic steps required to obtain the final product, thereby improving the overall yield. Unfortunately, the basic hydrolysis step was unsuccessful, likely due to a combination of low reactivity and instability of the

porphyrazine under the applied conditions. As a result, the free carboxylic acid functionality could not be obtained, preventing the evaluation of these compounds as sensitizers in DSSC devices.
This chapter also describes the synthesis and characterization of two thioalkyl porphyrazines intended for BHJ solar cell applications: a pyrene-substituted derivative and a helicene-substituted derivative, both of which were resynthesized for device testing as reported in Chapter 4.

2.4 Methods and experimental

2.4.1 General procedure

All chemicals and solvents (Aldrich) were of reagent grade. Solvents were dried and distilled before use according to standard procedures. Solvents used in physical measurements were of spectroscopic or HPLC grade. Silica gel used for chromatography was Merck Kieselgel 60 (70-230 mesh), 20x20 cm plates for thin layer chromatography (TLC) were Macherey-Nagel 0.2mm F_{254} on aluminium substrate and Merck 0.5mm or 1.0mm on glass substrate. UV-Vis spectra were registered in liquid at ~10^{-6}M in CH_2Cl_2 at room temperature, in the 250-800nm region using UV-Vis Cary 50 and 1cm quartz sample cells.

^{1}H-NMR and ^{13}C-NMR spectra were registered in $CDCl_3$ with 400MHz INOVA Varian. The MALDI-TOF MS were registered by Consorzio Interuniversitario "Istituto Nazionale Biostrutture e Biosistemi" of Università di Napoli "Federico II".

2.4.2 Synthesis

The *free-base* thioethyl porphyrazines **3**[10] their non-symmetrically H-substituted counterpart **4**[11] and the Br-substituted porphyrazines **5**[12] were prepared according to previously described procedures.

Methyl 5-(4,4,5,5-tetramethyl-1,3,2-dioxaborolan-2-yl)thiophene-2-carboxylate (7).

200 mg (0.790 mmol) of 5-(4,4,5,5-Tetramethyl-1,3,2-dioxaborolan 2-yl)thiophene 2-carboxylic acid (**6**) was dissolved in 15 mL of a mixture (30:1 v/v) of methanol and concentrated sulfuric acid. The reaction was carried out by reflux at 70°C for 20 h. The excess solvent was removed at reduced pressure, and the crude was then purified washing with CH_2Cl_2 and filtering the liquid phase. The product is a white solid. R_f = 0.25. Yield: 81%. UV-vis, CH_2Cl_2, λ_{max}/nm: 262. ^{1}HNMR (400 MHz, $CDCl_3$) δ/ppm: 1.35 (s, 12H, CH_3), 3.89 (s, 3H, -OCH_3), 7.55 (d, J= 3.7Hz, H, ArH), 7.81 (d, J= 3.7Hz, H, ArH). ^{13}C-NMR (100 MHz, $CDCl_3$) δ/ppm: 24.63 (*CH_3*), 24.74 (*CH_3*), 24.78 (*CH_3*), 24.83 (*CH_3*), 29.68 (-$OCMe_2$), 52.22 (-OCH_3), 84.58 (Ar), 133.94 (Ar) 136.88 (Ar), 139.33 (Ar), 162.59 (*C=O)*.

PzTCOOMe: ***2-(4-carboxy-thienyl)-3, 7, 8, 12, 13, 17, 18-heptakis-(ethylthio)-5, 10, 15, 20 -porphyrazine***

Brominated compound **5** (88.0 mg, 0.108mmol) was dissolved in 20mL of anhydrous DMF: toluene (2:3 v:v), degassed with nitrogen flux and heated at 100°C. Then K_2CO_3 (120 mg, 0.865mmol, 8eq.), the catalyst $Pd(PPh_3)_4$ (12.0 mg, 0.0108 mmol 10%) and **7** (115 mg, 0.432 mmol, 4eq.) were added and the mixture was left stirring at 120°C for 7h. The crude was extracted with $CHCl_3$ and water three

times and the organic phases collected and dried with anhydrous Na_2SO_4. The solvent was then removed at reduced pressure. The crude was purified with silica gel chromatography with gradient elution starting from the CH_2Cl_2:*n*-hexane (6:4) mixture (v:v) up to the CH_2Cl_2:*n*-hexane (8:2) mixture (v:v). R_f=0.15 Yield = 14%. ^{1}H-NMR (400 MHz, $CDCl_3$): δ -1.81 (s, 2H, N*H*) 1.40 (t, J=8, 3H, C*H*$_3$), 1.46 (t, J=8, 3H, C*H*$_3$), 1.51÷1.60 (m, 15H, C*H*$_3$.), 3.66 (q, J=8, 2H, SC*H*$_2$), 3.97 (q, J=8, 2H, SC*H*$_2$), 4.03÷4.18 (m, 10H, SC*H*$_2$) 4.07 (s, 3H, OC*H*$_3$), 8.03 (d, J=4, 1H), 8.92 (d, J=4, H). ^{13}CNMR (100 MHz, $CDCl_3$) δ/ppm: 14.28, 15.33, 15.72, 15.76, 15.79, 22.84, 27.87, 29.44, 29.61, 29.85, 30.91, 31.60, 52.48, 131.99, 133.64, 135.61, 136.70, 138.62, 139.96, 140.45, 140.58, 141.21, 141.50, 143.81, 163.40. UV-vis (CH_2Cl_2): λ_{max}/nm: 356 (Soret); 506 (extra band), 642 and 711 (Q bands). MALDI-MS: *m/z* 876.17 $[M+2H]^+$ (calc. per $C_{36}H_{44}N_8O_2S_8$ 876.14), *m/z* 897.14 $[M+Na]^+$ (calc. per $C_{36}H_{42}N_8NaO_2S_8$ 897.11)

***Palladium(II)-2, 3, 7, 8, 12, 13, 17, 18-octakis-(ethylsulfanyl)-5, 10, 15, 20-porphyrazinate* (8)**

Compound **3** (58 mg, 0.073 mmol) was dissolved in 12.0 mL of anhydrous toluene. $[Pd(CH_3COO)_2]$ (20.5 mg, 0.091 mmol) was then added. The reaction was carried out at reflux at 140°C in a nitrogen atmosphere for 3 hours. Once the reaction solvent was eliminated, purification was carried out by silica gel chromatography with the CH_2Cl_2 eluent mixture:*n*-hexane (1:1) (v:v). R_f = 0.43. Yield=43%. ^{1}H NMR (400 MHz, $CDCl_3$, 297 K): δ 1.55 (t, J = 7.5 Hz, 24 H, C*H*$_3$), 4.07 (q, J = 7.5 Hz, 16 H, SC*H*$_2$). ^{13}CNMR (100 MHz, $CDCl_3$) δ/ppm: 15.70, 29.67, 140.41, 145.47. UV-vis (CH_2Cl_2): λ/nm: 331 (Soret); 493(extra band), 656 (Q band). MALDI-MS: m/z 899.57 $[M+H]^+$ (calc. per $C_{32}H_{41}N_8PdS_8$ 899.03).

PdPzTCOOMe: *palladium(II) 2-(4-carboxymethyl-thienyl)-3,7,8,12,13,17, 18-heptakis-(ethylsulfanyl)-5, 10, 15, 20-porphyrazinate*

95 mg (0.11 mmol) of Pd(II) complex **8** was dissolved in 13 mL of THF. To facilitate dissolution, the reaction mixture was heated to 60 °C under magnetic stirring. Compound **7** (85 mg, 0.32 mmol) was then added, followed by the addition of the catalyst $[Pd(PPh_3)_4]$ (12 mg, 0.011 mmol, 10 mol% relative to complex 8). Subsequently, Cu(I) thiophene-2-carboxylate (CuTC) (25 mg, 0.13 mmol, 1.2 equivalents) was added. The resulting solution was stirred at 60 °C for 23 h. The solvent was removed under reduced pressure, and the crude product was dissolved in $CHCl_3$. The solution was washed with a 10% (m/v) NH_4Cl aqueous solution and deionized water. The organic phase was separated and dried over anhydrous Na_2SO_4. Recrystallization from CH_2Cl_2/MeOH was then performed. After filtration,

the blue-green solid obtained was further purified by silica gel column chromatography using gradient elution, from CH_2Cl_2:*n*-hexane (6:4, v/v) to CH_2Cl_2:*n*-hexane (8:2, v/v).

Sixth band, R_f= 0.23. Yield=15%. ^{1}H NMR (400 MHz, $CDCl_3$): δ 1.36 (t, J=7.6, 3H, C*H*$_3$), 1.41 (t, J=7.6, 3H, C*H*$_3$), 1.45÷1.62 (m, 15H, C*H*$_3$.), 3.58 (q, 2H, SC*H*$_2$), 3.85÷4.20 (m, 12H, SC*H*$_2$), 4.08 (s, 3H, OC*H*$_3$), 8.01 (br s, 1H), 8.86 (br s, H). UV-vis (CH_2Cl_2): λ_{max}/nm: 336 (Soret); 500 (extra band), 662 (Q band). MALDI-MS: *m/z* 981.14 $[M+3H]^+$(calcd. for $C_{36}H_{43}N_8PdO_2S_8$ 981.03), *m/z* 924.08 $[M - COOCH_3 + 5H]^+$ (calcd. for $C_{34}H_{42}N_8PdS_8$ 924.03).

PzPy: ***2-(1-Pyrene)-3, 7, 8, 12, 13, 17, 18-heptakis(ethylthio)-5, 10, 15, 20- porphyrazine***

Brominated porphyrazine **5** (100 mg, 0.123 mmol) was dissolved in a dry DMF/toluene (2:3, v/v) mixture (20 mL) heating at 100°C under N_2. Then, potassium carbonate (136 mg, 0.984 mmol), tetrakis(triphenylphosphine) palladium(0) (10% mol, 14 mg, 0.0123 mmol) and 1-pyrene boronic acid (121 mg, 0.492 mmol) were added in sequence and the mixture heated at reflux. The reaction was monitored by TLC and stopped after 8 h. After cooling to room temperature water (30 mL) was added and the solution was extracted with $CHCl_3$ (35 mL). The organic fractions were collected, dried over anhydrous Na_2SO_4 and filtered. After removal of the solvent under reduced pressure, the crude product was purified first by column chromatography on silica gel (hexane:CH_2Cl_2 6:4 v/v, R_f=0.19), recovering 52 mg of **PzPy** as a dark blue solid (45% yield). ^{1}H-NMR (600 MHz, CDCl3) δ/ppm: -1.10(s,2H); 0.52(t,3H); 1.25(t,3H); 1.44(t,3H); 1.55(t,3H); 1.58(t,6H); 1.66(t,3H); 3.06(m,1H, J=12.5, 7.4 Hz); 3.20(dq,1H, J=12.5, 7.4Hz); 3.29(dq,1H, J=12.5, 7.4Hz); 3.33(dq,1H, J=12.5, 7.4Hz); 3.91(dq, 2H, J=7.4, 1.7 Hz); 4.13(m, 6H); 4.29(dq, 2H, J=7.4, 2.6); 7.96(d, 1H, J=9.0 Hz); 8.08(t, 1H, J=7.5 Hz); 8.09(d, 1H, J=9.0 Hz); 8.19(d, 1H, J=7.5 Hz); 8.28(d, 1H, J=9.0 Hz); 8.31(d, 1H, J=9.0 Hz); 8.32(d, 1H, J=7.5 Hz); 8.52(d, 1H, J=7.5 Hz); 8.62(d, 1H, J=7.5 Hz). UV-Vis, CH_2Cl_2, λ_{max}/nm: 277, 350 (Soret), 513 (extra band), 640 and 709 (Q bands).

2-Trimethylsilyl-ethynyl-[6]helicene (11)

2-Bromo-[6]helicene (82 mg, 201 μmol) was dissolved, under an inert atmosphere, in freshly distilled Et3N (17 mL). Trimethylsilylacetylene (42 μL, 301 μmol) was then dropwise added, followed by CuI (4.2 mg, 22.0 μmol) and $PdCl_2(PPh_3)_2$ (28.2 mg, 40 μmol). The mixture was heated at reflux under vigorous stirring, observing a darkening. After 3 hours, reflux was stopped and the mixture was allowed to cool at room temperature. The mixture was diluted with CH_2Cl_2 and filtered on Celite.

The orange solution was extracted with saturated NH_4Cl. The collected organic phases were washed with brine and dried over anhydrous Na_2SO_4. After filtration and solvent evaporation at reduced pressure the recovered orange-yellow solid was first purified by column chromatography (silica gel, hexane:CH_2Cl_2, 9 : 1 v/v) and later by using a preparative TLC plate (1.0 mm thickness, silica gel, hexane:CH_2Cl_2, 9 : 1 v/v). Compound **11** was obtained as a clear yellow solid (22.0 mg, 122 μmol) in 27% yield. ^{1}H-NMR (400 MHz, CDCl3) δ/ppm: 0.18 (s, 9H); 6.72 (ddd, 1H, J1 = J2 = 7.2 Hz, J3 = 1.0 Hz); 7.25 (dd, 1H, J1 = 6.8 Hz, J2 = 1.2 Hz); 7.30 (dd, 1H, J1 = J2 = 6.8 Hz); 7.56 (d, 1H, J = 8.8 Hz); 7.73 (d, 1H, J = 8.4 Hz); 7.77 (s, 1H); 7.84 (d, 1H, J = 9.2 Hz); 7.87 (d, 1H, J = 9.2 Hz); 7.90–8.06 (m, 7H). GC-MS (EI) *m/z* 424.2 $[M]^+$ (calcd. for $C_{31}H_{24}Si$ 424.2).

2-Ethynyl-[6]helicene

Compound **11** (20.0 mg, 47 μmol) was dissolved in THF (0.5 mL), and then TBAF (50μL, 47 μmol) was added. The solution instantaneously became bright orange from clear yellow and was left stirring at room temperature for 20 min. Then 0.5mL of HCl 10% v:v was added to quench the reaction and diluted with CH_2Cl_2 and the organic phase was washed with $NaHCO_3$ and water. The collected organic phases were dried over anhydrous Na_2SO_4 and filtered. After filtration, the solvent was removed under vacuum, recovering compound **12** (16 mg, 46 μmol) as a yellow-orange solid (quantitative yield). ^{1}H NMR (400 MHz, $CDCl_3$), δ/ppm: 2.69 (s, 1H, CuCH), 6.70 (dd, 1H, J1 = J2 = 8.4 Hz), 7.26 (d, 1H, J = 11.6 Hz), 7.27 (dd, 1H, J1 = J2 = 6.8 Hz), 7.54 (d, 1H, J = 8.4 Hz), 7.74 (d, 1H, J = 8.8 Hz), 7.75 (s, 1H), 7.85 (d, 1H, J = 8.0 Hz), 7.86 (d, 1H, J = 7.6 Hz), 7.89–8.30 (m, 7H). GC-MS (EI) *m/z* 352.1 $[M]^+$ (calcd. for $C_{28}H_{16}$ 352.1).

[2-Bromo-3,7,8,12,13,17,18-heptakis(ethylthio)-5,10,15,20-porphyrazinate] palladium(II) (9)

Compound **5** (130 mg, 0.16 mmol) was dissolved in anhydrous toluene (20 mL) and $Pd(OAc)_2$ (46 mg, 0.20 mmol) was added. The solution was stirred at 140 °C for 1 h under a nitrogen atmosphere. After vacuum removal of the solvent, the dark solid was purified by silica gel column chromatography with CH_2Cl_2/hexane (1 : 1 v/v) as the eluent. Second band, R_f= 0.54, yield 24%. ^{1}H-NMR (400 MHz, $CDCl_3$) δ/ppm: 1.42 (t, 3H J = 7.5); 1.47–1.62 (m, 18H); 3.80 (q, 2H J = 7.5); 3.89 (q, 2H J = 7.5); 3.97 (q, 2H J = 7.5); 4.02 (q, 4H J = 7.5); 4.06 (q, 2H J = 7.5); 4.14 (q, 4H J = 7.5). ^{13}C-NMR (100 MHz, CDCl3) δ/ppm: 15.46, 15.49, 15.56, 15.58, 28.84, 29.03, 29.36, 29.40, 29.41, 29.53, 29.55, 121.00, 135.85, 139.51, 139.62, 139.80, 140.16, 140.44, 140.64, 141.90, 142.51, 143.55, 143.85, 144.90, 145.00, 145.27, 145.46.

PdPzHelix:[*2-(2-Ethynyl-[6]-helicene)-3,7,8,12,13,17,18-eptakis(ethylthio)-5,10,15,20]-porphyrazinate palladium(II)*

The palladium(II) complex **9** (30.0 mg, 59.0 μmol) was dissolved in Et_3N (15 mL). The dark blue solution was heated at reflux, and then compound **12** (30 mg, 88 μmol), CuI (1.0 mg, 5.2 μmol), and $PdCl_2(PPh_3)_2$ (8.5 mg, 9.2 μmol) were added in sequence. After 180 min heating was removed, the mixture was allowed to cool at room temperature, and the solvent was removed under vacuum. The dark blue solid recovered was dissolved in CH_2Cl_2 and washed in sequence with saturated NH_4Cl and brine. The collected aqueous phases were washed with CH_2Cl_2. The collected organic phases were then dried over anhydrous Na_2SO_4 and filtered. The solvent was removed under vacuum, recovering a dark blue solid which was first purified by silica gel column chromatography using a gradient elution (hexane:CH_2Cl_2, first 7 : 3, then 6 : 4, finally 1 : 1 v/v) and subsequently by using a preparative TLC plate (1.0 mm thickness, silica gel, hexane:CH_2Cl_2, 1 : 1 v/v, R_f= 0.32). The product **PdPzHelix** was recovered as a dark blue solid TLC plate (SiO_2; 1.0 mm thickness, silica gel, hexane:CH_2Cl_2, 1 : 1 v/v, R_f = 0.34). ^{1}H NMR (400 MHz, $CDCl_3$) δ/ppm: 1.31 (t, 3H, CH_3, J = 7.5 Hz), 1.41–1.64 (m, 18H, CH_3), 3.62–3.74 (m, 1H, SCH_2), 3.74–3.85 (m, 1H, SCH_2), 3.96 (q, 2H, J1 = 7.2 Hz, SCH_2), 4.01 (q, 2H, J1 = 7.2 Hz, SCH_2), 4.4–4.2 (m, 6 H, SCH_2), 4.22 (q, 2H, J1 = 7.2 Hz, SCH_2), 6.77 (br t, 1H, J = 6.8 Hz), 7.23 (br t, 1H, J = 6.8 Hz), 7.63 (d, 1H, J1 = 8.4 Hz), 7.73 (d, 2H, J = 8.4 Hz), 7.87 (d, 1H, J = 8.2 Hz), 7.90–8.00 (m, 3H), 8.00–8.14 (m, 6H). UV-Vis, CH_2Cl_2, λ_{max}/nm: 265, 274, 334 (Soret), 514 (extra band), 663 (Q band).

2.5 References

1. Fernàndz-Ariza, J.; Urbani, M.; Rodrìguez-Morgade, M. S.; Torres, T.; *Chem. Eur. J.,* **2018**, *24*, 2618-2625
2. Belviso, S.; Santoro, E.; Penconi, M.; Righetto, S.; Tessore, F.; *J. Phys. Chem. C,* **2019**, *123*, 13074-13082
3. (a) Liang, Y.; Xu, Z.; Xia, J.; Tsai, S.-T.; Wu, Y.; Li, G.; Ray, C.; Yu, L. *Adv. Energy Mater.* **2010**, 22, E135–E138. (b) Jun Yuan, Y.; Zhang, Y.; Zhou, L.; Zhang, G.; Yip, H.-L.; Lau, T.-K.; Lu, X.; Zhu, C.; Peng, H.;Johnson, P. A.; Leclerc, M.; Cao, Y.; Ulanski, J.; Li, Y.; Zou, Y. *Joule* **2019**, *3*, 1140–1151. (c) Liu, Q.; Jiang, Y.; Jin, K.; Qin, J.; Xu, J.; Li, W.; Xiong, J.; Liu, J.; Xiao, Z.; Sun, K.; Yang, S.; Zhang, X.; Ding, L. *Sci. Bull.* **2020**, *65*, 272–275.
4. Schram, C.; Hoffmann, B. M.; *Inorg. Chem.,* **1980**, 19, 383-385
5. Miyaura, N.; Suzuki, A.; *Chem. Rev*., **1995**, 95, 2457-2483.
6. Liebeskind, S. L.; Srogl, J.; *Org. Lett*., **2002,** 4, 6, 979-981.
7. Medina, D. P.; Fernandez-Ariza, J.; Urbani, M.; Sauvage, F.; Torres, T.; Rodriguez-Morgade, M. S. *Molecules*, **2021**, 26, 2129.
8. Belviso, S.; Capasso, A.; Santoro, E.; Najafi, L.; Lelj, F.; Superchi, S.; Casarini, D.; Villani, C.; Spirito, D.; Bellani, S.; Del Rio-Castillo, A. E.; Bonaccorso, F. *Adv. Funct. Mater*, **2018**, *28,*1705418.
9. Belviso, S.; Marsico, G.; Franzini, R.; Villani, C.; Abbate, S.; Longhi, G., *Dalton Trans.*, **2022**, *51*, 16453–16464
10. (a) Lelj, F.; Morelli, G.; Ricciardi, G.; Roviello, A.; Sirigu, A. *Liq. Cryst*. **1992**, *12*, 941-960. (b) Belviso, S.; Ricciardi, G.; Lelj, F *J. Mater. Chem.* **2000**, *10,* 297–304. (c) Belviso, S.; Cammarota, F.; Rossano, R.; Lelj, F. *J. Porphyrins Phthalocyanines* **2016**, *20*, 223-233
11. Belviso, S.; Ricciardi, G.; Lelj, F.; Monsù Scolaro, L.; Bencini, A.; Carbonera, C. *J. Chem. Soc., Dalton Trans.* **2001**, 1143-1150
12. Belviso, S.; Amati, M.; Rossano, R.; Crispini, A.; Lelj, F. *Dalton Trans*. **2015**, *44*, 2191-2207.

Chapter 3

Peripherally metalated β-η^1-Pd(II)-thioethyl porphyrazine: synthesis, characterization and photovoltaic application[1]

3.1 Synthesis and characterization

3.1.1 Synthesis

In Chapter 2 several aryl- and arylethynyl-substituted thioalkyl porphyrazines have been described. These compounds were synthesized *via* Pd(0)-catalyzed Suzuki-Miyaura[2] or Sonogashira[3] cross-coupling reactions starting from mono-brominated thioalkyl porphyrazines. However, in the Suzuki-Miyaura reaction between the β-bromo thioethyl porphyrazine **5** and aryl boronic acids good yields of the aryl-substituted porphyrazine product were often obtained together with a minor secondary product identified, by ^{1}HNMR and ^{13}CNMR analyses, as the β-η^1-Pd(II)-thioethyl porphyrazine complex **13** (Scheme 3.1.1), *i.e.* the oxidative addition intermediate between the parent β-bromo porphyrazine and the $Pd(PPh_3)_4$ catalyst. The quantity of this organometallic compound depended on the reaction time and on the solvents employed: in fact, by using the DMF/Toluene mixture yield of less than 1% was obtained, while from the reaction in THF a 5% yield was recovered.

Some *meso* ring-metalated porphyrins have been reported in the past,[4] while only a single example of β cyclometalated porphyrin dimers has been described.[5] Therefore, complex **13** represents the first example of isolable β-ring-metalated tetrapyrrole with a C_β-M bond. We then decided to undertake a more in-depth structural and electronic study on this compound, to eventually employ it in the fabrication of optoelectronic devices. Accordingly, the direct synthesis of complex **13**, its structural characterization, a detailed investigation of its spectral and electrochemical properties by both experimental and computational methods, were carried out.

At first, it was necessary to establish a suitable synthetic strategy for the direct preparation of complex **13**. An optimized preparation of the complex in good 80% yield was accomplished by reacting the brominated porphyrazine **5** (described in 2.1) with an equimolar quantity of $Pd(PPh_3)_4$ in refluxing toluene (Scheme 3.1.1).

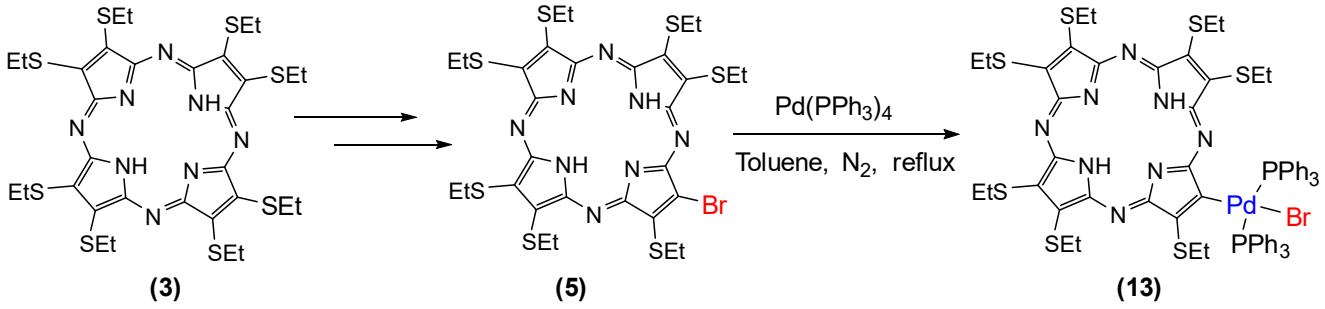

Scheme 3.1.1 *Direct synthesis of organometallic β-η[1]-Pd(II)-thioethyl porphyrazine complex* ***(13)****.*

3.1.2 NMR characterization

The ^{1}HNMR ($CDCl_3$) spectrum of **13** (Figure 3.1.1) shows the typical signals of a *free base* asymmetric thioethyl porphyrazine. In fact, at -1.85 ppm is observed a singlet (*a*) relative to the internal protons of the macrocycle, between 1.0 and 2.0 ppm the cluster relative of the methyl groups of the thioethyl chains (*b*), between 3.5 and 4.5 ppm the cluster (*c*) relative to the protons of the -SCH_2 groups of the chains. Finally, three intense signals *(d)* are observed in the aromatic zone which could be attributed to the *para*, *meta*, and *ortho* protons of the six phenyl groups of the two triphenylphosphine moieties.

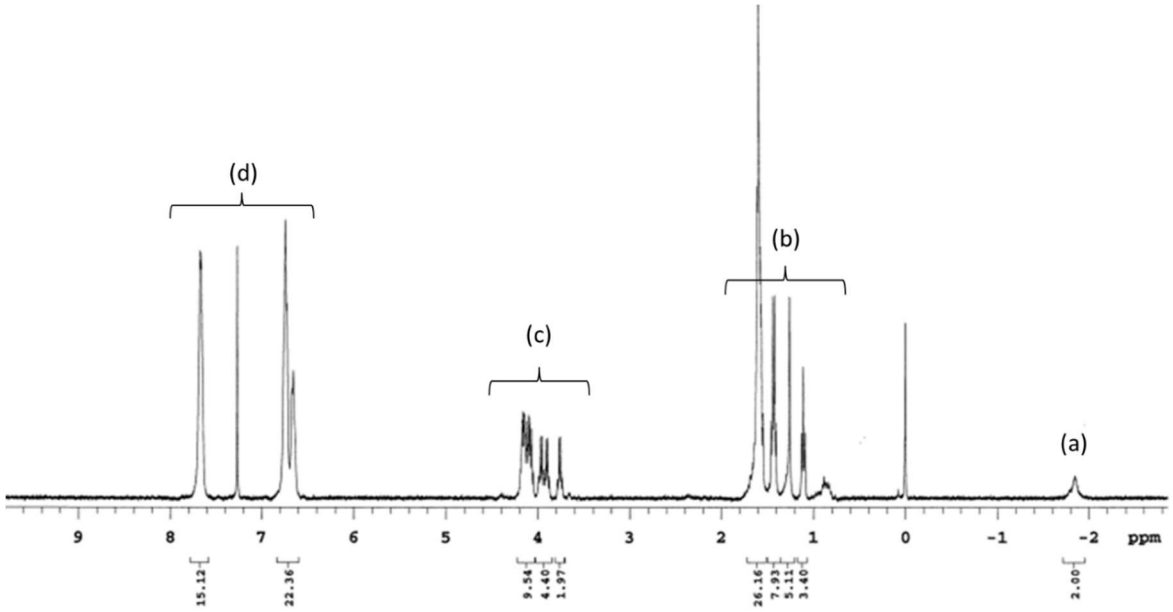

Figure 3.1.1 *^{1}H NMR spectrum of complex* ***13****.*

The ^{13}CNMR ($CDCl_3$) spectrum confirms the presence of the triphenylphosphine moieties together with the thioethyl substituted porphyrazine system (Figure 3.1.2). In fact, in the spectrum there are two signals attributable to aliphatic carbons, respectively, around 15 and 30 ppm, while in the aromatic zone, four intense signals can be observed between 120 and 135 ppm, followed at lower

field, by numerous signals of the quaternary carbons of the macrocycle. The detail of the signals between 120 and 135 ppm (Figure 3.1.3) shows two flared singlets at 127.3 (*c*) and 129.6 ppm (*d*), followed by two triplets at 130.4 (*a*) and 134.5 ppm (*b*). These triplets can be attributed to the *ipso* and *ortho* carbons of the phenyls of triphenylphosphine. Their multiplicity indicates the presence of a coupling with two ^{31}P nuclei, the one adjacent to the phenyl and, through a "virtual coupling", the one belonging to another triphenylphosphine moiety, constituting an ABX spin system. On the basis of what is reported in the literature for the phosphine complexes of Pd and Pt[6,7], this spectral pattern can be attributed to the presence of two PPh_3 groups coordinated in the *trans* position to a Pd atom in turn linked to the macrocycle. Another confirmation of the presence of phosphorous atoms in **13** is obtained from the ^{31}P-NMR spectrum (Figure 3.1.4), in which a singlet at 24 ppm is present.

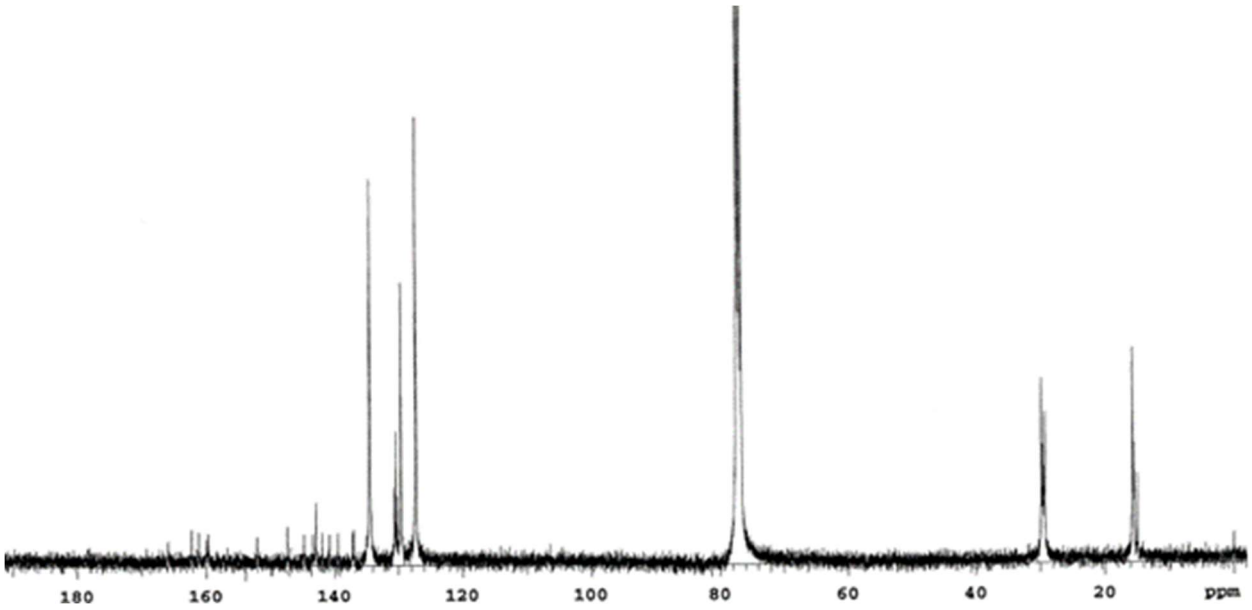

Figure 3.1.2 *^{13}C NMR spectrum ($CDCl_3$) of complex* **13.**

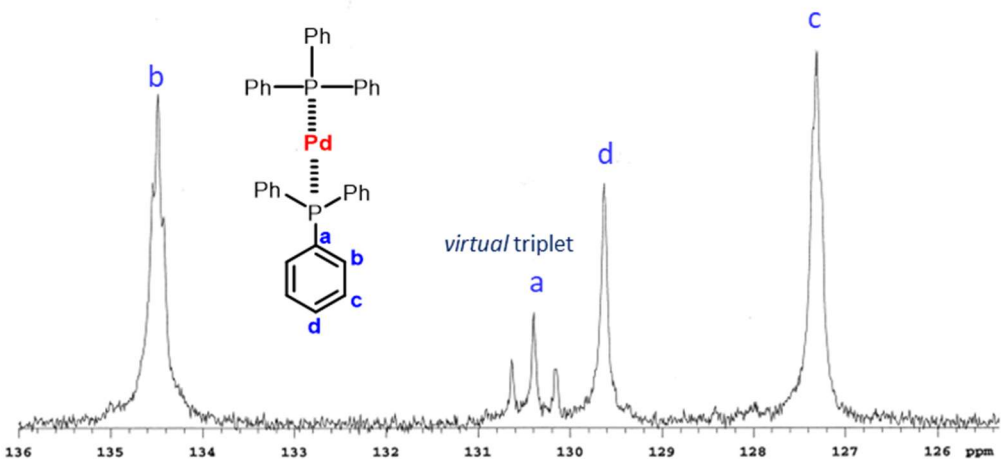

Figure 3.1.3 *^{13}CNMR spectrum ($CDCl_3$) of complex* ***13****. Enlargement of the 126-136 ppm range.*

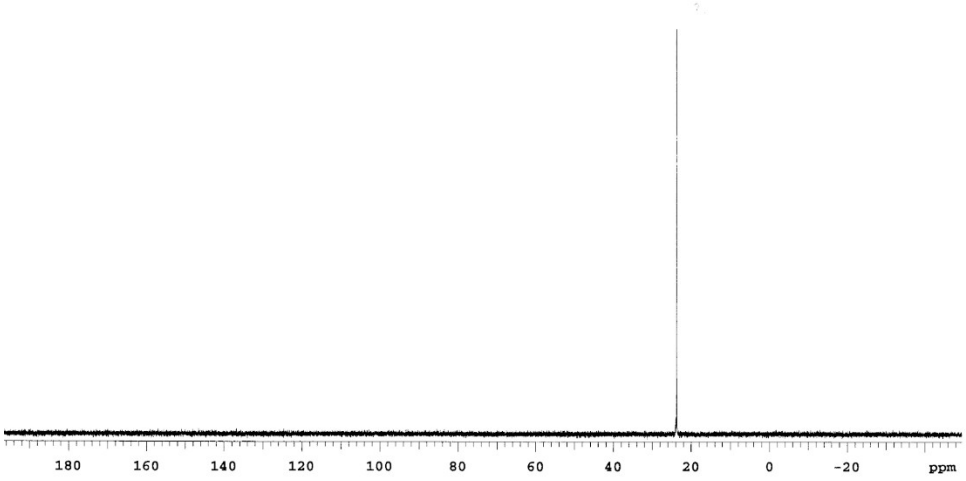

Figure 3.1.4 *^{31}P-NMR spectrum of compound **13**.*

3.1.3 Crystallographic characterization

Complex **13** was particularly stable in air and in solution allowing its crystallization from a CH_2Cl_2/MeOH mixture. Single crystals were obtained by slow diffusion of methanol in a CH_2Cl_2 solution followed by a very slow evaporation of solvent at ambient temperature. Complex **13** crystallizes in the triclinic P-1 space group with one molecule of the complex and one dichloromethane solvent molecule contained in the asymmetric unit. Bond lengths and bond angles are in the normal range and in agreement with similar compounds.[8]

The molecular structure of the compound confirms that the halogenated -$PdBr(PPh_3)_2$ group is in the β-position of a pyrrole ring and that a partial exchange of Br atom with Cl atom took place during crystallization generating two molecular structures different only for the halogen nature. In fact, as reported in literature,[8c] during the slow crystallization process, the presence of chlorinated solvents can induce a partial exchange of the halogen. The structural analysis showed that the halogen exchange was almost complete and that only a very small fraction of the brominated to the chlorinated compound was formed (fraction -Cl to -Br is 0.98 to 0.02). The complex shows the usual square planar geometry around the Pd atom, with the square plane approximately perpendicular to the porphyrazine, ring system. The C-Pd-halogen axis is in the plane of pyrrole ring and the two -PPh_3 groups are arranged in approximately mirror symmetry with phenyl rings overlapping the pyrrole ring on both sides. The pyrrolic hydrogen atoms inside the porphyrazine ring system show a *trans* disposition of the NH groups that are involved in the usual intramolecular N-H--N hydrogen bonding pattern observed in similar compounds. The macrocycle ring system is essentially planar and assumes a slight-bent flat shape with the peripheral thioethyl groups alternatively oriented up- and in- plane with a preferential disposition that results less sterically hindered in one side. The crystal packing is

stabilized by normal van der Waals interactions and face-to-edge interactions of phenyl rings. The crystallographic structure confirms the spectroscopic data obtained: the intermediate formed is an organometallic complex, the metal atom is linked to the β position of the macrocycle and the two -PPh_3 groups linked to the metal atom are positioned in *trans*, also the presence of the of bromine has been confirmed, furthermore it is visible that the geometry of the complex formed by Pd(II) is, as expected, of the square planar type. This structure represents one of the very few cases of crystallographic resolution obtained so far for a thioalkyl porphyrazine.

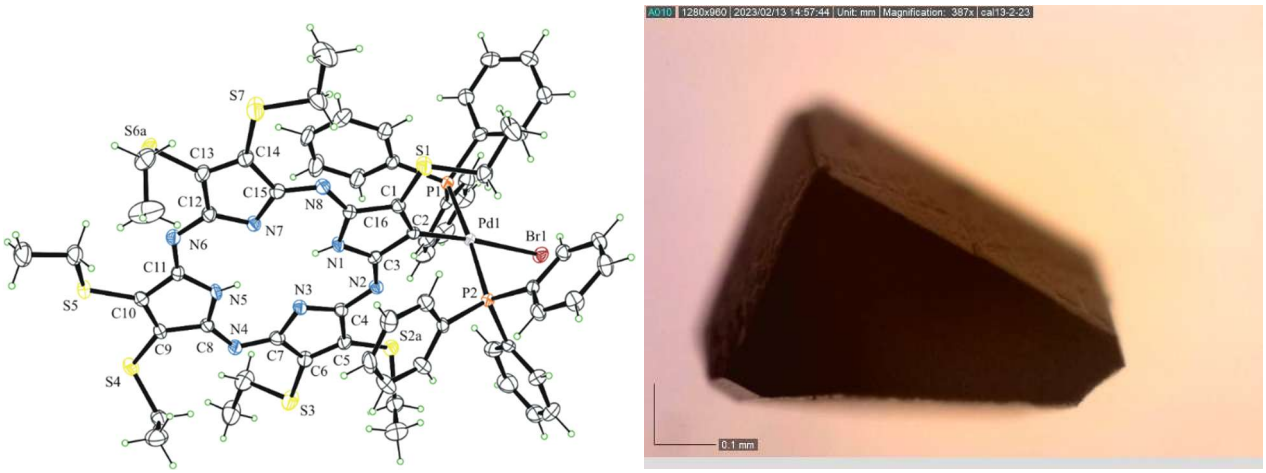

Figure 3.1.5 (left) *Ortep view of complex 1 with ellipsoids drawn at 50% probability level. The dichloromethane solvent molecule and the minor parts of the disordered thioethyl groups are not drawn for clarity.* ***(right)*** *single crystal image of complex* ***13*** *in the not polarized light of optical microscope.*

3.1.4 Spectroscopic analysis

Detailed studies of the spectral and electrochemical properties of complex **13** have also been carried out. Its UV-Vis absorption spectrum in CH_2Cl_2 is reported in Figure 3.1.6, together with that of the symmetrically substituted thioethyl porphyrazine **3** (Chapter 2.1). The spectrum of **13** shows several intense absorption bands in the 250-800 nm range featuring the typical characteristics of non-aggregated *free base* thioalkyl porphyrazines and closely resembling that of **3**, but with distinctive differences in the wavelengths of the two Q bands. Specifically, the main spectral features of **13** are the two Q bands at 693 nm and 650 nm, the "extra" band at 515 nm (due to the $n_{sulfur} \rightarrow \pi^*$ transitions), and the Soret band at 363 nm. Moreover, a new band at 307 nm, attributable to the triphenylphosphine chromophore, is present. Comparison of the experimental spectra of both species (Figure 3.1.6), highlights differences arising from the modification of the macrocycle periphery. The most notable differences include a blue-shift (~17 nm) of the lower energy Q_x band of **13** and a red-shift (~13 nm)

of the higher energy Q_y band. Additionally, red shifts of both the "extra" band (~15 nm) and Soret band (~4 nm) are observed.

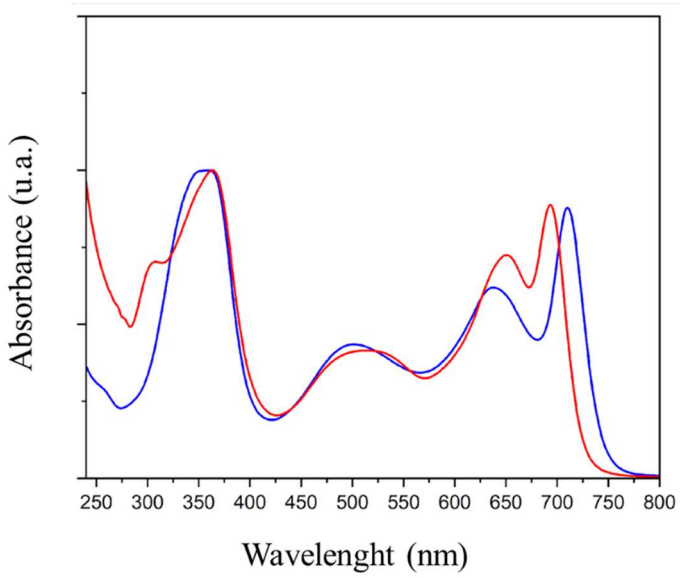

Figure 3.1.6 *UV-Vis absorbance spectrum of compound **3** (blue line) and complex **13** (red line).*

To gain further insight into the electronic structure of complex **13**, a time-dependent density functional theory (TDDFT) computational investigation was performed to interpret the UV–Vis spectral features by comparing the main transitions with those of the parent unsubstituted porphyrazine **3**. Accordingly, quantomechanical calculations at TDDFT/wB97X-D3/def2-TZVP/CPCM(CH_2Cl_2) level of theory were carried out on both **3** and **13**. The UV-Vis transitions of **3** have been previously described and assigned with the computational support[9], but for consistency in spectral comparison, these calculations were repeated at the same level of theory used for complex **13**. Overall, the interpretation of the main electron transitions in **3** confirmed earlier reports, with an improved match to the experimental data (Figure 3.1.7). The two Q_x and Q_y bands at 673 and 648 nm correspond to the HOMO→LUMO and HOMO→LUMO+1 MOs transitions, respectively (see Figure 3.1.8 right side). The "extra" band can be ascribed to two main transitions #6 and #9: the first involves the HOMO-1→LUMO transition, with charge transfer (CT) character localized on sulphur electrons, while the second results from combined HOMO-3→LUMO+1 and HOMO-2→LUMO+1 CT transitions covering different sulphur localized orbitals. The Soret band is described by π-π* transitions #17÷19 originating from the combination of HOMO-6/-7/-8→ LUMO/LUMO+1 and #27 by HOMO-13/HOMO-12→LUMO+1. This new set of calculations aligns well with experimental

data, closely matching relative intensities and positions of the Q_x and Q_y bands, the origin of the characteristic "extra" band of the thioalkyl porphyrazines, and the relative intensity of the Soret band.

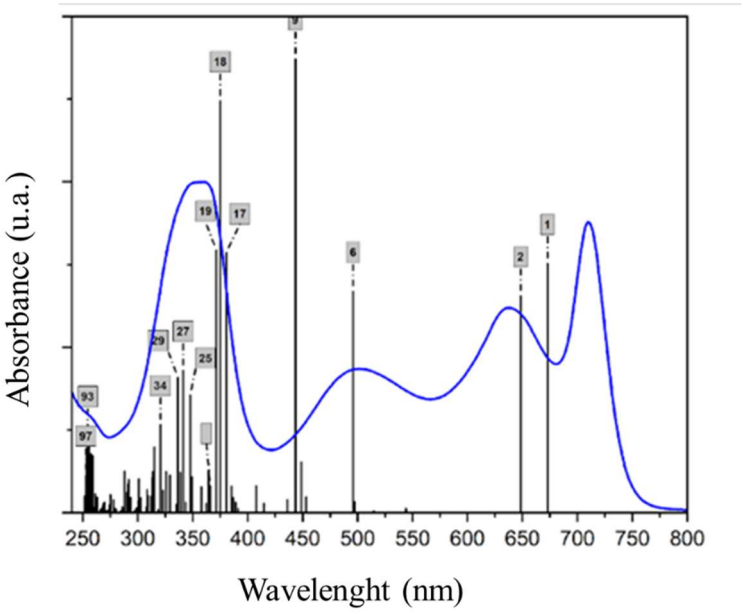

Figure 3.1.7 *Experimental UV-Vis spectrum (blue line) and computed dipolar strengths (black bars) at TDDFT/wB97X-D3/def2-TZVP/CPCM (CH_2Cl_2) level of theory for* ***3****.*

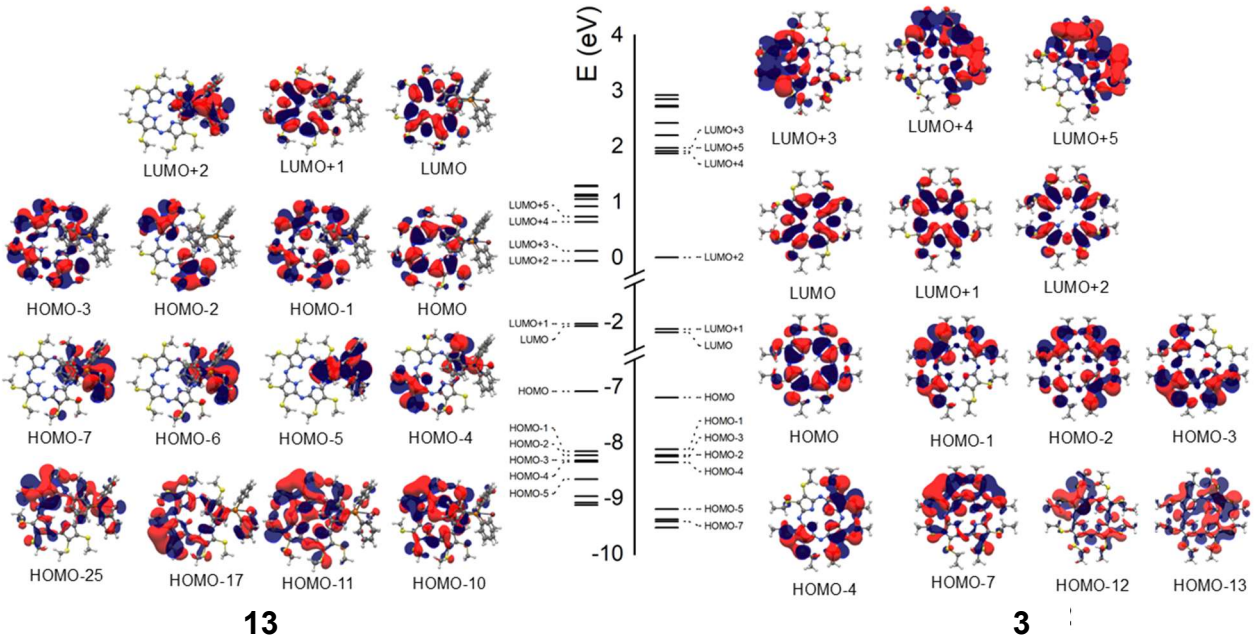

Figure 3.1.8 *Kohn-Sham orbital energy levels and graphical representations of some more relevant orbitals computed at TDDFT/wB97X-D3/def2-TZVP/CPCM (CH_2Cl_2) level of theory for* ***3*** *(right side) and complex* ***13*** *(left side).*

For complex **13**, the computed dipolar strengths superposed on the experimental UV-Vis spectrum (Figure 3.1.9) well reproduce the observed main spectral features in terms of position and relative intensity. Both Q_x and Q_y bands derive from a combination of the HOMO→LUMO and HOMO→LUMO+1 transitions (transitions #1 and #2) localized on the macrocycle core (Figure 3.1.8 left side). In respect to **3**, a different mixing probability of the MOs character, due to a smaller energy gap between nearly degenerate LUMO and LUMO+1, and a smaller $\Delta E_{HOMO-LUMO}$ bandgap (5.0078 eV (**13**) *vs* 5.0127 eV (**3**)), are observed. The calculations reproduce the convergence of the two Q bands, resulting from a blue shift of the Q_x band and a red shift of the Q_y band. In the 420-550 nm range, a higher number of transitions (# 5-9, Figure 3.1.8 left side), occur from HOMO-1 to HOMO-4 MOs localized on peripheral sulphur atoms to the macrocycle core LUMO+1, reflecting the reduced molecular symmetry. Notably, the transitions contributing to the Soret band (transitions #20, 21, and 23) have different origins and characteristics: transition #23 (HOMO-10→ LUMO+1) is fully localized on the macrocycle, whereas both transitions #20 (HOMO-5→LUMO) and #21 (HOMO-5→LUMO/LUMO+1) involve CT from the HOMO-5 MO localized on the $Pd(PPh_3)_2$ substituent to the LUMO/LUMO+1 localized on the macrocycle core (Figure 3.1.8 left side). It is worth noting that in peripherally aryl-substituted thioalkyl porphyrazines[10,11,12,13] HOMO-LUMO CT transitions occur between the aryl substituent and the macrocycle core, whereas in complex **13** the CT transition occurs at higher energy, in correspondence to the Soret band. Finally, the additional feature at 307 nm corresponds to transition #50 (HOMO-7→LUMO+2) attributable to a π−π* transition localized on the triphenylphosphine groups.

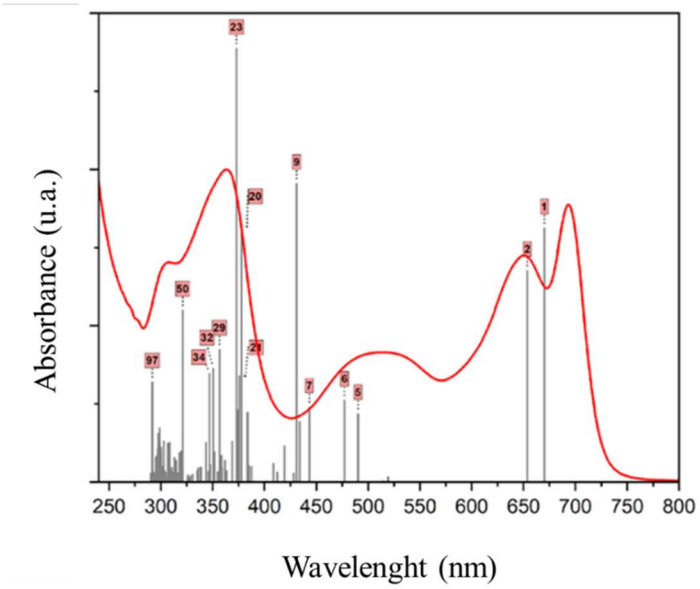

Figure 3.1.9 *Experimental UV-Vis spectrum (red line) and computed vertical energies (grey bars) at TDDFT/wB97X-D3/def2-TZVP/CPCM (CH_2Cl_2) level of theory for **13**.*

3.1.5 Electrochemical properties

The electrochemical behaviour of the novel Pd(II) porphyrazine complex **13** was investigated. The analysis was carried out using cyclic voltammetry (CV) and differential pulsed voltammetry (DPV) with all potentials (Table 1) reported versus the ferrocene/ferrocenium redox couple used as internal standard. The redox profile of complex **13** is typical of thioalkyl porphyrazines. As it can be seen from the cyclic voltammogram shown in Figure 3.1.10, the cathodic curve is characterized by two reversible monoelectronic reduction process of the porphyrazine ring attributed to formation of the porphyrazine π-anion radical and dianion, respectively.[14,15] The half-wave potentials in CH_2Cl_2 for these two processes are respectively $E_{1/2}(\Delta E_p) = -1.077$ V (0.072) and $E_{1/2}(\Delta E_p) = -1.454$ V (0.073). The ΔE_p values, slightly higher than the theoretical 0.057 V, indicate quasi-reversible processes.

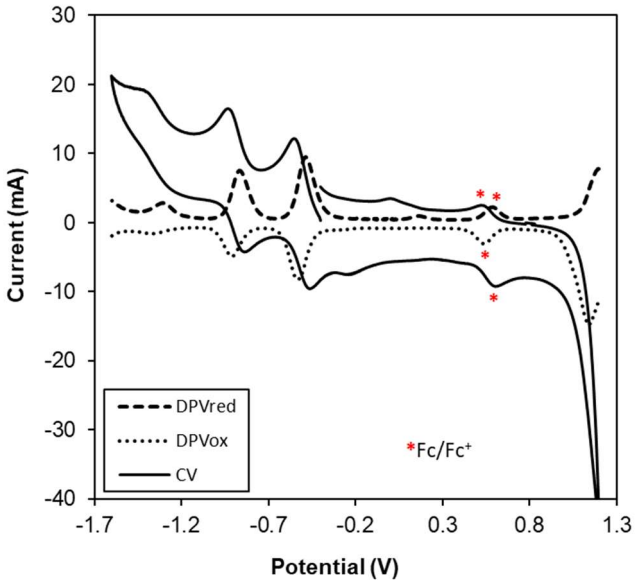

Figure 3.1.10 *Cyclic voltammogram and differential pulse voltammograms of complex* ***13*** *in CH_2Cl_2. Ferrocene/ferrocenium redox signals are labelled with a red asterisk.*

Table 2 *Summary of peak potentials $E_{1/2}$ (volts vs Fc/Fc^+) for complex* ***13*** *and compound* ***3.***

			Oxidation	Reduction		E_{HOMO}[b]		E_{LUMO}[b]		HOMO-LUMO bandgap
Compd	Tech[a]	Solvent		I	II	Expt.	Compt[c]	Expt.	Compt[c]	
	(CV)	CH_2Cl_2	/	-1.077	-1.454		-5.792[d]	-3.723	-3.337[d]	/
	$(DPV)_{red}$	CH_2Cl_2	/	-1.076	-1.458			-3.724		/
13	$(DPV)_{ox}$	CH_2Cl_2	/	-1.068	-1.446			-3.732		/
	(CV)	DMF	/	-0.929	-1.381			-3.871		/
	$(DPV)_{red}$	DMF	0.713	-0.934	-1.409	-5.513	-5.729[e]	-3.866	-3.273[e]	1.647
	$(DPV)_{ox}$	DMF	0.714	-0.911	-1.389	-5.514		-3.889		1.625
3	(CV)	CH_2Cl_2	/	-0.907	-1.230			-3.893		/

[a]Measured in 10^{-3} M solution. Glassy carbon working electrode. [b]Values (eV) referred to first oxidation and first reduction and calculated assuming the energy level for the ferrocene at −4.8 eV. [c]HOMO and LUMO orbital energy calculated by DFT on the optimized neutral molecule. [d]TDDFT/M06/def2-TZVP/CPCM(CH_2Cl_2). [e]TDDFT/M06/def2-TZVP/CPCM(DMF).

The DPV data are consistent with the CV results. The electrochemical analysis in DMF provided reduction potential values very similar to those in CH_2Cl_2 and allowed detection of the oxidation potential not clearly visible in the latter solvent (Table 2). HOMO and LUMO energies calculated from electrochemical data are reported in Table 2, by assuming the energy level of ferrocene/ferrocenium at −4.8 eV.[16,17,18] The HOMO and LUMO energies calculated from the experimental electrochemical data are -5.5 eV for HOMO and -3.9 eV for LUMO, respectively, yielding a bandgap of approximately 1.6 eV. As observed for other asymmetrically substituted thioalkyl porphyrazines, these HOMO and LUMO energy values make **13** potentially suitable for fabrication of BHJ cells with nanocarbons acceptors.[11,13] A significant shift to more cathodic values is observed in the case of complex **13** compared to the potential values of "free base" porphyrazine **3**. Computed values for the HOMO and LUMO energies at TDDFT/M06/def2-TZVP/CPCM level of theory in both CH_2Cl_2 and DMF are also reported in Table 2. They are in good agreement with experimental data, confirming the reliability of the computational protocol.

3.2 Application: nanohybrids with Graphene Nanoflakes

The spectroscopic and electrochemical properties of complex **13** described above make this compound promising for OPV applications. Moreover, the presence of additional of aromatics rings other than the porphyrazine ring on the complex could enhance its interaction with nanocarbon moieties used as acceptors in OPV devices. This behaviour has been previously described in the research group where this PhD thesis was carried out in refence to the pyrene-substituted thioethyl porphyrazine **PzPy**[11] (see paragraph 1.6.2). Therefore, a study on the preparation of nanohybrids with Graphene nanoflakes (GNF) and on their photoresponse has been carried during the required industrial stage at the BeDimensional S.p.A. laboratories in Genova.

Graphene is a material formed by a single layer of sp^2 carbon atoms, bonded by strong σ bonds, arranged like hexagons with 120° angles and 0.142nm bond length. It is the thinnest and hardest material in the world. When it's pure, is totally hydrophobic, insoluble in many solvents and difficult exfoliate.

Its preparation can be made by two majors synthetic techniques:

- **Top-down approach**, when graphene is produced by exfoliation of the graphite in several ways. The most common method, used in this work, is liquid phase exfoliation in organic solvent or aqueous solution in the presence of surfactants. To do this, the solution is sonicated to give enough energy for breaking the π-π interaction between the graphite layers. Generally, in addiction to organic solvents, planar aromatic molecules are used to help the exfoliation.
- **Bottom-up approach**, where graphene is synthetized from a feedstock of carbon using different techniques (e.g. chemical vapour deposition)

3.2.1 Synthesis of Graphene Nanoflakes

Synthesis of graphene nanoflakes was made in BeDimensional S.p.A. laboratory using a Liquid Exfoliation process.[19] This method consists of ultrasonication of graphite bulk material followed by centrifugation. In this way, it was obtained a biphasic dispersion with the smallest flakes remaining in solution and the largest and heavy ones as well as chunks of non-exfoliated graphite that settle to the bottom of the tube. The dispersion was then characterized by Raman spectroscopy, Atomic Force Microscopy (AFM) and Transmission Electron Microscopy (TEM).

Raman spectroscopy

The Raman spectroscopy gives information about the quality of the samples. In fact, by using this fast and non-destructive technique it is possible to obtain information about defects, disorder and possible chemical modifications of the flakes. As shown in Figure 3.2.1 the Raman spectra of graphene nanoflakes (GNF) shows the typical D (≈1345 cm^{-1}), D' (≈1615 cm^{-1}), G (≈1582 cm^{-1}) and

2D (≈2696 cm^{-1}) bands.[20] Where 2D is a degenerate band formed by $2D_1$ and $2D_2$ which can be used as indicators of the thickness of the material. In fact, in graphite the $2D_2$ band is more intense of the $2D_1$ band. If normalized for the intensity of the G band and plotted the $I[2D_1]/I[G]$ *vs* $I[2D_2]/I[G]$ it is possible to obtain a demarcation line where all the points below are graphitic flakes and all the point above the line are few layers graphene or single layer graphene. For this sample the purity in graphene nanoflakes is 96%. The D and D' bands are indicators of edge or in-plane defects.
The statistical analysis made on the raw data is shown in Figure 3.2.2**.**

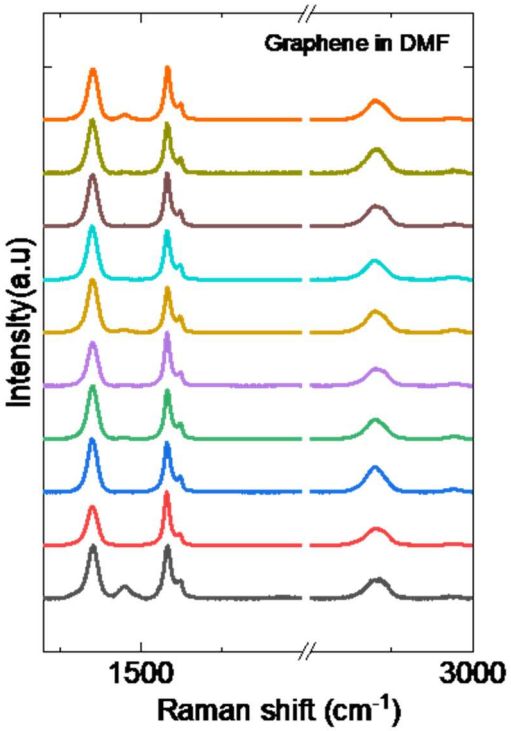

Figure 3.2.1 *Raman spectra of Graphene nanoflakes.*

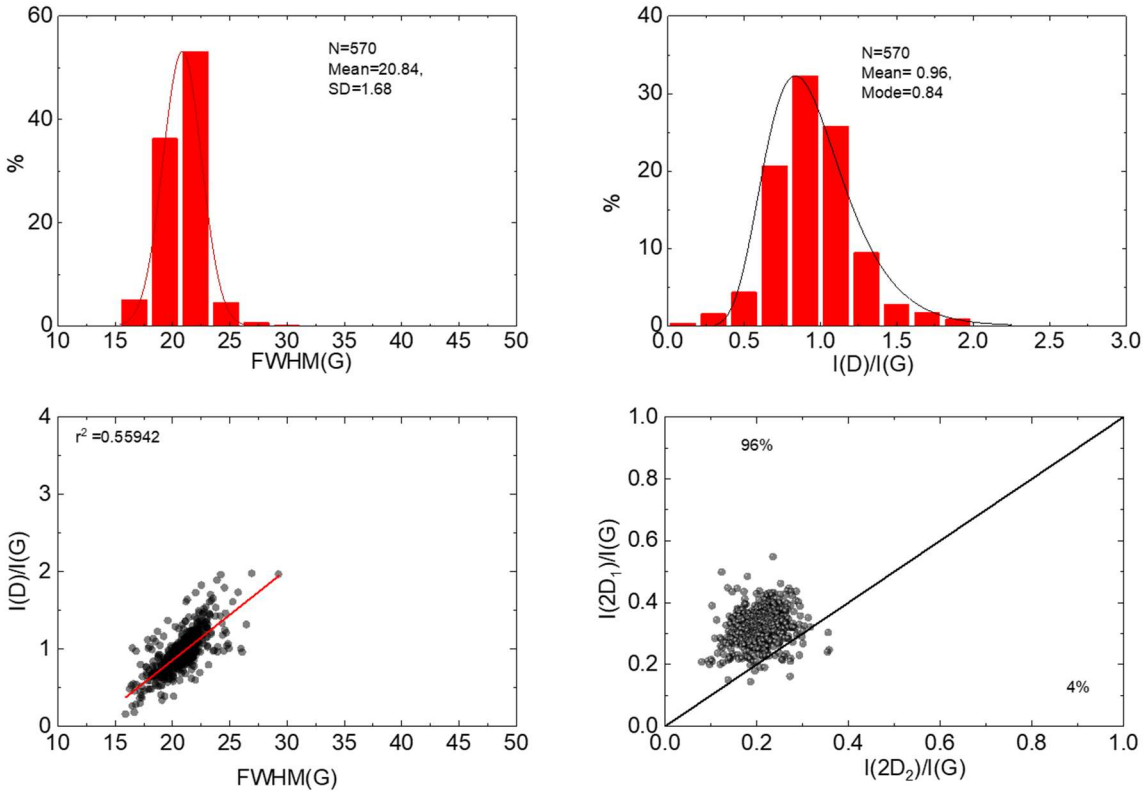

Figure 3.2.2 *Statistical analysis of the Raman raw data collected on graphene sample.*

AFM and TEM analysis

AFM and TEM analysis on graphene sample were performed to evaluate the morphology of the flakes. The two analyses give complementary information about the dimension of the flakes, in fact, by the AFM it is possible to know the sample thickness whereas by TEM it is possible to know its lateral size. The samples were prepared by drop casting from a DMF dispersion on lacey carbon TEM grid while for AFM the sample was drop casted onto a mica sample holder.

From statistical analysis on AFM images (Figure 3.2.3) it is possible to say that the nanoflakes thickness is spread between some nanometres until a maximum of fifty nanometres with a mode of 2.94 nm. This spread is shown also by TEM images. In fact, from the image in Figure 3.2.4 right it is possible to note the differences between the flakes. After statistical analysis it is possible to affirm that the main dimension of graphene nanoflakes is around 138 nm, with a mean of 220 nm.

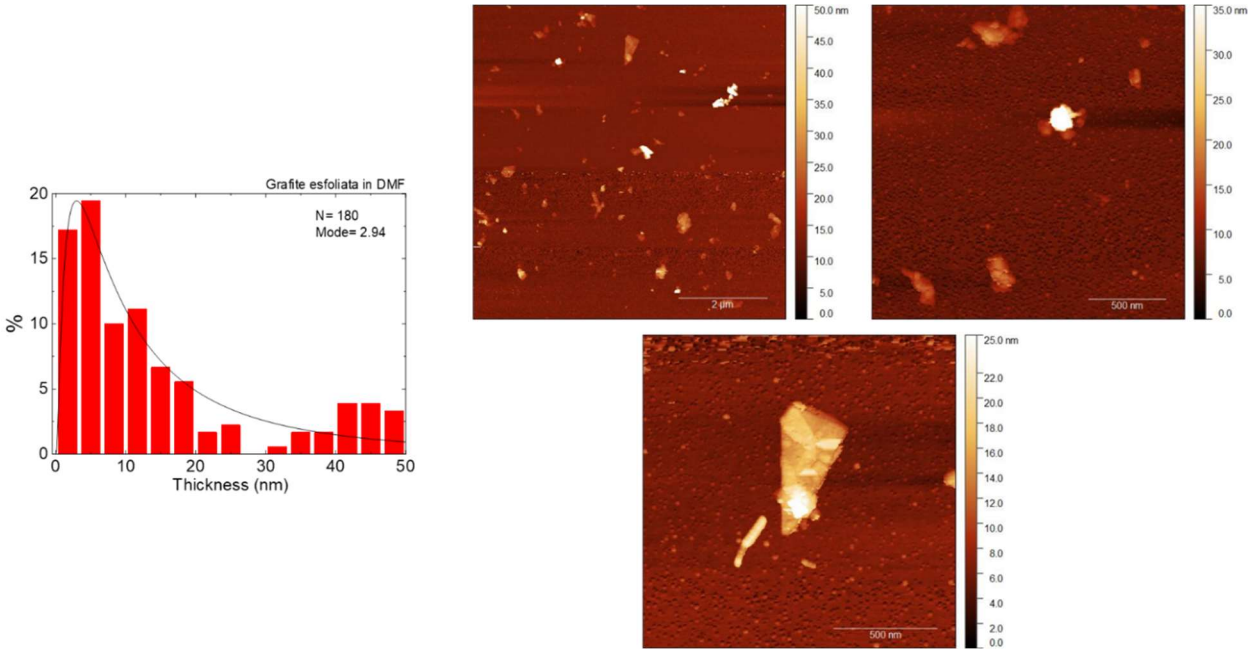

Figure 3.2.3 *atomic force microscopy images (right) and statistical analysis (left) of graphene nanoflakes.*

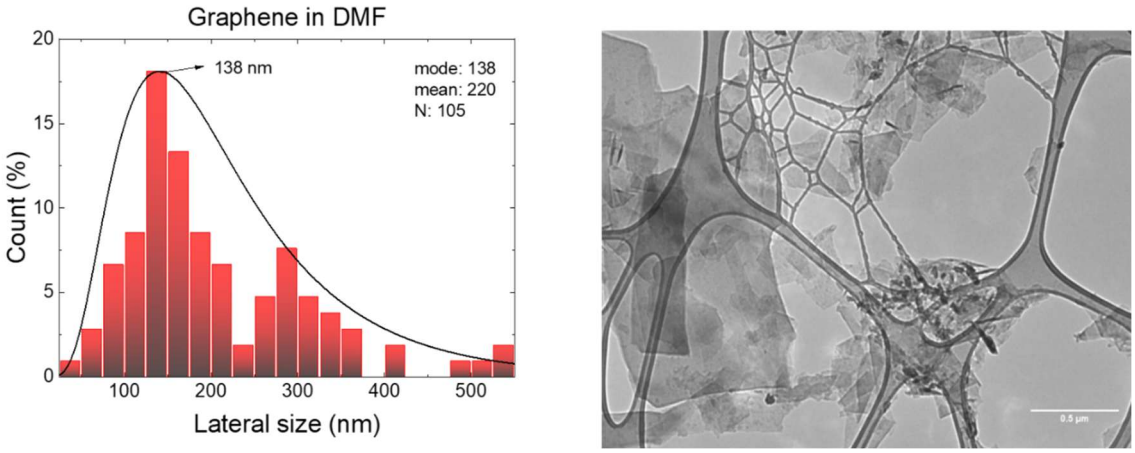

Figure 3.2.4 *Transmission electronic microscopy image (right) and statistical analysis (left) of graphene nanoflakes.*

3.2.2 Nanohybrid preparation and characterization

Between the complex **13** and GNF a π-π interaction occurs, involving the aromatic electrons of the porphyrazine and the aromatic structure of the graphene. Therefore, to obtain nanohybrids it is necessary just to mix the two species in solution and left them under stirring. Several mixtures displaying different weight ratios between complex **13** and GNF were prepared and characterized by UV-Vis absorbance and emission spectra, SEM microscopy, and Raman spectroscopy. Then, the nanohybrids were deposited on a gold interdigitate functionalized silicon to evaluate the photoresponse. These measurements were carried out at Istituto Italiano di Tecnologia (IIT) laboratories in Genova.

Raman Spectroscopy

The Raman analysis reveals several differences compared to GNF alone. First, new bands appear between the D and G bands, which can be attributed to the Raman signals of the porphyrazine. As shown in Figure 3.2.5, the intensity of both the D and 2D peaks decreases, accompanied by a slight blue shift, while the G peak remains essentially unchanged. The D band is associated with structural defects and is related to the breathing modes of aromatic rings. The observed decrease in intensity of the D and 2D bands may be attributed to the interaction between complex **13** and the GNF surface. This interaction likely reduces the effective defect density and alters the vibrational properties of the graphene nanoflakes.

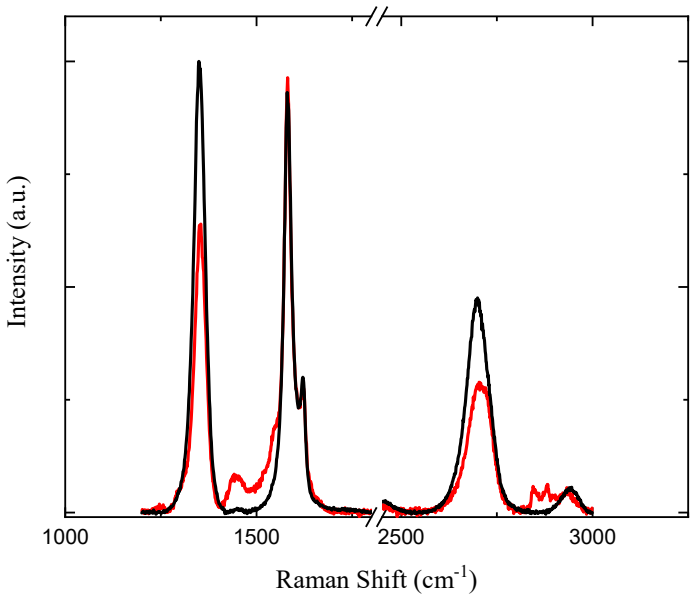

Figure 3.2.5 *Comparison between the Raman spectrum of GNF (black line) and nanohybrids (red line).*

UV-Vis spectroscopy

Mixtures with different ratios of complex **13** and GNF were prepared for UV–Vis absorption and emission spectroscopy (CH_2Cl_2) in order to evaluate whether the relative amounts of the two components influence their electronic interaction. Specifically, solutions with 3:4 and 3:7 (w/w) ratios of complex **13**:GNF were prepared at a porphyrazine concentration of 1.25×10^{-5} M. The UV–Vis absorption spectra (Figure 3.2.6) show a slight increase in overall light absorption with increasing GNF content. More significant effects are observed in the emission spectra: upon excitation at 360 nm, increasing the amount of GNF leads to stronger fluorescence quenching, along with the growth of a band around 580 nm, which can be attributed to the contribution of graphene (Figure 3.2.7).

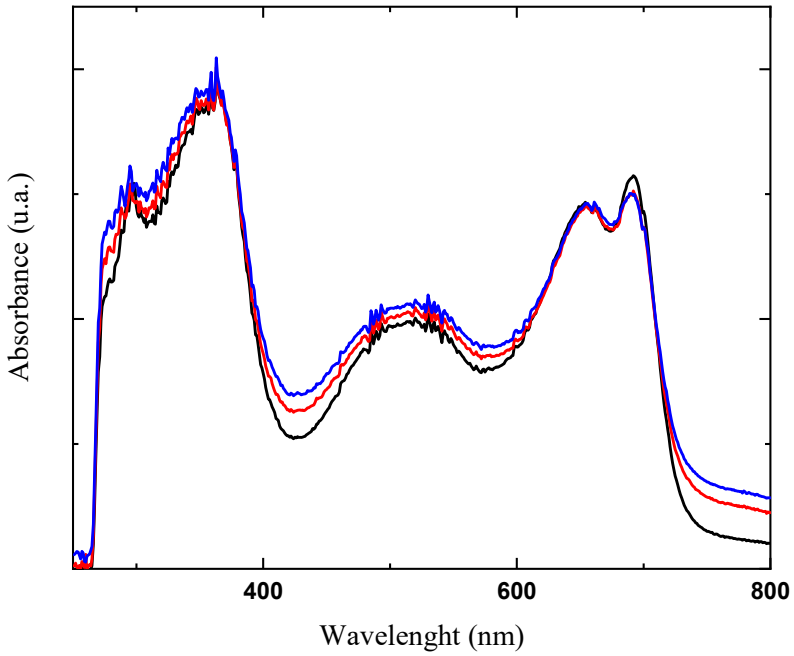

Figure 3.2.6 *UV-Vis absorption spectra of complex* ***13*** *(black line) 3:4 nanohybrid solution (red line), 3:7 nanohybrid solution (blue line).*

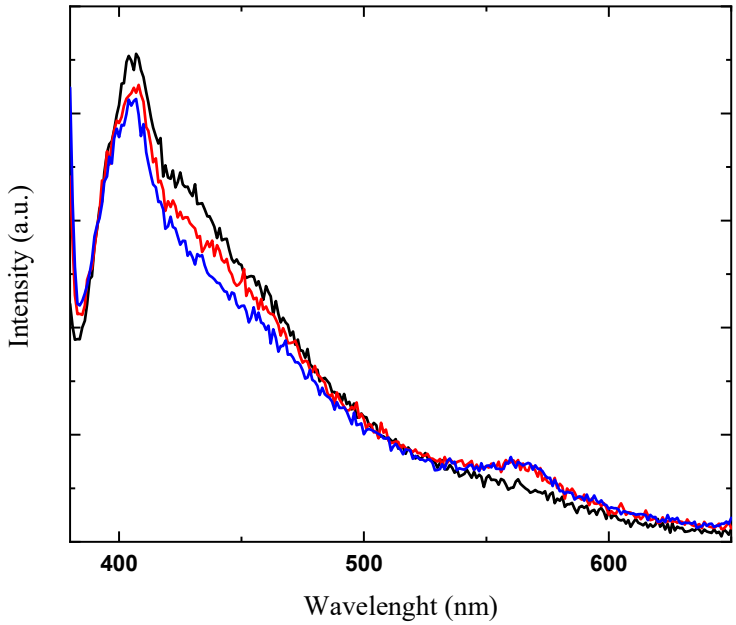

Figure 3.2.7 *UV-Vis emission spectra of complex* ***13*** *(black line), nanohybrid solution 3:4 (red line) nanohybrid solution 3:7 (blue line).*

SEM and TEM analysis

Microscopy analysis was also carried out to investigate the morphological changes occurring at the material surface. SEM measurements were performed at the Istituto Italiano di Tecnologia (IIT). Images of both GNF and nanohybrid samples were collected after coating the sample surface with a thin layer of gold. For the nanohybrid system, a solution with a 3:4 w/w ratio of **13** to graphene nanoflakes was prepared and deposited onto a glass substrate. For comparison, a control sample consisting of a glass substrate functionalized with graphene nanoflakes alone was also prepared.

By comparing the two samples, clear morphological differences can be observed. In the case of pristine graphene nanoflakes, the edges appear clean and well-defined. In contrast, the nanohybrid sample shows flakes with more irregular, blunt, and roughened edges. This difference provides further evidence that the interaction between **13** and graphene nanoflakes induces modifications at the surface of the material.

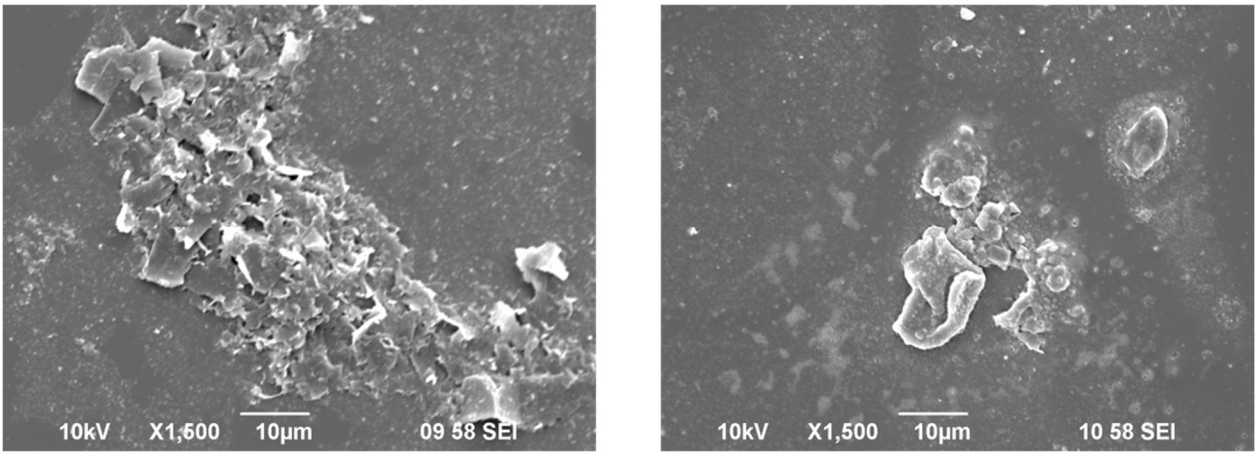

Figure 3.2.8 *SEM images of graphene nanoflakes (left image) nanohybrids of complex* ***13****/Graphene nanoflakes (right image).*

3.3 Devices fabrication

To evaluate the activity and photoresponse of complex 13, a gold interdigitated electrode device (area: 1 cm²) on a silica substrate was fabricated at the Istituto Italiano di Tecnologia (IIT). The device featured an inter-finger spacing of 10 µm, designed to minimize charge recombination. Two devices were prepared using different coating techniques—spray coating and drop casting—in order to assess the influence of the deposition method on the electrical properties of the material.

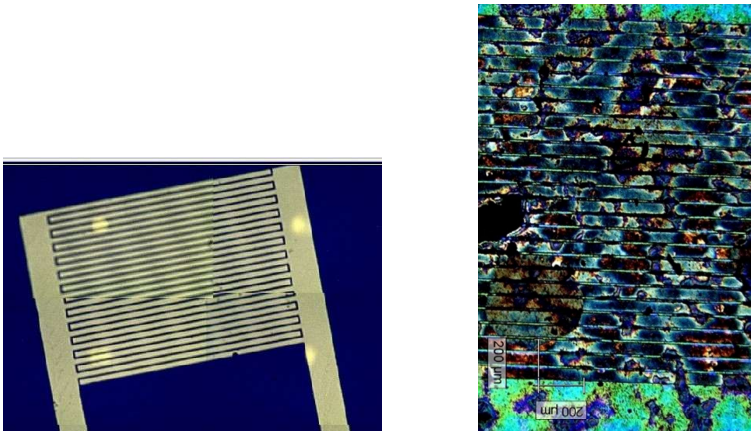

Figure 3.3.1 *Optical microscope images of* ***(left)*** *same disposal after coating* ***(right)****.*

Electrical characterization revealed no measurable photocurrent under illumination. However, a dark current was observed at 0 V, and the current–voltage behaviour exhibited an ohmic response. In both devices, the measured resistance was relatively low, approximately 17 Ω and 65 Ω under vacuum conditions, with a slight increase when measured in air.

These results can be interpreted in different ways. The absence of photocurrent may be attributed to the relatively large spacing (10 μm) between the interdigitated electrodes. In combination with fast charge recombination processes, this could hinder efficient charge collection, preventing the detection of a photocurrent. Therefore, further experiments with reduced electrode spacing are recommended.
Additionally, the observation of current flow at 0 V indicates that the material is intrinsically conductive (i.e., in an "ON" state even applied bias). This behaviour suggests the presence of charge carriers or conductive pathways within the material, which may arise from the interaction between complex **13** and the graphene nanoflakes.
This can be explained with a combination of intrinsic mechanisms of the material and properties of the device:

- **Intrinsic Residual Polarization**, happen when there is difference between the electrodes and active material's work function can create a inner polarization that generate a electrical field that allow the movement of charge carriers at 0V.
- **Dark current,** due to the thermal movement of charge carriers.
- **Asymmetric Rectifying Effects**, if the electrodes form a Schottky junction with the active material, an energy barrier can be created that favors the flow of charges in one direction. The barrier is not symmetrical with respect to V=0, generating a residual current even in the absence of voltage. This phenomenon is common in rectifying devices, such as diodes.
- **Trap and Charge Release Phenomena,** defects or impurities in the graphene or palladium complex can act as charge traps. These traps also release charges at V=0, causing a residual current.

3.4 Conclusions

The structure of the new β-η^1-Pd(II)-thioalkyl porphyrazine complex **13** was elucidated through ^{1}HNMR, ^{13}CNMR and ^{31}PNMR analyses and subsequently confirmed by single-crystal X-ray diffraction (SCXRD). Complex **13** thus represents the first η^1 tetrapyrrole organometallic complex in which the metal is coordinated at the β position of the macrocycle rather than at the *meso*-position, as observed in some porphyrin complexes. The spectroscopic and electrochemical properties of this complex were investigated by UV-Vis analysis and cyclic voltammetry and interpreted by time-dependent density functional theory (TDDFT) computations, enabling the assignment of the molecular orbital origin of the main electronic transitions. Notably, whereas in peripherally aryl-substituted thioalkyl porphyrazines a charge transfer HOMO-LUMO electronic transition occurs between the aryl substituent and the macrocycle core, in complex **13** charge transfer transitions

localized on the $Pd(PPh_3)_2$ substituent occur at significantly higher energies, in correspondence to the Soret band. The spectroscopic and electrochemical properties of complex **13** make this compound promising for OPV applications and the presence of additional of aromatics rings other than the porphyrazine ring on the complex could enhance its interaction with nanocarbon moieties used as acceptors in OPV devices. Therefore, a study on the preparation of nanohybrids with Graphene nanoflakes (GNF) and on their photoresponse has been carried during the required industrial stage at the BeDimensional S.p.A. laboratories in Genova.

First, the preparation of the graphene nanoflakes was carried out by a Liquid Exfoliation process using graphite in dimethylformamide (DMF). After ultrasonication and centrifugation processes, supernatant was analysed by Raman Spectroscopy, AFM, TEM and SEM microscopy to evaluate nanoflakes purity and size distribution. Secondly, nanostructured hybrid materials with different **13**:GNF w/w ratio were prepared. The formation of the nanohybrids were confirmed by UV-Vis spectroscopy, observing a spectral enhancement, and by emission spectroscopy which, on the contrary, showed luminescence quenching. TEM and SEM microscopy analyses also showed the nanohybrids size. Finally, photodetectors were fabricated by depositing a film of these nanohybrids by spray coating methods onto a 10μm gold interdigitate electrode on Si wafer support. Preliminary tests on the photoactivity properties of **13**/GNF nanohybrids have been carried out but, unfortunately, they showed no photocurrent production under device illumination.

3.5 Methods and Experimental

3.5.1 General

All chemicals and solvents (Aldrich) were of reagent grade. Solvents were dried and distilled before use according to standard procedures. Solvents used in physical measurements were of spectroscopic or HPLC grade. Silica gel used for chromatography was Merck Kieselgel 60 (70-230 mesh), 20x20 cm plates for thin layer chromatography (TLC) were Macherey-Nagel 0.2mm F254 on aluminium substrate and Merck 0.5mm or 1.0mm on glass substrate. UV-Vis spectra were registered in liquid at ~10-6M in CH_2Cl_2 at room temperature, in the 250-800nm region using UV-Vis Cary 50 and 1cm quartz sample cells. ^{1}H-NMR and ^{13}C-NMR spectra were registered in $CDCl_3$ with 400MHz INOVA Varian.

UV-vis spectra were recorded in the 250-800 nm range by UV-vis Cary 50 spectrophotometer and UV-Vis/NIR Jasco V-770 spectrometer in 1 cm path length quartz cells and solution of *ca.* 10^{-6}M, scan rate 600nm/min. The cyclic voltammetry (CV) and differential pulse voltammetry (DPV) experiments were performed with an EG & G Princeton Applied Research Model 263A potentiostat/galvanostat. Data were collected and analysed by the Model 270 electrochemical analysis system software[21]. A standard three-electrode arrangement was employed. The working electrode was a glassy carbon button (Ø = 3 mm). A platinum wire served as counter electrode and a home-made AgCl/Ag electrode containing saturated KCl was used as the reference electrode. All the oxidation and reduction potentials are reported relative to the ferrocene/ferrocenium (Fc/Fc^+) potential scale, using the voltametric oxidation of ferrocene as an internal reference. The reproducibility of individual potential values was within ± 5 mV. All the electrochemical measurements were carried out using Schlenk techniques (N_2) at room temperature. The concentration of the supporting electrolyte [$N(C_4H_9$-*n*$)_4BF_4$] was typically of 0.15 M. Cyclic voltammograms were recorded by scanning the potential at 200 mVs^{-1}. DPV measurements were performed at 5 mVs^{-1} with a pulse height of 50 mV and 50 ms pulse width. Photoluminescence emission spectra of the nanohybrids were recorded at room temperature in quartz cells with an Agilent Cary Eclipse fluorescence spectrometer with excitation at 360 nm. Raman measurements were collected with a Renishaw inVia confocal Raman microscope with excitation line of 532 nm (2.33 eV) with a 50× objective lens and an incident power of ≈1 mW on the samples. The GNF dispersions were drop cast onto Si/SiO_2 wafer (300 nm thermally grown SiO_2, LDB Technologies Ltd.) and dried under vacuum. 50 spectra were collected for each sample; Lorentzian functions were used to fit the peaks. GNF were characterized morphologically by transmission electron microscopy (TEM) (operated at 100 kV, JOEL JEM 1011). The materials were dropped with a pipette on holey carbon 200 mesh grids and dried under vacuum overnight. Field-

emission scanning electron microscopy (SEM) was also performed on samples drop cast onto Si wafer (JoelJSM-7500FA). Atomic Force microscopy (AFM) measurements were performed with a XE-100 AFM (Park System, Korea) by means of PPP-NCHR cantilevers (Nanosensors, Switzerland) having a tip diameter <10 nm. The images were collected in intermittent contact (tapping) mode on an area of 5 x 5 μm^2 (1024 x 1024 data points) using a drive frequency of 330 kHz and keeping the working set point above 70% of the free oscillation amplitude. The scan rate for the acquisition of the images was 0.2 Hz. The crystallographic analysis of porphyrazine compound **13** has been performed X-ray diffraction data were measured in flowing N_2 at 173 K using a Bruker-Nonius KappaCCD four-circle diffractometer equipped with an Oxford Cryostream-700 apparatus (graphite monochromated MoKα radiation, λ = 0.71073 Å, CCD rotation images, thick slices, φ and ω scans to fill the asymmetric unit). Reduction of data and semiempirical absorption correction were done using SADABS program[22]. The structure was solved by direct methods with SIR97 program[23] and refined by the full-matrix least-squares method on F^2 using the SHELXL-2019/2 program[24] with the aid of the program WinGX. The figures were generated using ORTEP-3.[25]

3.5.2 Synthesis

The *free-base* thioethyl porphyrazines **3**[26] their non-symmetrically H-substituted counterpart **4**[27] and the Br-substituted porphyrazines **5**[10] were prepared according to previously described procedures.

2-[bromo-trans-bis(triphenylphosphino)-palladium(II)] 3, 7, 8, 12, 13, 17, 18-heptakis (ethylthio)-5, 10, 15, 20-21H, 23H porphyrazine **(13)**

Compound **5** (70 mg; 0.086 mmol) was dissolved in 35 mL anhydrous toluene. Then $Pd(PPh_3)_4$ (95 mg; 0.082 mol) was added to the solution. The mixture was heated at reflux, checked by TLC and stopped after approximately 40 minutes. Excess solvent was removed under reduced pressure and the crude product was purified on silica gel column using CH_2Cl_2:*n*-hexane 7:3, *v*:*v* and then by preparative TLC with the same eluent mixture. Complex **13** was isolated collecting the second eluted band (R_f =0.17). Exchange of Br atom with Cl took place during the chromatographic purification with CH_2Cl_2 solvent. A first band (R_f =0.37) was then collected corresponding to the analogous complex **13** containing Cl atom instead Br. The collected first and second band provided **13** in 80% overall yield. ^{1}H NMR (400 MHz, $CDCl_3$), δ/ppm: -1.85 (s, 2H, Np*H*), 1.10 (t, J = 7.6 Hz, 3H, CH_3), 1.41 (t, J = 7.6 Hz, 3H, CH_3), 1.43 (t, J = 7.6 Hz, 3H, CH_3), 1.5-1.7 (m, 12 H, CH_3), 3.75 (q, J = 7.6 Hz, 2H, SCH_2), 3.89 (q, J = 7.6 Hz, 2H, SCH_2), 3.95 (q, J = 7.6 Hz, 2H, SCH_2), 4.0–4.2 (m, 8H, SCH_2), 6.6–6.7 (m, 6H, Ph *p*-H), 6.7–6.8 (m, 12H, Ph *m*-H), 7.6–7.8 (m, 12H, Ph *o*-H). ^{13}CNMR (100 MHz, $CDCl_3$), δ/ppm: 14.98(*C*H_3), 15.49(*C*H_3), 15.57(*C*H_3), 15.65(*C*H_3), 15.73(*C*H_3), 29.32 (*C*H_2), 29.49 (*C*H_2), 29.69 (*C*H_2), 29.84 (*C*H_2), 127.31 (s, Ph *m*-*C*), 129.63 (s, Ph *p*-*C*), 130.40 (t, Ph *ipso*-

C), 134.48 (t, Ph *o*-*C*), 137.00, 137.17, 139.50, 140.83, 141.93, 142.92, 143.42, 144.81, 147.37, 152.08, 159.67, 159.88, 161.20, 162.25, 165.91, 169.28. ^{31}PNMR (162 MHz, $CDCl_3$), δ/ppm: 24 (s). UV-Vis (CH_2Cl_2), $\lambda_{max.}$/nm 307, 363 (Soret), 515 (extra band), 650 and 693 (Q bands).

Graphene nanoflakes

The preparation of graphene nanoflakes (GNF) and porphyrazine/GNF nanohybrids as well as their Raman and microscopy characterizations were carried out at BeDimensional S.p.A. Company and at IIT (Istituto Italiano di Tecnologia) in Genova. In a 50 mL vial of graphite (500 mg) (AMG Graphite) was weighted and then DMF (50 mL) was added. The vial was then sealed and submerged in an ultrasonic bath (VWR Ultrasonic Cleaner USC - THD) for ten hours splitting the whole time in 10 one-hour intervals to permit the cooling of the water under 35°C. After this step, the supernatant was transferred into a Falcon tube and centrifuged for 4 hours at 3840 rpm, which is the maximum speed allowed for Falcon tubes using DMF as solvent. The centrifugation was carried out at 12 °C with an acceleration ramp set to 9. Following centrifugation, the supernatant was carefully collected, and a 1 mL aliquot of the dispersion was taken to determine the concentration using the evaporation method.

3.5.3 Computational details

Compound **3** geometry has been taken from a previous work of the research group where this thesis was carried on[9] while the geometry of complex **13** has been taken from the SCXRD coordinates and further optimized at DFT/B3LYP/def2-svp/gas phase substituting, for simplicity, the pendant ethyl groups with methyl moieties. No negative frequencies have been found suggesting a real minimum found. Both structures have been submitted to TDDFT calculations at wB97X-D3/def2-TZVP/CPCM(DCM) level of theory, taking into account the first 100 states with ORCA 6 software.[28] The molecular orbitals have been generated with the use of Avogadro 2 software.[29] The wB97X-D3 functional[30] is a modern Long-range corrected hybrid density functionals with improved dispersion corrections. TDDFT/M06/def2-TZVP/CPCM(CH_2Cl_2) and (DMF) level of theories have been used for HOMO and LUMO energies calculation to be compared with experimental electrochemical data.

3.5.4 Photoresponse experiments

Interdigitated gold electrodes were fabricated on Si/SiO_2 substrates by UV lithography with an SUSS MicroTec MJB4 mask aligner. The lithography and development of the positive photoresist were followed by thermal evaporation of chromium/ gold (thickness 9 nm/40 nm) and lift off. 20 μL of **13**/GNF solution in DMF (3:4 weight ratio) 0.5 mg mL^{-1} was drop cast or 5 mL of the same solution was sprayed. Photodetection experiments were performed under ambient conditions. Monochromatic light was obtained from a xenon lamp coupled to a monochromator (Spectral Products CM110) and

brought to the sample with a system of lenses and mirrors in order to illuminate the device area. In this condition, the spectral responsivity was simply calculated as the ratio between the measured photocurrent density and the optical input power density for each light wavelength. Light power was measured using a calibrated Si photodiode (ThorlabsS120VC). DC bias and current measure were provided by a Keithley 2612 sourcemeter. Light was modulated with a mechanical chopper, and AC photocurrent was acquired using a current preamplifier (DL 1211) and lock-in amplifier (Signal Recovery 7265). Spectral responsivity and *IV* curves of the photodetectors were acquired at 857 Hz. The detection limit of the measurement setup was equal to 1 nA. Transient currents under chopped 1 Sun illumination (xenon light source equipped with AM 1.5 G filters) were acquired with a sampling period of 0.4 s and a light switching period of 5 s.

3.6 References

1. Belviso, S.; Larotonda, G.; Santoro, E.; Santarsiere, A.; Tuzi, A.; *Dalton Trans.*, **2025**, *54*, 11563-11572
2. N. Miyaura and A. Suzuki, *Chem. Rev*., 1995, **95**, 2457–2483.
3. K. Sonogashira, Y. Tohda and N. Hagihara, *Tetrahedron Lett*., 1975, **16**, 4467–4470.
4. (a) Arnold, D. P.; Sakata, Y.; Sugiura, K.-I.; Worthington, E. I. *Chem. Commun.* **1998**, 2331–2332. (b) Hodgson, M. J.; Healy, P. C.; Williams, M. L.; Arnold, D. P. *J. Chem. Soc., Dalton Trans.* **2002**, 4497–4504. (c) Hartnell, R. D.; Arnold, D. P. *Organometallics* **2004**, *23*, 391–399. (d) Hodgson, M. J.; Borovkov, V. V.; Inoue, Y.; Arnold, D. P. *J. Organomet. Chem.* **2006**, *691*, 2162–2170. (e) Jiang, M. Y.; Shin, J.-Y.; Patrick, B. O.; Dolphin, D. *Dalton Trans.* **2008**, 2598–2602.
5. (a) Matano, Y.; Matsumoto, K.; Nakao, Y.; Uno, H.; Sakaki, H.; Imahori, H. *J. Am. Chem. Soc.* **2008**, *130*, 4588–4589. (b) Matano, Y.; Matsumoto, K.; Hayashi, H.; Nakao, Y.; Kumpulainen, T.; Chukharev, V.; Tkachenko, N. V.; Lemmetyinen, H.; Shimizu, S.; Kobayashi, N.; Sakamaki, D.; Ito, A.; Tanaka, K.; Imahori, H. *J. Am. Chem. Soc.* **2012**, *134*, 1825–1839.
6. Pregosin, P. S.; Kunz, R. *Helv. Chim. Acta* **1975**, *58*, 49–50..
7. (a) Pidcock, A. *Chem. Commun.* **1968**, 92; (*b*) Verstuyft, A. W.; Nelson, J. H.; Cary, L. W. *Inorg. Chem.* **1976**, *15*, 732–734.
8. (a) Ricciardi, G.; Bencini, A.; Belviso, S.; Bavoso, A.; Lelj, F. *J. Chem. Soc., Dalton Trans.* **1998**, 1985–1991.(b) Ricciardi, G.; Bavoso, A.; Bencini, A.; Rosa, A.; Lelj, F.; Bonosi, F. *J. Chem. Soc., Dalton Trans.* **1996**, 2799–2807.(c) Arnold, D. P.; Healy, P. C.; Hodgson, M. J.; Williams, M. L. *J. Organomet. Chem.* **2000**, 607, 41–50.
9. Ghidinelli, S.; Abbate, S.; Santoro, E.; Belviso, S.; Longhi, G. *J. Phys. Chem. B* **2021**, *125*, 264–280.
10. Belviso, S.; Amati, M.; Rossano, R.; Crispini, A.; Lelj, F. *Dalton Trans*. **2015**, *44*, 2191-2207.
11. Belviso, S.; Capasso, A.; Santoro, E.; Najafi, L.; Lelj, F.; Superchi, S.; Casarini, D.; Villani, C.; Spirito, D.; Bellani, S.; Del Rio-Castillo, A. E.; Bonaccorso, F. *Adv. Funct. Mater.* **2018**, *28*, 1705418
12. Belviso, S.; Santoro, E.; Penconi, M.; Righetto, S.; Tessore, F. *J. Phys. Chem. C* **2019**, *123*, 13074–13082
13. Belviso, S.; Marsico, G.; Franzini, R.; Villani, C.; Abbate, S.; Longhi, G. *Dalton Trans.* **2022**, *51*, 16453–16464.
14. Bottomley, L. A.; Chiou, W. H. *J. Electroanal. Chem.* **1986**, *198*, 331–346.
15. Ough, E. A.; Creber, K. A. M.; Stillman, M. *Inorg. Chim. Acta* **1996**, *246*, 361–369.
16. Liu, Y.; Liu, M. S.; Li, X.-C.; Jen, A. K.-Y. *Chem. Mater.* **1998**, *10*, 3301–3304.
17. Pommerehne, J.; Vestweber, H.; Guss, W.; Mahrt, R. F.; Bässler, H.; Porch, M.; Daub, J. *Adv. Mater.* **1995**, *7*, 551–554.
18. Mussini, P. R.; Orbelli Biroli, A.; Tessore, F.; Pizzotti, M.; Biaggi, C.; Di Carlo, G.; Lobello, M. G.; De Angelis, F. *Electrochim. Acta* **2012**, *85*, 509–523.
19. Bonaccorso, F., Bartolotta, A., Coleman, J. N. & Backes, C. *Advanced Materials*, **2016**, *28*, 6136–6166.

20. del Rio Castillo, A. E.; Pellegrini, V.; Ansaldo, A.; Ricciardella, F.; Sun, H.; Marasco, L.; Buha, J.; Dang, Z.; Gagliani, L.; Lago, E.; Curreli, N.; Gentiluomo, S.; Palazon, F.; Prato, M.; Oropesa-Nuñez, R.; Toth, P. S.; Mantero, E.; Crugliano, M.; Gamucci, A.; Tomadin, A.; Polini, M.; Bonaccorso, F. *Mater Horiz* **2018**, *5*, 890–904.

21. A. J. Bard, L. R. Faulkner, *Electrochemical Methods, Fundamentals and Applications*; John Wiley & Sons: New York, **1980**

22. *SADABS User Manual*; Bruker Nonius BV: Delft, The Netherlands, **2002**

23. Altomare, A.; Burla, M. C.; Camalli, M.; Cascarano, G. L.; Giacovazzo, C.; Guagliardi, A.; Moliterni, A. G.; Polidori, G.; Spagna, R. *J. Appl. Crystallogr.* **1999**, *32*, 115.

24. Sheldrick, G. M. *Acta Crystallogr., Sect. C* **2015**, *C71*, 3

25. Farrugia, L. J. *J. Appl. Crystallogr.* **2012**, *45*, 849

26. (a) Lelj, F.; Morelli, G.; Ricciardi, G.; Roviello, A.; Sirigu, A. *Liq. Cryst*. **1992**, *12*, 941-960. (b) Belviso, S.; Ricciardi, G.; Lelj, F *J. Mater. Chem.* **2000**, *10,* 297–304. (c) Belviso, S.; Amati, M.; De Bonis, M.; Lelj, F. *Mol. Cryst. Liq. Cryst*. **2008**, *481*, 56-72. (d) Belviso, S.; Cammarota, F.; Rossano, R.; Lelj, F. *J. Porphyrins Phthalocyanines* **2016**, *20*, 223-233

27. Belviso, S.; Ricciardi, G.; Lelj, F.; Monsù Scolaro, L.; Bencini, A.; Carbonera, C. *J. Chem. Soc., Dalton Trans.* **2001**, 1143-1150

28. Neese, F. *Comput. Mol. Sci*., **2012**, *2*, 1, 73–78.

29. (*a*) Hanwell, M. D.; Curtis, D. E.; Lonie, D. C.; Vandermeersch, T.; Zurek, E.; Hutchison, G. R. *J. Cheminform.*, **2012**, *4*, 17; (*b*) Other relevant publications that might be of interest: Hanwell, M. D.; de Jong, W. A.; Harris, C. J. *J. Cheminform.*, **2017**, *9*, 55; (*c*) de Jong, W. A.; Walker, A. M.; Hanwell, M. D. *J. Cheminform*, **2013**, *5*, 25.

30. Lin, Y.-S.; Li, G.-D.; Mao, S.-P.; Chai, J.-D. *J. Chem. Theory Comput*., **2013**, *9*, 263–272.

Chapter 4

Bulk Heterojunction solar cells with thioethyl porphyrazines

In this chapter, the preparation and characterization of bulk heterojunction solar cells, with the active layer based on the thioethyl porphyrazines described in the previous chapters, will be discussed. All the characterizations and preparations of the cells were carried out in the laboratories of the Institute of Emerging Technologies at the Hellenic Mediterranean University of Crete, under the supervision of prof. Emmanuel Kymakis of the Nanomaterials for Emerging Devices.

To the best of our knowledge, BHJ solar cells incorporating thioalkyl porphyrazines as donor materials have not been previously reported. Consequently, the experimental work was structured into three main stages:

- Device architecture choice and fabrication of reference solar cell.
- Optimization of thin-film formation and morphology.
- Fabrication of complete BHJ devices using thioalkyl porphyrazines as donor component.

4.1 Device architecture and reference cell fabrication

For device fabrication, an inverted bulk heterojunction architecture was adopted owing to its enhanced operational stability and generally higher power conversion efficiency compared to conventional organic photovoltaic configurations. This improvement is achieved by reversing the conventional sequence of functional layers.[1] In inverted OPVs,[2] as schematically shown in Figure 4.1.1(b), the electron transport layer (ETL) is deposited onto the transparent electrode, while the hole transport layer (HTL) is placed on top of the active layer. Consequently, the role of the electrodes is inverted with respect to conventional architectures: indium tin oxide (ITO) acts as the cathode, whereas a high–workfunction metal serves as the anode.

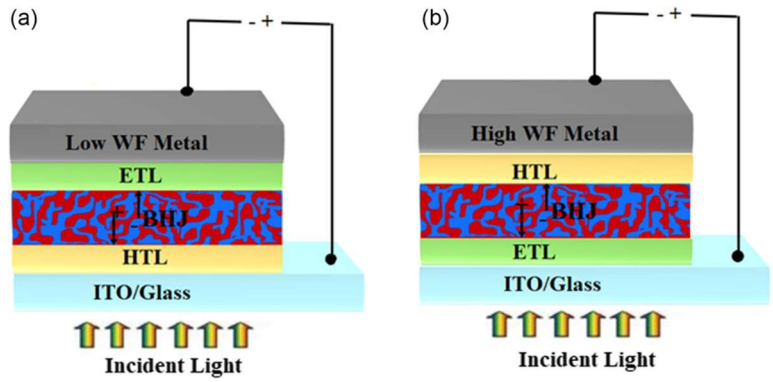

Figure 4.1.1 *(a) Conventional layer structure for OPV solar cells; (b) inverted layer structure for OPV solar cells.*

The device structure for the inverted solar cell employed in this thesis can be summarized as follows:

- Glass/ITO as cathode electrode
- ZnO as electron transport layer (ETL)
- Active layer
- MoO_x as the hole transport material (HTL)
- Ag as the anode electrode

Reference solar cell

As reference system, blends of poly(3-hexylthiophene) (P3HT) with either $PC_{71}BM$ or $PC_{60}BM$ (structure shown in Figure 4.1.2) were selected as the active layer. This donor-acceptor system is among the most extensively investigated in the literature and it is known for its good stability and reproducibility, typically yielding power conversion efficiencies (PCEs) in the range of 2-3%.[2] Furthermore, the P3HT: fullerene system is well suited for the incorporation of additional molecular components, enabling the development of ternary organic solar cells.[3] ZnO and MoO_x were chosen as ETL and HTL, respectively, due to their widespread use, favourable alignment of the energy-levels, and proven compatibility with inverted BHJ architectures.[3]

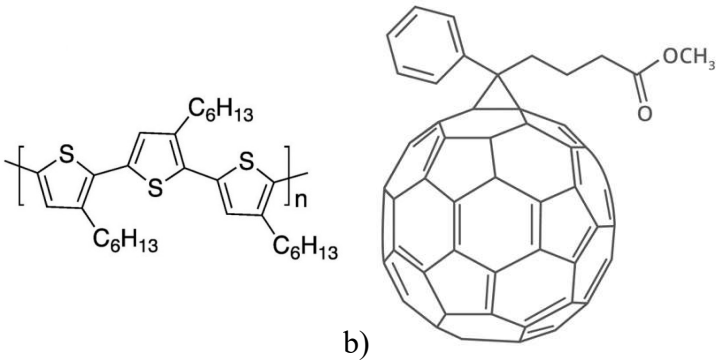

a) b)

Figure 4.1.2 *(a) P3HT (poly-3-hexylthiophene) structure; (b) $PC_{60}BM$ (phenyl-C60-butyric acid methyl ester) structure.*

To build the devices, a glass/ITO support was washed and then ETL and active layer were spin coated. At this point, the HTL and anode was deposed on the substrate by thermal evaporation under N_2 atmosphere. The cell built in this way, was tested under standard AM 1.5G illumination (1 sun). The optimized reference device (J/V curve shown in Figure 4.1.3) exhibited the following photovoltaic parameters: PCE of 3.25%, fill factor (FF) of 66.5%, short-circuit current density (J_{SC}) of −8.17 mA cm^{-2}, and open-circuit voltage (V_{OC}) of 0.598 V.

These values are consistent with those reported in the literature for P3HT-based BHJ solar cells, confirming the reliability of the adopted fabrication protocol.[2]

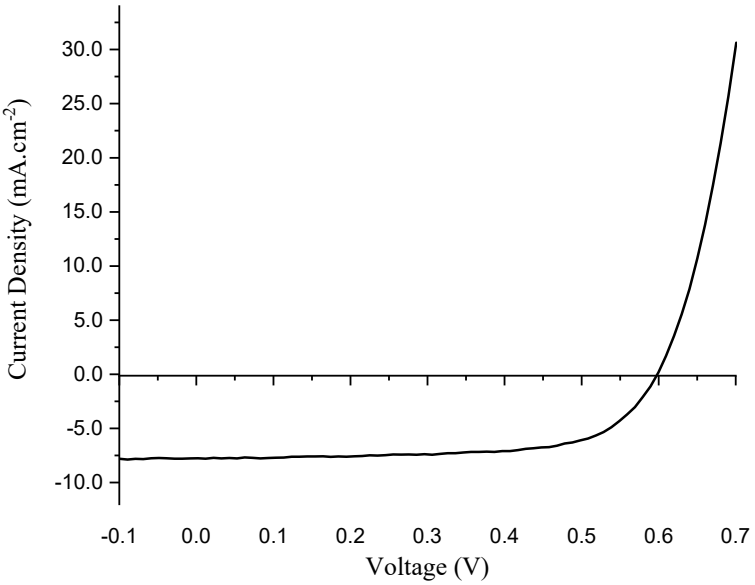

Figure 4.1.3 *Current/voltage diagram for reference cell (J/V curve).*

4.2 BHJ solar cells with porphyrazines as active layer

After establishing the performance of the reference solar cell, BHJ devices incorporating thioethyl-substituted porphyrazines as donor materials were fabricated and evaluated.[4] As these represent the first examples of bulk heterojunction solar cells employing thioalkyl porphyrazines as donor materials, and considering the good performance of the reference device, we attempted to replace the donor P3HT with the thioalkyl porphyrazine while still using $PC_{60}BM$ as the acceptor. The donor molecules used in this thesis are those described in Chapter 2, and their structures are reported in Figure 4.2.1. Detailed fabrication procedures for porphyrazine-based devices are described in the Methods and Experimental.

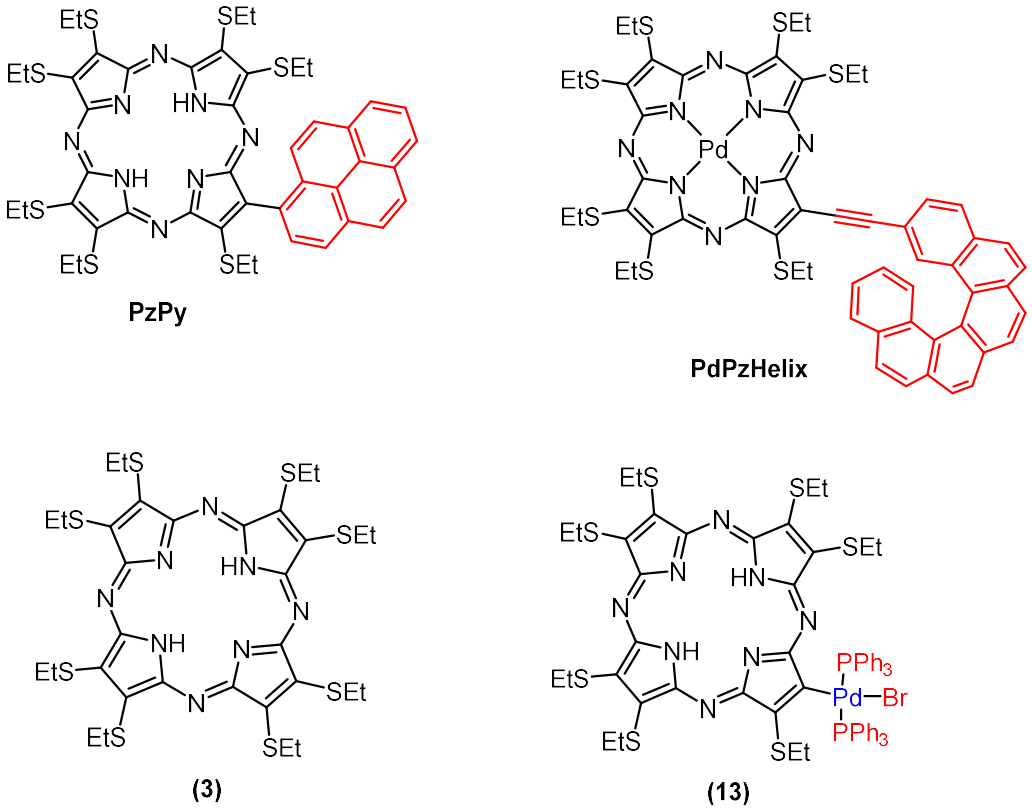

Figure 4.2.1 *Thioethyl porphyrazine employed as donor in BHJ solar cells.*

The obtained cells was tested under AM 1.5G illumination equal to 1 sun light intensity. The photovoltaic parameters obtained for the cells are reported in the following Table 3.

Table 3 *Comparison of the obtained photovoltaic parameters for the BHJ-porphyrazine-based cells.*

Blend	**PCE (%)**	**FF (%)**	**J_{sc} (mA/cm^2)**	**V_{oc} (V)**
3:$PC_{60}BM$	0.10	42.0	-0.77	0.310
PdPzHelix:$PC_{60}BM$	0.09	42.8	-0.52	0.398
PzPy:$PC_{60}BM$	0.06	36.2	-0.71	0.242
13:$PC_{60}BM$	0.04	35.7	-0.72	0.172

Among the investigated compounds, the best photovoltaic performance was obtained for the porphyrazines named as **3** and **PdPzHelix** when blended with $PC_{60}BM$ as acceptor material. Although the efficiencies obtained for these devices are lower than those reported for the most recent and highly engineered tetrapyrrolic donor systems (with a PCE between the 2 and 10%) [5] it should be emphasized that these results represent the first examples of thioalkyl porphyrazines employed as donor materials in BHJ solar cells. As such, they provide a valuable proof of concept and a starting point for further optimization. Several parameters can be systematically optimized to improve device performance. In particular, the donor-to-acceptor ratio plays a crucial role in determining the morphology of the active layer and, consequently, exciton dissociation and charge transport. The choice of acceptor material is another key factor, as it can significantly influence electron mobility, energy-level alignment, and device stability. Additionally, film formation parameters should be carefully controlled. In particular, factors such as the speed used for the spin coating process, the solvent choice, and the post-deposition thermal annealing temperature, can strongly affect the nanoscale morphology and uniformity of the active layer. Attention should also be paid to the electron transport layer and the hole transport layer. Optimising these layers can result in more efficient charge transport and collection, further boosting the performance of the solar cells.

4.3 Morphological characterization of the cells active layer

In the case of the best-performing porphyrazine-based devices **3**:$PC_{60}BM$ and **PdPzHelix**:$PC_{60}BM$ further characterizations of the active layers were carried out by UV–Vis absorption spectroscopy, by atomic force microscopy (AFM) and by X-ray Photoelectron Spectroscopy (XPS).

4.3.1 Compound 3:$PC_{60}BM$

The UV–Vis spectra of thin films obtained by spin-coating deposition of compound **3**, $PC_{60}BM$, and their **3**:$PC_{60}BM$ blend are shown in Figure 4.3.1. The $PC_{60}BM$ film exhibits two absorption bands centered at approximately 360 nm and 450 nm, respectively. The spectrum of the porphyrazine **3** film displays three features: absorptions around 360 nm and 500 nm, along with a broad band spanning the 600–800 nm region, closely resembling its spectral profile in solution. In the case of the **3**: $PC_{60}BM$ blend, the absorption profile clearly combines the bands of both components, indicating that their individual optical properties are largely preserved in the film. Notably, the UV–Vis spectrum of the donor–acceptor blend extends across the entire visible region, resulting in a panchromatic absorption profile. This feature is highly advantageous for photovoltaic applications, as the maximum intensity of the solar emission spectrum lies within the visible range. Consequently, broad absorption across this region is essential for efficient light harvesting and improved device performance.

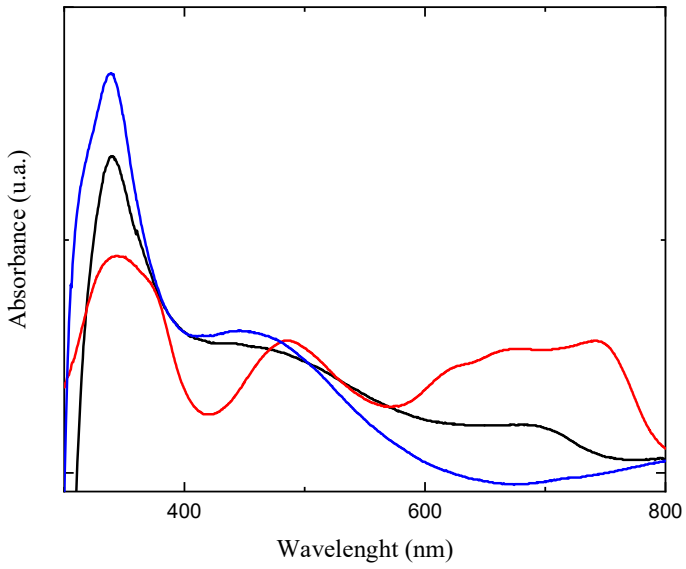

Figure 4.3.1 *UV-Vis absorption spectra on solid state (film) of **3** (red); $PC_{60}BM$ (blue); blend **3**:$PC_{60}BM$ (black).*

AFM measurements were performed to evaluate the surface morphology and roughness of the active layer. Surface roughness is a key parameter for assessing film uniformity and phase distribution. Lower roughness values indicate a more homogeneous film, suggesting effective spreading of the blend over the substrate surface, which is expected to favour efficient charge transport and improved device performance. This favourable characteristic was shown by the topography scan of the **3**:$PC_{60}BM$ film reported in Figure 4.3.2(a).

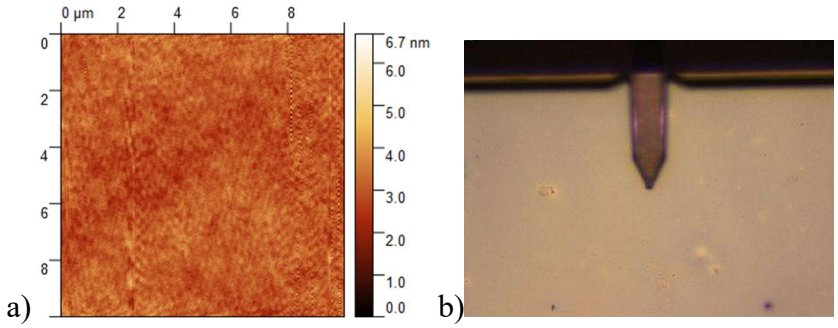

***Figure 4.3.2** (a) Topography scan of **3**:$PC_{60}BM$ film; (b) photography of the same sample recorded by AFM camera.*

X-ray Photoelectron Spectroscopy (XPS) was the last analysis performed and applied to verify the film elemental chemical composition. The analysis was carried out on glass substrates functionalized with the active blend.

Figure 4.3.3 *Images of the glass functionalized sample in XPS sample holder and XPS analysis chamber.*

During this analysis, we focused on specific elements of the porphyrazine. For the blend **3**:$PC_{60}BM$, the focus was on the sulphur atom. We also registered a reference spectrum of compound **3** to check if the interaction between donor and acceptor modified the atomic electrons. The curve fitting of the detailed analysis in the 175~150 eV shows the presence of two peaks (n°2 and 3 in Figure 4.3.4) allied to $S2_{p3/2}$ and to $S2_{p1/2}$ with a binding energy (BE) ascribable, by literature data,[6] to the thiol and thioether compounds. A third peak (n°1 in Figure 4.3.4) is referrable to silicon contamination coming from the glass substrate. A fourth little peak found in the curve fitting could be attributed by position and intensity to shake-up signal or an oxidized sulphur atom. Comparing this with the compound **3** reference, there is no shifting in BE of the main sulphur peaks, this means that the interaction is not involving the sulphur atoms but is a proof of the presence of the thioethyl porphyrazine in the active blend and moreover that the spin-coating and annealing process is not destroying the molecule. Unfortunately, it was not possible to expand the analysis to the carbon and nitrogen atoms due to the presence of molybdenum from the sample holder that significantly modify those regions.

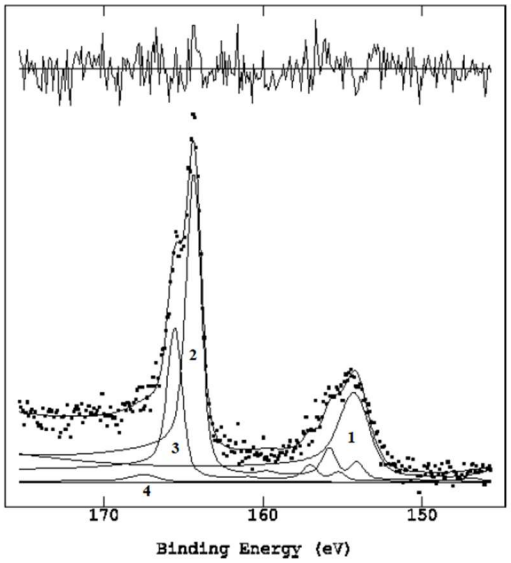

Figure 4.3.4 *Curve fitting of Sulphur region of **3**:$PC_{60}BM$ blend.*

4.3.2 Compound PdPzHelix:$PC_{60}BM$

The cell that uses the complex **PdPzHelix** as donor in active blend, was also characterized as the previous one. As in the previous blend, the UV-Vis spectrum shows a panchromatic absorption profile (Figure 4.3.5) where the absorptions of both the components emerge.

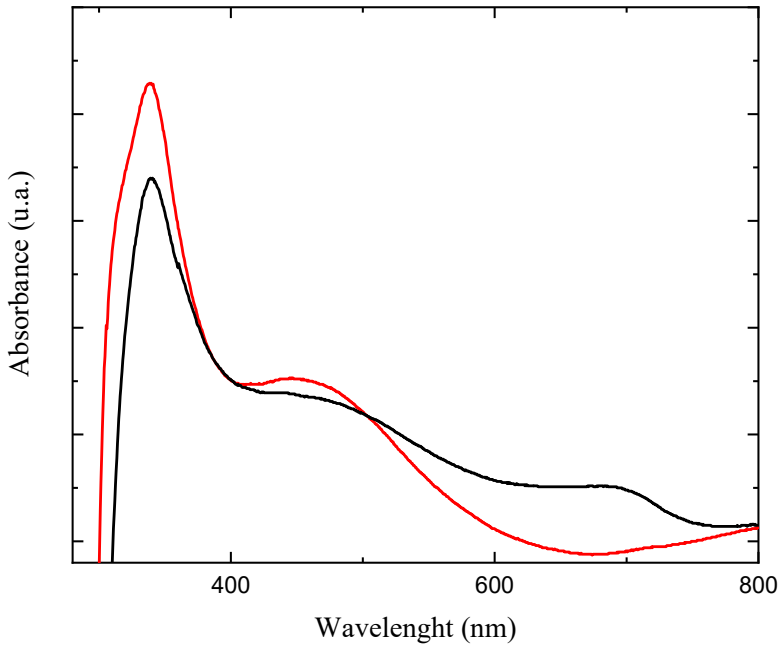

Figure 4.3.5 *UV-Vis absorption spectra of (red) $PC_{60}BM$; (black) blend* ***PdPzHelix****:$PC_{60}BM$.*

AFM measurements were carried out to evaluate the surface morphology and roughness of the active layer. Lower roughness values indicate a more homogeneous film, suggesting effective spreading of the blend over the substrate surface, which in turn favors efficient charge transport and improved device performance. The topography scan of the **PdPzHelix**:$PC_{60}BM$ film, shown in Figure 4.3.6, exhibits favorably low roughness values. Although the roughness of this sample is slightly higher than that of the **3**:$PC_{60}BM$ blend, it remains very low overall, indicating a high degree of film uniformity, as evidenced by the topographical analysis.

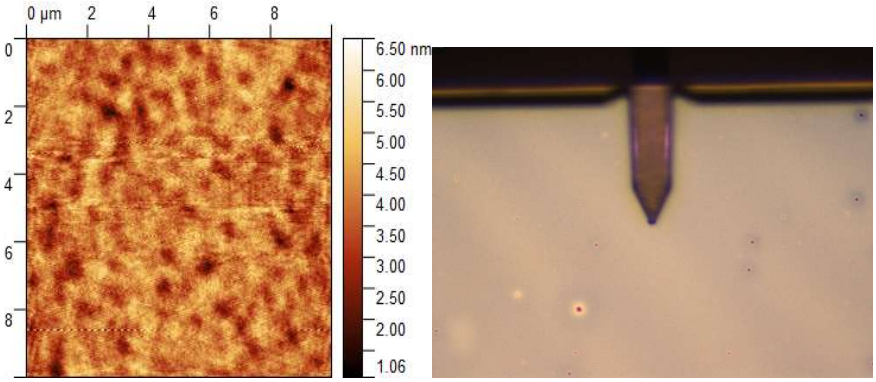

Figure 4.3.6 *(a) Topography scan of* ***PdPzHelix****:$PC_{60}BM$ film; (b) photography of the same sample recorded by AFM camera.*

XPS analysis was carried out following the same procedure adopted for the previous blend, with particular attention devoted to the palladium and sulphur signals. As observed for the **3**:$PC_{60}BM$ sample, the sulphur region in the 150–175 eV range shows no significant shift in peak position, confirming the preservation of the thioethyl-substituted porphyrazine structure.

Further confirmation is provided by the presence of the characteristic palladium peaks. Curve fitting of the 330–345 eV region (Figure 4.3.7) reveals two components attributable to the $Pd3_{p5/2}$ and $Pd3_{p3/2}$ core levels, in good agreement with values reported in the literature for palladium complexes.[7] As in the previous sample, the analysis of the carbon and nitrogen regions is less reliable, due to interference from molybdenum contamination originating from the sample holder.

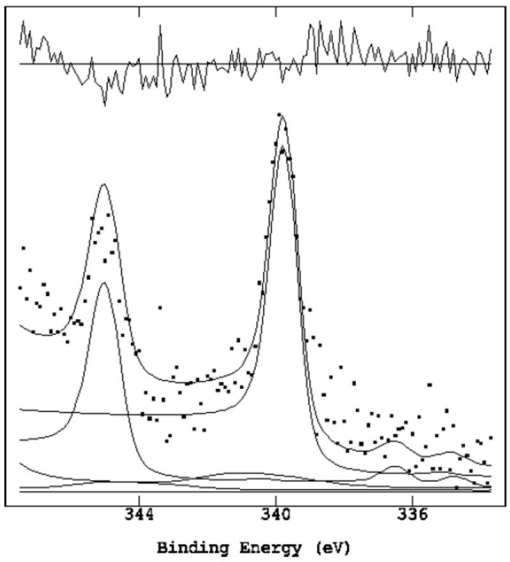

Figure 4.3.7 *Curve fitting of palladium region of compound* ***PdPzHelix****:$PC_{60}BM$ blend.*

4.4 Conclusions

In this chapter, we report the fabrication of the first bulk heterojunction (BHJ) solar cells employing thioalkyl-substituted porphyrazines as donor materials. As a reference system, blend of poly(3-hexylthiophene) (P3HT) with $PC_{60}BM$ was used as the active layer. This donor–acceptor combination is among the most extensively studied in organic photovoltaics and is widely recognized for its excellent stability and reproducibility. Among the investigated compounds, the highest photovoltaic response was obtained for porphyrazines **3** and **PdPzHelix** when blended with $PC_{60}BM$ as acceptor. Although the resulting power conversion efficiencies (PCEs) remain limited, comprehensive characterization of both devices and active layers-performed via AFM, XPS, and UV–Vis spectroscopy on the two best-performing systems-reveals clear indications of untapped potential for performance enhancement. Several key parameters remain open for optimization. In particular, the selection of alternative acceptor materials may enable improved energy-level alignment and enhanced charge-transfer efficiency. Moreover, active-layer morphology can be further tuned through systematic variation of spin-coating parameters (e.g., rotation speed and time), while post-deposition thermal annealing conditions represent an additional critical lever for optimizing nanoscale phase separation and, consequently, device performance.

While the achieved efficiencies are lower than those reported for state-of-the-art, highly optimized tetrapyrrolic donor systems, it is crucial to emphasize that these results constitute the first demonstration of thioalkyl porphyrazines as donor materials in BHJ solar cells. As such, they establish an important proof of concept and provide a solid foundation for further molecular and device optimization.

4.5 Methods and Experimental

Atomic force microscopy (AFM) measurements were performed using a Nanowizard III (JPK Instruments, Germany), mountedonanAxioObserverD1(CarlZeiss, Germany) inverted optical microscope. The images were acquired using a PPPNCHR cantilevers (Nanosensors, USA), which have a tip with a nominal diameter of 10 nm. The image acquisition was performed using a drive frequency of 295 kHz. Intermittent contact mode was used to record the image over an area of 2.5 mm^2 (512data points), using a scan rate of 0.7 Hz. The working set point was set above 70% of the free oscillation amplitude.

XPS spectra were acquired using a PHOIBOS 100 MCD-5 (SPECS) spectrometer, employing an MgKα source (1253.6 eV). The wide scan spectrum was acquired in FRR mode with an energy step of 1 eV and a channel time of 0.5 s. The main signals of each sample were selected for detailed acquisitions (in FAT mode, with a pass energy E° = 9 eV, a channel width of 0.1 eV, and a channel time of 0.5 s) and processed using the Googly curve-fitting software[8,9] for semiquantitative analysis.

Preparation of BHJ solar cells

Initially, glass/ITO substrates were cleaned by sequential sonication for 10 minutes in different solvents: soapy distilled water, acetone, and isopropanol. After cleaning, the substrates were dried under an air flow and subsequently placed in an oven at 70 °C overnight. The ZnO precursor solution was prepared by dissolving 0.1 g of zinc acetate and 0.028 g of ethanolamine in 1 mL of 2-methoxyethanol, followed by stirring at room temperature for 1 hour. The reference cell active-layer blend solution was prepared by dissolving 11.9 mg of P3HT and 8.1 mg of $PC_{60}BM$ in 1 mL of chlorobenzene, corresponding to a 1:0.8 weight ratio. This solution was stirred overnight at 60 °C. Prior to ZnO deposition, the ITO surface was cleaned and activated by plasma treatment. ZnO was then deposited by spin coating: 60 µL of the ZnO solution was dispensed onto the substrate and spun at 4000 rpm for 45 seconds. The resulting films were annealed at 160 °C for 30 minutes (

Figure 4.5.1a). The pre-heated blend solution was subsequently spin-coated to form the active layer by dispensing 30 µL onto the substrate and spinning at 2000 rpm for 60 seconds, followed by thermal annealing at 150 °C for 10 minutes (

Figure 4.5.1 b). All fabrication steps described above were carried out under ambient conditions. Finally, a 10 nm-thick MoO_x layer and a 100 nm-thick Ag layer were deposited onto the functionalized glass substrates by thermal evaporation under a nitrogen atmosphere (

Figure 4.5.1 c). With the Ag electrode in place, the devices were ready for testing.

In the case of the assembly of the porphyrazine-based BHJ solar cells, the active-layer blend solution was modified by using a ratio between porphyrazine:$PC_{60}BM$ of 3:7. The fabrication process followed the same protocol used for the reference solar cell.

Device characterization was performed using a Newport Oriel Sol1A Class ABB solar simulator under standard 1 sun illumination (AM1.5G, 100 mW cm^{-2}).

(a) 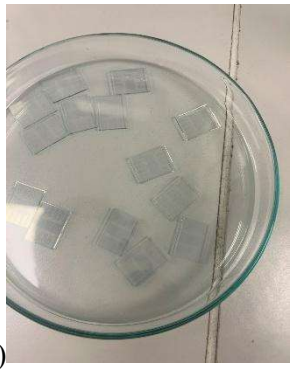 (b) 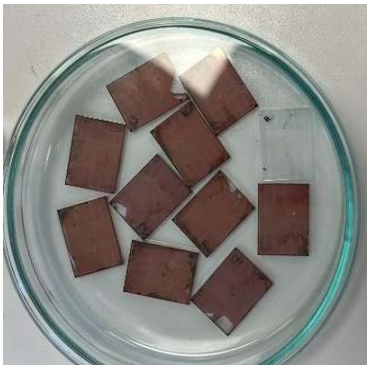 (c) 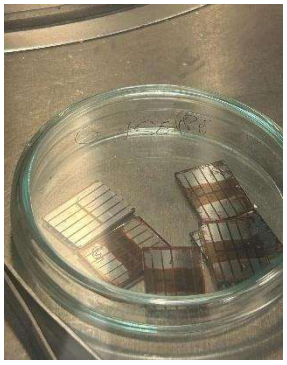

Figure 4.5.1 *(a) Glass-ITO after cleaning; (b) glass-ITO after blend deposition; (c) glass-ITO after Ag deposition.*

4.6 References

1. Wang, K.; Liu, C.; Meng, T.; Yi, C.; Gong, X. *Chem. Soc. Rev.* **2016**, *45*, 2937–2953.
2. Abubaker, S. A.; Pakhuruddin, M. Z. *Energy Technol.* **2024**, *12*, 2400285.
3. *(a)* Zhang, T.; Zhao, X.; Yang, D.; Tian, Y.; Yang, X. *Adv. Energy Mater.* **2018***, 8,* 1701691. (b) Lu, H.; Zhang, J.; Chen, J.; Liu, Q.; Gong, X.; Feng, S.; Xu, X.; Ma, W.; Bo, Z. *Adv. Mater.* **2016***, 28*, 9559–9566. (c) Yang, G.; Wang, Z.; Duan, Y.; Zhao, D.; Yu, J. *Nanoscale Res. Lett.* **2019***, 14,* 266.
4. Cooling, N. A.; Feron, K.; Jones, T. W.; Belcher, W. J.; Dastoor, P. C. *Electronics* **2025**, *14*, 1655.
5. (a) Piradi, V.; Yan, F.; Zhu, X.; Wong, W. Y. *Mater. Chem. Front.* **2021**, *5*, 7119–7133. (b) Kesters, J.; Verstappen, P.; Kelchtermans, M.; Lutsen, L.; Vanderzande, D.; Maes, W. *Adv. Energy Mater.* **2015**, *5*, 1500218.
6. Srinivasan, V.; Stiefel, E. I.; Elsberry, A.; Walton, R. A. *J. Am. Chem. Soc.* **1979**, *101*, 2611.
7. Kadam, A.; Pandit, N.; Survase, A.; et al. *Chem. Afr.* **2026**, *9*, 127.
8. Castle, J. E.; Chapman-Kpodo, H.; Proctor, A.; Salvi, A. M. *J. Electron Spectrosc. Relat. Phenom.* **2000**, *106*, 65–80
9. Castle, J. E.; Salvi, A. M. *J. Electron Spectrosc. Relat. Phenom.* **2001**, *114–116*, 1103–1113.

Conclusions

Non-symmetrically substituted porphyrazines represent a highly promising class of materials for organic photovoltaic (OPV) applications. In this context, the present PhD work was aimed at the design, synthesis, and characterization of thioalkyl-substituted porphyrazines and their metal complexes, with particular focus on their electronic properties and potential implementation in both dye-sensitized solar cells (DSSCs) and bulk heterojunction (BHJ) devices.

Molecular design was guided by the introduction of functional groups capable of promoting anchoring to TiO_2 surfaces, as well as extended aromatic moieties to enhance π–π interactions with carbon-based nanostructures. First, we chose to insert on the macrocycle a heteroaromatic thiophene moiety, widely employed in photoactive materials, also bearing a methylester group, for the effectiveness of carboxylic acid in anchoring to TiO_2. Accordingly, a novel carboxy ester thiophene-based functionalization at the β-position of the porphyrazine macrocycle was successfully achieved by two distinct synthetic strategies: a multi-step route involving asymmetrization, bromination, and Suzuki cross-coupling, and a more direct Liebeskind–Srogl coupling approach. However, the inability to obtain the free carboxylic acid functionality by hydrolysis of the ester moiety prevented the evaluation of these systems as DSSC sensitizers. In parallel, thioalkyl porphyrazines bearing extended aromatic substituents, such as pyrene and helicene units, were synthesized to be investigated for BHJ applications. In this framework, a novel β-η^1-Pd(II) porphyrazine complex was obtained and fully characterized by spectroscopic techniques and single-crystal X-ray diffraction. This compound represents an unprecedented example of a tetrapyrrolic system featuring metal coordination at the β-position of the macrocycle. Combined spectroscopic, electrochemical, and theoretical (TDDFT) studies revealed distinctive electronic features, including charge-transfer transitions at higher energies localized on the $Pd(PPh_3)_2$ fragment, suggesting potential relevance for optoelectronic applications. The interaction of such complex with carbon nanostructures was further explored during an industrial stage at the BeDimensional S.p.A. laboratories in Genova through the preparation of nanohybrids with graphene nanoflakes (GNF), obtained via liquid-phase exfoliation. Hybrid formation was confirmed by spectroscopic and microscopic analyses, highlighting luminescence quenching and enhanced absorption features. Nevertheless, preliminary photodetector devices fabricated from these materials did not exhibit measurable photocurrent, indicating that further optimization is required.

Finally, the first examples of BHJ solar cells employing thioalkyl porphyrazines as donor materials were fabricated and evaluated during a stage at the Institute of Emerging Technologies at the Hellenic Mediterranean University of Crete. Among the investigated compounds, the best photovoltaic

performance was achieved with symmetrical porphyrazines **3** and unsymmetrical **PdPzHelix** porphyrazine Pd(II) complex when blended with $PC_{60}BM$ as the acceptor material. Although the achieved power conversion efficiencies remain modest, these results constitute a significant proof of concept, demonstrating the feasibility of employing such systems in OPV devices.

For sake of clarity, the main electronic properties of the studied compounds are summarized in Table 4 and their molecular structures shown in Figure 4.

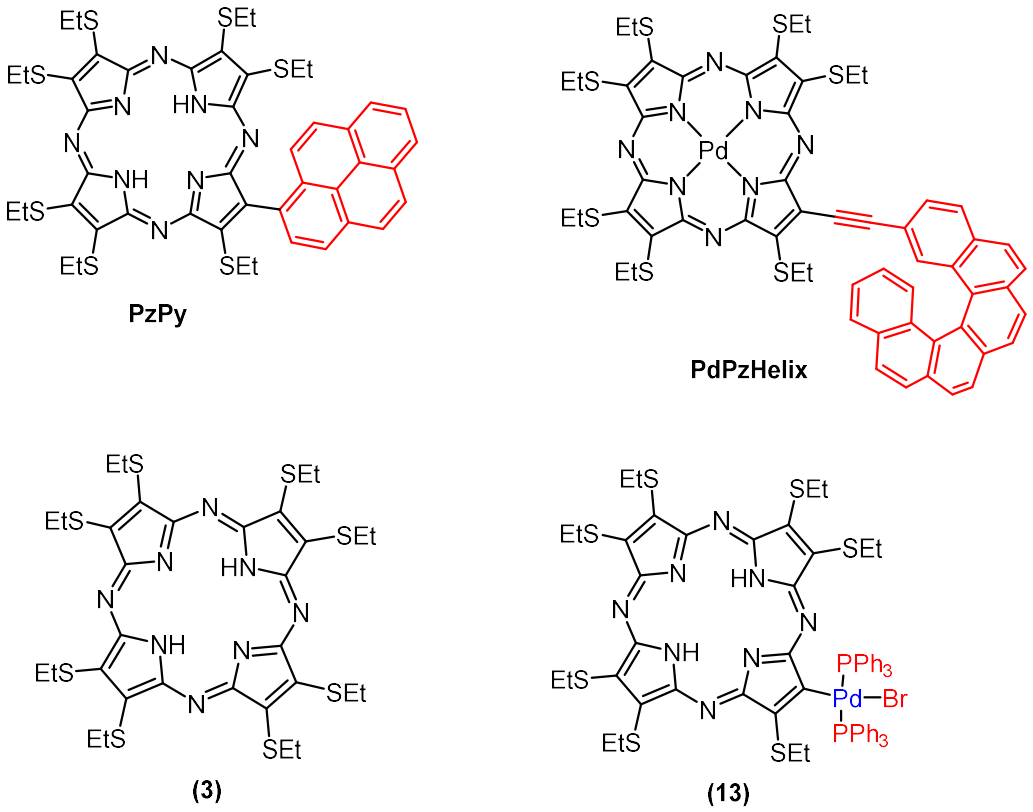

Figure 4 *Thioethyl porphyrazine employed as donor in BHJ solar cells.*

Table 4 *Experimental data for the thioalkyl porphyrazines studied during this Ph.D. thesis work*

Compound	PCE (%) vs $PC_{60}BM$	FF (%)	J_{sc} (mA/cm^2)	V_{oc} (V)	HOMO (eV)	LUMO (eV)	UV-Vis (λ_{max}/nm) in CH_2Cl_2
3	0.10	42.0	-0.77	0.310	/	-3.9 (CH_2Cl_2)	359 (Soret); 500 (extra band); 637 and 710 (Q bands)
PdPzHelix	0.09	42.8	-0.52	0.398	/	-3.8 (CH_2Cl_2)	265; 274; 334 (Soret); 514 (extra band); 663 (Q band)
PzPy	0.06	36.2	-0.71	0.242	-5.5 (CH_2Cl_2) -5.5 (DMF)	-3.9 (CH_2Cl_2) -4.0 (DMF)	277; 350 (Soret); 513 (extra band); 640 and 709 (Q bands)
13	0.04	35.7	-0.72	0.172	/ -5.5 (DMF)	-3.7(CH_2Cl_2) -3.9 (DMF)	307; 363 (Soret); 515 (extra band); 650 and 693 (Q bands)

Morphological and spectroscopic analyses suggest that substantial improvements can be achieved through optimization of key parameters. In particular, the donor-to-acceptor ratio plays a crucial role in determining the morphology of the active layer and, consequently, exciton dissociation and charge transport. The choice of acceptor material is another key factor, as it can significantly influence electron mobility, energy-level alignment, and device stability. Additionally, film formation parameters should be carefully controlled. In particular, factors such as the speed used for the spin coating process, the solvent choice, and the post-deposition thermal annealing temperature, can strongly affect the nanoscale morphology and uniformity of the active layer. Attention should also be paid to the electron transport layer and the hole transport layer. Optimising these layers can result in more efficient charge transport and collection, further boosting the performance of the solar cells.

Overall, this work provides new synthetic methodologies, structural insights, and functional understanding of porphyrazine-based systems, contributing to the advancement of tetrapyrrolic materials for organic photovoltaics and paving the way for future developments aimed at enhancing device performance. Improvement in device performance would also pave the way for the next stage of investigation of these molecular systems. Scaling up both material production and device area could become feasible, supported by the relatively straightforward synthetic access to thioalkyl-porphyrazines. Compared with the state-of-the-art polymers and small molecules currently employed

as electron donors in organic photovoltaic devices, these compounds can be obtained through a reduced number of synthetic steps, potentially offering significant advantages in terms of cost-effectiveness, scalability, and industrial implementation.

List of publication

1. **Conference Poster presentation:** G. Larotonda,* A. Buono, E. Mecca, S. Belviso
   "Novel thienyl-substituted porphyrazine complexes for photovoltaic applications"
   XLIX Italian Conference of Inorganic Chemistry – INORG2023 - Perugia, 12th-15th September 2023
   Book of Abstract, P46

2. **Conference Poster presentation:** S. Belviso, G. Larotonda,* A. Tuzi
   "Synthesis and catalytic activity of a β-η^{1}-Pd(II)-thioethyl porphyrazine complex"
   XXVIII Congresso Nazionale della Società Chimica Italiana - Milano, 26-30 Agosto 2024
   Atti del Convegno, INO-PO-037
   Link:***https://www.assotic.it/wp-content/uploads/2024/09/XXVIII-Congresso-Nazionale-SCI2024-Book-of-Abstract-volume-1.pdf***

3. **Conference Oral presentation:** G. Larotonda*, S. Bellani, F. Bonaccorso, A. Tuzi, S. Belviso
   "Synthesis and characterization of noncovalent nanohybrids of a β-η^{1}-Pd(II)-thioethyl porphyrazine complex and graphene nanoflakes"
   II Virtual Symposium on Pericyclic Reactions and Synthesis of Carbon- and Heterocyclic Systems (CIRP) – 28th-29th November 2024
   Book of Abstract, OC p.36

4. **Peer-Reviewed Journal:** S. Belviso, G. Larotonda, E. Santoro, A. Santarsiere, A. Tuzi,
   Dalton Transactions, 2025 (selected as HOT PAPER by the Editor)
   "Synthesis, electronic properties, structural studies, and catalytic activity of peripherally metalated β-η^{1}-Pd(II)-thioalkyl porphyrazine"
   DOI: ***10.1039/D5DT01394A***
   Link: ***https://pubs.rsc.org/en/content/articlelanding/2025/dt/d5dt01394a***

Acknowledgments

Financial support from the European Union NextGenerationEU and the Italian Ministry of University (MUR) National Recovery and Resilience Plan (NRRP) Program "Strengthening of research structures and creation of R&D innovation ecosystems" (Tech4You –Technologies for climate change adaptation and quality of life improvement Project grant n. ECS_0000009) is gratefully acknowledge.

The preparation of the complex **13** nanohybrids with graphene nanoflakes, along with microscopy analyses, emission and Raman spectroscopy, and photocurrent measurements, was carried out during the industrial stage at BeDimensional (Genova) under the supervision of Dr. Francesco Bonaccorso and Dr. Sebastiano Bellani, whom we gratefully acknowledge.

Dr. Ernesto Santoro (University of Basilicata) is acknowledged for the computational studies performed on complex **13**, and Dr. Fausto Langerame (University of Basilicata) for the X-ray Photoelectron Spectroscopy (XPS) analysis of the active layers.

Prof. Angela Tuzi (University of Naples - Federico II) is gratefully acknowledged for her crystallographic studies on complex **13**.

Prof. Emmanuel Kymakis is acknowledged for his hospitality during the Ph.D. research period abroad at the Hellenic Mediterranean University (HMU), within the Nanomaterials for Emerging Devices research group. Dr. Eirini Koutsouroubi and Dr. Nikos Tzoganakis are acknowledged for their laboratory support in the fabrication and characterization of BHJ cells.